THE UNIVERSITY OF QUEENSLAND

AUSTRALIA

# Improving the Image Quality in Compressed Sensing MRI by the Exploitation of Data Properties

Yang Yang

Bachelor of Engineering – Communication

Master of Engineering – Embedded System

*A thesis submitted for the degree of Doctor of Philosophy at*
*The University of Queensland in* 2016

School of Information Technology and Electrical Engineering

# Abstract

Minimizing scan time without compromising image quality has been the main thrust of magnetic resonance imaging (MRI) since the establishment of the field. Tremendous effort has been put into MRI systems in pursuit of faster MR imaging techniques, which can substantially facilitate clinical diagnoses and improve the patient experience. Traditional MRI accelerated approaches mainly focused on hardware improvements to improve the speed of scanning. These methods are still governed by Nyquist-Shannon sampling rate. Hence, when the acceleration rate is pushed beyond the theoretical limit, aliasing artefacts are introduced which degrade the reconstructed image quality and are difficult to eliminate via current methods. Recently, it has been found that a newly developed signal processing theory, compressed sensing (CS), can be used to create high-resolution signal data sets from sparse samples, despite violating the classical Nyquist-Shannon sampling criteria. The application of CS to MRI opens up an appealing avenue to offer potentially significant scan time reductions. CS reconstructs MR images from incomplete k-space measurements. Taking advantage of the fact that MR images have sparse representations under certain mathematical transformations, CS overcomes the distortions resulting from the under-sampled k-space data. Significant progress has been made in the development of CS MRI. However, there are two major remaining challenges to its full adoption in clinical applications: (1) the small amount of under-sampled data (for example, less than 1/8 of the whole k-space data) will inherently introduce artefacts in the reconstructed image and compromise diagnosis accuracy for the reconstructed images; (2) owing to hardware limits, it is difficult to realise two-dimension random under-sampling, which is favoured by CS operation. Practically, the random phase-encode under-sampling pattern has been widely implemented. However, it introduces coherent aliasing artefacts that are hard to eliminate using the CS theory.

In this thesis, several techniques are proposed that can improve the quality of images reconstructed by CS MRI. These techniques have the potential to facilitate faithful reconstruction of CS MRI in clinical applications. A novel two-stage reconstruction scheme is introduced in Chapter 3. In this method, the under-sampled *k*-space data is segmented into low-frequency and high-frequency parts. Then, in stage one, using dense measurements, the low-frequency region of k-space data is faithfully reconstructed. The fully reconstituted low-frequency *k*-space data from the first stage is then combined with the under-sampled high-frequency *k*-space data to complete the second stage reconstruction of the whole image. With this two-stage approach, each reconstruction inherently incorporates a lower data under-sampling rate than conventional approaches. Because the restricted isometric property is easier to satisfy than conventional CS method, the reconstruction consequently produces lower residual errors in each step. Results from different MR test cases demonstrate the remarkable improvement in the quality of reconstruction using the proposed approach.

Chapter 4 then introduces a novel approach to reduce the aliasing artefacts induced by random phase-encode under-sampling. The proposed reconstruction process is separated into two steps in our new algorithm. In step one, we transfer the original two-dimensional (2D) image reconstruction into a parallel one-dimensional (1D) signal reconstruction procedure, which takes advantage of the superior incoherence property in the phase direction. In step two, using the new k-space data obtained from the 1D reconstructions, we then implement a follow-up 2D CS reconstruction to produce a better solution, which exploits the inherent correlations between the adjacent lines of 1D reconstructed signals. Validated by experiments, the proposed method achieves more accurate reconstruction results and effectively suppresses the coherent artefacts introduced by random phase-encode under-sampling.

Chapter 5 introduces a novel non-Cartesian trajectory, a pseudo-polar (PP) trajectory, instead of random phase-encode under-sampling pattern in a Cartesian grid. As a compromise with the hardware limitations, a Cartesian trajectory is widely used in current CS MRI, even though it introduces coherent aliasing artefacts in the corresponding random phase-encode under-sampling pattern. Compared with the conventional Cartesian trajectory, the PP trajectory collects more data from the central k-space region and the radially sampled data are more incoherent. These properties are very suitable for CS based fast imaging. When reconstructing under-sampled PP data with CS, PP Fast Fourier Transform (FFT) is implemented to realize the fast and accurate transform between k-space and image domain. Based on the standard 1D FFT and the Fractional Fourier Transform (FRFT), PPFFT avoids the time-consuming interpolation process in the transform of other non-Cartesian trajectories. Investigated by simulations and in vivo experiments, the proposed scheme provides a practical and accurate CS-based rapid MR imaging method for clinical applications.

This thesis presents a series of original research contributions as described above. The key novelty of these CS MRI methods relies upon the exploitation of the features of the MRI data. These methods have been tested with typical MR datasets, and the experimental results suggest that, these innovative methods are capable of producing high quality MRI images with reduced scan time (usually 4-8 times faster). These new CS MRI methods have the potential for both clinical and preclinical applications.

## Declaration by author

This thesis is composed of my original work, and contains no material previously published or written by another person except where due reference has been made in the text. I have clearly stated the contribution by others to jointly-authored works that I have included in my thesis.

I have clearly stated the contribution of others to my thesis as a whole, including statistical assistance, survey design, data analysis, significant technical procedures, professional editorial advice, and any other original research work used or reported in my thesis. The content of my thesis is the result of work I have carried out since the commencement of my research higher degree candidature and does not include a substantial part of work that has been submitted to qualify for the award of any other degree or diploma in any university or other tertiary institution. I have clearly stated which parts of my thesis, if any, have been submitted to qualify for another award.

I acknowledge that an electronic copy of my thesis must be lodged with the University Library and, subject to the policy and procedures of The University of Queensland, the thesis be made available for research and study in accordance with the Copyright Act 1968 unless a period of embargo has been approved by the Dean of the Graduate School.

I acknowledge that copyright of all material contained in my thesis resides with the copyright holder(s) of that material. Where appropriate I have obtained copyright permission from the copyright holder to reproduce material in this thesis.

## Publications during candidature

### *Peer-reviewed journal papers*

**Yang Yang**, Feng Liu, Wenlong Xu and Stuart Crozier, Compressed Sensing MRI via Two-stage Reconstruction, *IEEE Transactions on Biomedical Engineering*, vol.62, pp.110-118, 2015.

**Yang Yang**, Feng Liu, Zhaoyang Jin and Stuart Crozier, Aliasing Artefact Suppression in Compressed Sensing MRI for Random Phase-encode Undersampling, *IEEE Transactions on Biomedical Engineering*, vol.62, pp.2215-2223, 2015.

**Yang Yang**, Feng Liu, Mingyan Li, Jin Jin, Ewald Weber, Qinghuo Liu and Stuart Crozier, Pseudo-Polar Fourier Transform based Compressed Sensing MRI, *IEEE Transactions on Biomedical Engineering*, (accepted).

### *Peer-reviewed conference papers*

**Yang Yang**, Mingyan Li, Ewald Weber, Jin Jin, Feng Liu, Sven Junge and Stuart Crozier, Rapid Radial MRI using Compressed Sensing and a Rotating RF Coil at 9.4T, *38th Annual International Conference of the IEEE Engineering in Medicine and Biology Society (EMBC'16)*, Orlando, USA, 2016.

Zhen Feng, He Guo, Yinxin Wang, Yeyang Yu, **Yang Yang**, Feng Liu and Stuart Crozier, GPU accelerated high-dimensional compressed sensing MRI, *13th International Conference on Control Automation Robotics & Vision*, Singapore, 2014.

## Publications included in this thesis

Chapter 3: **Y. Yang**, F. Liu, W. Xu and S. Crozier, Compressed Sensing MRI via Two-stage Reconstruction, *Biomedical Engineering*, *IEEE Transactions on*, vol. 62, pp. 110-118, 2015.

**Author contributions**

| | |
|---|---|
| Yang Yang | Methodology development (90%), code implementation (100%), analysis and interpretation (60%), manuscript preparation (100%) |
| Feng Liu | Methodology development (10%), analysis and interpretation (20%), manuscript review (70%) |
| Wenlong Xu | Analysis and interpretation (10%), manuscript reviews (10%) |
| Stuart Crozier | Analysis and interpretation (10%), manuscript reviews (20%) |

Chapter 4: **Y. Yang**, F. Liu, Z. Jin and S. Crozier, Aliasing Artefact Suppression in Compressed Sensing MRI for Random Phase-encode Undersampling, *Biomedical Engineering*, *IEEE Transactions on*, vol. 62, pp. 2215-2223, 2015.

**Author contributions**

| | |
|---|---|
| Yang Yang | Methodology development (90%), code implementation (100%), analysis and interpretation (60%), manuscript preparation (100%) |
| Feng Liu | Methodology development (10%), analysis and interpretation (20%), manuscript review (70%) |
| Zhaoyang Jin | Analysis and interpretation (10%), manuscript reviews (10%) |
| Stuart Crozier | Analysis and interpretation (10%), manuscript reviews (20%) |

Chapter 5: **Y. Yang**, F. Liu, M. Li, J. Jin, E. Weber, Q. Liu and S. Crozier, Pseudo-Polar Fourier Transform based Compressed Sensing MRI, *Biomedical Engineering*, *IEEE Transactions on*, 2016, accepted.

**Author contributions**

| | |
|---|---|
| Yang Yang | Methodology development (90%), code implementation (100%), experimental design (50%), execution of experiments (30%), analysis and interpretation (40%), manuscript preparation (100%) |
| Feng Liu | Methodology development (10%), analysis and interpretation (10%), manuscript review (10%) |
| Mingyan Li | Experimental design (25%), execution of experiments (35%), analysis and interpretation (10%), manuscript review (30%) |
| Jin Jin | Experimental design (25%), execution of experiments (35%), analysis and interpretation (10%), manuscript review (30%) |
| Ewald Weber | Analysis and interpretation (10%), manuscript reviews (10%) |
| Qinghuo Liu | Analysis and interpretation (10%), manuscript reviews (10%) |
| Stuart Crozier | Analysis and interpretation (10%), manuscript reviews (10%) |

## Contributions by others to the thesis

Professor Feng Liu (primary supervisor), Professor Stuart Crozier (associate supervisor), Dr Jin Jin (colleague) and Dr Mingyan Li (colleague) have all made contributions in discussions about research ideas, experimental designs, data collection and the interpretation of the experimental results. Their individual contributions are detailed in the previous section and are listed at the beginning of Chapters 3–5. Prior to submission, the thesis was reviewed by all PhD supervisors with corrections being inserted by the author. This thesis has been edited by Wendy Smith (Chapter 1, 2 and 6).

## Statement of parts of the thesis submitted to qualify for the award of another degree

None

## Acknowledgements

Over the past four years, I have received support and encouragement from a great number of individuals. I would like to take this opportunity to express my sincere gratitude to everyone who has helped me during my PhD study.

First and most, I would like to express my deepest appreciation to my PhD supervisors Prof. Feng Liu and Prof. Stuart Crozier. I am extremely grateful to them for providing me with the opportunity to work in a wonderful research environment. Thanks to Feng Liu for always finding the time to understand my preliminary ideas and being enthusiastic for the whiteboard discussions that sometimes last for hours. Thanks for thousands of emails, many of which were exchanged over the nights and weekends. Thanks to Stuart Crozier for organising regular meetings to have insightful discussions and point out the right research direction. The discussions with both supervisors have generated many ideas and identified many flaws in my thinking. Without their excellent guidance and persistent support, I would never have been able to finish this dissertation.

My thanks go to Dr Jin Jin and Dr Mingyan Li for their tuition on understanding various aspects of MRI hardware system and for many discussions on MRI signals. Thanks also go to Kimberley Nunes for her patient and careful tutoring in academic writing.

The research in this thesis was funded by CSC-UQ PhD Scholarship and Top Up Assistance Program. I am also appreciative of the financial support in the form of travel grants from the University of Queensland.

Finally, I would like to say thanks to my parents, my parents-in-law and my grandparents, who have been supportive throughout my life in every way possible. Most of all I am deeply grateful to my loving and supportive wife Nan Wang for her trust and understanding through good and bad times. You are the joy of my life.

## Keywords

compressed sensing, mri, *k*-space segmentation, two-stage reconstruction, random phase-encode under-sampling, aliasing artefact suppression, non-Cartesian trajectory, pseudo-polar grid, rapid imaging.

## Australian and New Zealand Standard Research Classifications (ANZSRC)

| | |
|---|---|
| ANZSRC code: 090304, Medical Devices | 30% |
| ANZSRC code: 090399, Biomedical Engineering not elsewhere classified | 70% |

## Fields of Research (FoR) Classification

| | |
|---|---|
| FoR code: 0903, Biomedical Engineering | 100% |

# Table of Contents

# List of Figures

# List of Tables

# List of Abbreviations

| | |
|---|---|
| MRI | Magnetic Resonance Imaging |
| CS | Compressed Sensing |
| RF | Radio Frequency |
| PI | Parallel Imaging |
| SENSE | Sensitivity Encoding |
| GRAPPA | Generalised Autocalibrating Partial Parallel Acquisition |
| 1D | one-dimensional |
| 2D | two-dimensional |
| FFT | Fast Fourier Transform |
| DFT | Discrete Fourier transform |
| IDFT | Inverse Discrete Fourier transform |
| FOV | Field of View |
| FSE | Fast Spin-Echo |
| EPI | Echo-Planar Imaging |
| TSE | Turbo Spin-Echo |
| RARE | Rapid Acquisition with Refocused Echoes |
| CSE | Conventional Spin-Echo |
| TR | Repetition Time |
| ETL | Echo Train Length |
| SNR | Signal-to-Noise Ratio |

| | |
|---|---|
| RIP | Restricted Isometry Property |
| PSNR | Peak Signal-to-Noise Ratio |
| SSIM | Structural Similarity |
| RMSE | Root Mean Square Error |
| PSF | Point Spread Function |
| CS MRI | Compressed Sensing in MRI |
| TV | Total Variation |
| DCT | Discrete Cosine Transforms |
| SVD | Singular value decomposition |
| HOSVD | Higher-order Singular Value Decomposition |
| BP | Basis Pursuit |
| BPIC | Basis Pursuit with Inequality Constraints |
| BPDN | Basis Pursuit De-Noising |
| FCSA | Fast Composite Splitting Algorithm |
| NCG | Nonlinear Conjugate Gradient |
| PP | Pseudo-Polar |
| PPFFT | Pseudo-Polar Fast Fourier Transform |
| LS | Least Squares |
| fMRI | Functional MRI |
| SAR | Specific Absorption Rate |

# 1. Introduction

## 1.1 Motivation

As arguably the most important diagnostic imaging method ever developed, magnetic resonance imaging (MRI) offers unprecedentedly detailed anatomic and functional information of the human body. As such, MRI is now the method of choice in the diagnosis of the entire spectrum of human diseases, some of which are not easily diagnosed by any other imaging modalities. In the MRI scanning process, the patient is placed in a strong static magnetic field, in which the water protons within the body resonate at a radio frequency that is proportional to the static field strength. A number of detectors operating at the same radio frequency (usually called RF coils) are placed around the patient to excite and receive the MR signals. These signals are spatially encoded by gradient coils and digitally recorded in a computer system. The raw image data is acquired in the frequency domain (usually called the *k*-space), which is used to reconstruct diagnostic images using a Fourier Transform technique. Limited by physical and physiological constraints, the chronological acquisition of the full *k*-space is intrinsically slow. The lengthy scan process in MRI examinations introduces physiological motion artefacts, causes additional discomfort to the patient and reduces the temporal resolution critical for depicting specific details like cardiac dynamics. Thus, existing MR technology can fall short in some circumstances in its capacity to provide high quality diagnostic images. Also, the imaging speed limits further applications of MRI which require real-time output for dynamic imaging.

Minimising scan time without compromising image quality has been one of the main thrusts of MRI research. In traditional rapid MRI techniques, two main streams have been developed for imaging acceleration. The first one is based on full *k*-space scanning which uses a combination of fast gradients and RF coil pulse sequence [1-3]. While these methods have some drawbacks, such as (1) technological challenges associated with fast gradient coils and intensive sequences in hardware; (2) degraded image quality caused by eddy current distortions and nonlinear gradient magnetic fields; and (3) stimulation of the peripheral nerve and the potential to interfere with heart-muscle activity caused by the fast switched gradient [4]. The second approach is parallel imaging (PI), which is based on partial *k*-space sampling. PI uses multiple receive RF coils to implement simultaneous *k*-space under-sampling and reconstruct the whole image with prior information from the RF coils' distinctive sensitivity profiles. Many different PI algorithms have been developed to reconstruct the image, for example, Sensitivity Encoding (SENSE) [4, 5] and Generalised Autocalibrating Partial Parallel

Acquisition (GRAPPA) [6]. However, these PI methods force a trade-off between image quality and temporal resolution owing to: (1) the coil sensitivity maps being difficult to accurately obtain; (2) the noise of the PI not being distrustful or constant across the images but instead depending on the geometric factor, which is a spatially dependent parameter; (3) the moderate acceleration rates (usually less than four-fold) in clinical routine.

A recently developed technique, compressed sensing (CS) [7], a novel fast imaging technique that uses partial *k*-space sampling to reconstruct the image, is making a major impact on accelerating MRI speed [8-10]. CS is a relatively new signal processing theory; it combines the sampling and compression into one step by measuring fewer samples that contain more information about the signals [7, 11]. Utilizing a "getting more from less" strategy, CS eliminates the need to acquire large numbers of samples and aims to reconstruct signals from significantly fewer measurements than previously thought necessary using the traditional Nyquist criterion. In theory, CS can faithfully reconstruct MR images from highly incomplete *k*-space measurements and significantly reduce the scan time.

According to these mathematical properties, there are three key elements that must be acquired for a successfully application of CS in MRI [9]:

- Transform sparsity: The MR images should be represented in a known transform domain with a very small number of pixels with large values and the rest with zero or infinitesimal values.
- Incoherence of under-sampling artefacts: The artefacts introduced by the partial *k*-space sampling should be noise-like (incoherent) in the sparsifying transform domain.
- Nonlinear reconstruction: Through a nonlinear reconstruction algorithm, an artefact-free image can be recovered by enforcing both the sparsity of the signals representation and consistency of the reconstruction with the acquired samples.

Theoretically, the three conditions can be clearly met. However, the conventional CS methods suffer from at least two limitations in the real application of MRI. First, when CS is applied to some specific cases in dynamic MR imaging, the real-time imaging requirement pushes for a higher acceleration rate to shorten the scan time. With the same sparse transform, the less sampled data cannot cover enough important coefficients to compress the image without losses. The lossy information leads to residual incoherent artefacts in the reconstruction that CS fails to recover and, thus, degrades the quality of the reconstructed images. Second, the ideal two-dimensional (2D) random *k*-space under-sampling with great incoherence is impractical due to hardware and physiological constraints. Instead, a one-dimensional (1D) random under-sampling scheme can be easily realized by adapting the Cartesian trajectory widely used in MRI. Meanwhile, it has a weak performance in incoherence and introduces coherent aliasing artefacts which are hard to handle using CS. The alternative non-Cartesian under-sampling schemes have the required incoherence. However, the reconstruction of images from the *k*-space data sets acquired by non-Cartesian trajectories requires more computation time and achieves less accurate in results than using sampling based on a Cartesian trajectory. These constraints limit the further application of non-Cartesian trajectories in rapid imaging with CS, leading to inaccurate image reconstruction for diagnosis purposes.

To resolve the issues of conventional CS applications in MRI, this thesis will develop three novel reconstruction strategies by exploiting the data properties to improve the image quality reconstructed by CS for rapid MRI. The first one takes advantage of the distribution of *k*-space data and an iterative strategy is proposed to overcome the first limitation. The other two were contributed to break through the second limitation from different angles. The second method applies the *k*-space Fourier transform by parts to suppress the aliasing interference introduced by the weak incoherence of one-dimensional under-sampling. The third method brings in a novel non-Cartesian trajectory, which keeps the property of incoherence for CS and realize the fast and accurate transform between *k*-space and image domain.

## 1.2 Thesis outline

The remainder of this thesis is organized as follows.

Chapter 2 starts with a brief introduction of MRI, which specifically provides the current acceleration techniques in MRI and the motivation of applying CS to speed up MRI scanning. Then, a description of CS is given which covers its theoretical validation. And finally, a detailed introduction of CS being applied in MRI is provided and related typical applications are reviewed.

In Chapter 3, a novel two-stage CS reconstruction technique is proposed that uses a *k*-space segmentation scheme to address the challenge of high reduction factors in CS MRI. Considering the inhomogeneous power distribution of the *k*-space data, a *k*-space segmentation scheme is applied to separate the *k*-space data into a central region and peripheral regions. Utilizing the segmentation scheme, an image outline can first be reconstructed based on the densely sampled *k*-space centre. Combining the peripheral *k*-space data, a full image is then accurately recaptured by using the recovered low frequency *k*-space region. With this two-stage approach, each reconstruction inherently incorporates a lower data under-sampling rate than the conventional non-staged approach. Consequently, fewer residual reconstruction errors are introduced, which improves the quality of reconstructed images especially at high reduction factors.

Chapter 4 focuses on the incoherence issue to reduce the large coherent aliasing artefacts introduced by the random phase-encode under-sampling of Cartesian *k*-space trajectory. We take advantage of *k*-space features to separate the 2D image reconstruction into a series of parallel 1D signal reconstructions. With the excellent 1D incoherence property in the phase-encoding direction of the under-sampling pattern, the 1D CS algorithm is implemented to recover the series of parallel 1D signals. Using the *k*-space data obtained from the parallel 1D signal reconstructions, we then implement a second 2D CS reconstruction to recover the whole image. The aliasing artefact suppression in the serial 1D signal reconstructions and the junction enhancement of 1D signals in the following 2D reconstruction effectively improve the reconstructed image quality.

In Chapter 5, a novel CS-based imaging scheme is proposed to incorporate a pseudo-polar trajectory for MR data sampling. As a non-Cartesian *k*-space sampling scheme, a pseudo-polar trajectory has a superior performance in incoherence, which can eliminate the coherent aliasing artefacts in conventional CS MRI based on a Cartesian trajectory. Compared with a radial trajectory, a representation of a non-Cartesian trajectory, a pseudo-polar trajectory uses the concentric squares distribution and equal-slope spokes to replace the concentric circles distribution and equal-angle spokes in a radial trajectory. The similarity demonstrates pseudo-polar trajectory inherits the low motion sensitivity of radial trajectory. The concentric squares distribution ensures that the pseudo-polar trajectory can cover the corners of the square *k*-space, which missed by the circular sampling region of a radial trajectory. The high-frequency information in the corners can preserve the image details/edges. Moreover, using the corresponding pseudo-polar Fourier transform, it is straight forward process to reconstruct the image from the raw *k*-space data, which is an obstacle to other non-Cartesian trajectories. The promising results based on simulation and experimental data demonstrate the performance and feasibility of the proposed method.

Finally, in Chapter 6, this thesis will conclude with a summary of the contributions of my research, in terms of improving the reconstruction quality of CS MRI. In addition, some insights into possible future applications will be discussed.

# 2. Compressed Sensing MRI

The purpose of Chapter 2 is to illustrate the framework of Compressed Sensing MRI. In Section 2.1, the MR image formation is briefly introduced and the reasons for introducing compressed sensing to MRI are explained. Then in Section 2.1.1, the theoretical basis of compressed sensing is reviewed. The requirements for applying CS to MRI and some applications of CS in MRI are presented in Section 2.3.

## 2.1 MRI image formation and acceleration techniques

MRI is a powerful noninvasive medical imaging technique; it provides anatomical images based upon a phenomenon called nuclear magnetic resonance (NMR) discovered in 1946 by Bloch and Purcell [12]. The MR technique was first used as a research tool for determining the structures of molecules. Later, Lauterbur ([13], 1973) and Mansfield ([14, 15], 1977), who were joint Nobel Prize winners in 2003, developed the technology for medical imaging purposes and made pioneering contributions leading to the development of the modern MRI empire, which represented a significant breakthrough in the medical field. As arguably the most important diagnostic imaging method ever developed, MRI offers unprecedented detailed anatomic and functional information on the human body, and as such, MRI is now the method of choice for the diagnosis of the entire spectrum of human diseases. Over 25,000 MRI scanners have been installed into the various services of clinical diagnosis and research around world [16].

As a tomographic imaging technique, MRI provides visualization of internal tissue structures and functions of an object from externally measured NMR signals. NMR is the resonance phenomenon arising from the interactions of the nuclei of the imaged object and the homogenous static magnetic fields generated by the main magnet. Then, the resonance signals are localized by the low-frequency linear gradient fields through three orthogonal gradient coils. Finally, the radio-frequency (RF) system uses a transmitter coil to generate an RF magnetic field to excite the tissue and a receiver coil is used to convert the processing NMR signals into a recordable electrical signal. So the main magnet, a set of gradient coils and one or more RF coils combine to form the basic components of an MRI system [17]. All of these operations are in the RF range, thus avoiding the use of ionizing radiation and its associated potential harmful effects. In contrast to other tomographic imaging devices, MRI can generate 2D sectional images at any orientation, 3D volumetric images, or even 4D images representing spatial-spectral distributions without any additional mechanical adjustments [17].

MR images are not directly acquired in image domain during the data collection. Rather, the readout MR signals are stored in a *k*-space which is equivalent to a Fourier plane. A *k*-space is a deconstructed representation of spatial frequencies inherent in the original object. Although the *k*-space and the MR image appear quite different, they contain identical information about the scanned object. Figure 2-1 illustrates the relationship between the *k*-space domain and the image domain. Each point in a *k*-space domain holds specific spatial frequency and phase information about each pixel in the entire image, and vice-versa. These two representations can be interconverted using the Fourier Transform.

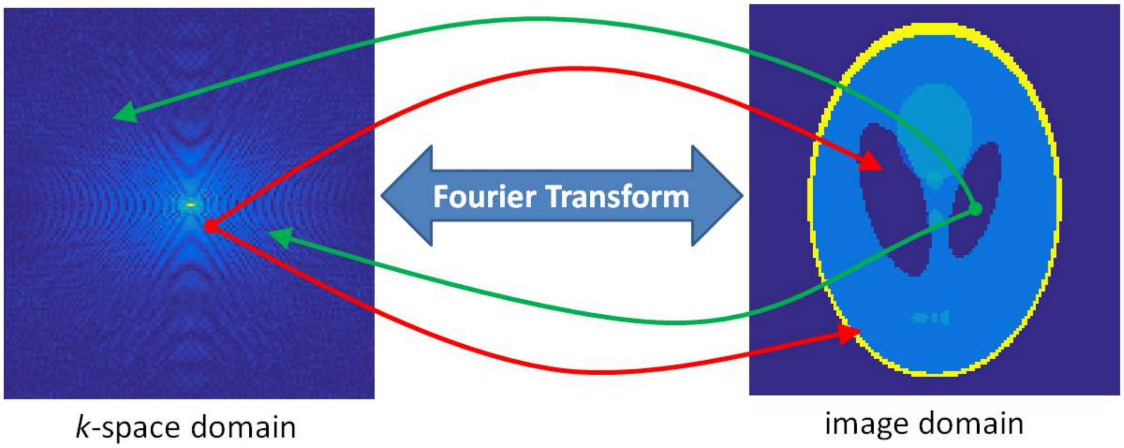

**Figure 2-1. The relationship between *k*-space and the corresponding image.**

As we know, it is practically impossible to sample the MR signals with infinite frequency information. In order to represent the object faithfully in the prescribed resolution and field-of-view (FOV), the data to fill the *k*-space are sampled discretely from the MR signal and satisfy the conventional standard, the Nyquist-Shannon sampling theorem. As long as the theorem is followed, the data can be acquired in any order/trajectory. Although the non-Cartesian trajectories such as spiral and radial (refer to Figure 2-2a and Figure 2-2b) are becoming popular in MRI these days, the line-by-line Cartesian trajectory (seeing Figure 2-2c) is widely used in current MRI systems and has been used nearly exclusively in MRI systems over the last 30 years.

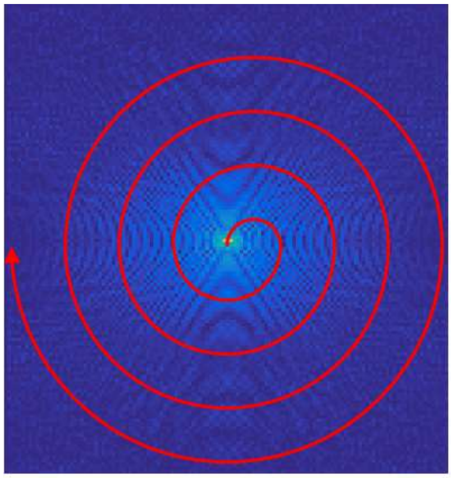

(a) Spiral Trajectory

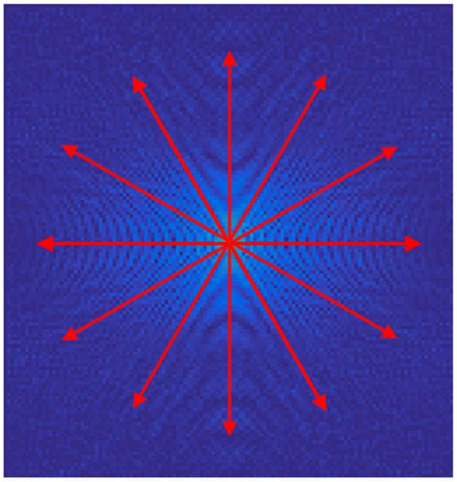

(b) Radial Trajectory

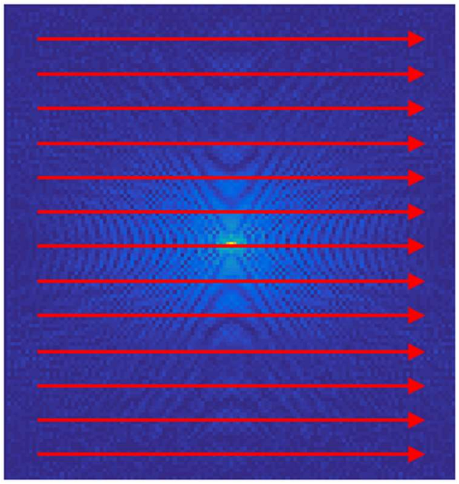

(c) Cartesian Trajectory

**Figure 2-2. Typical *k*-space sampling trajectories.**

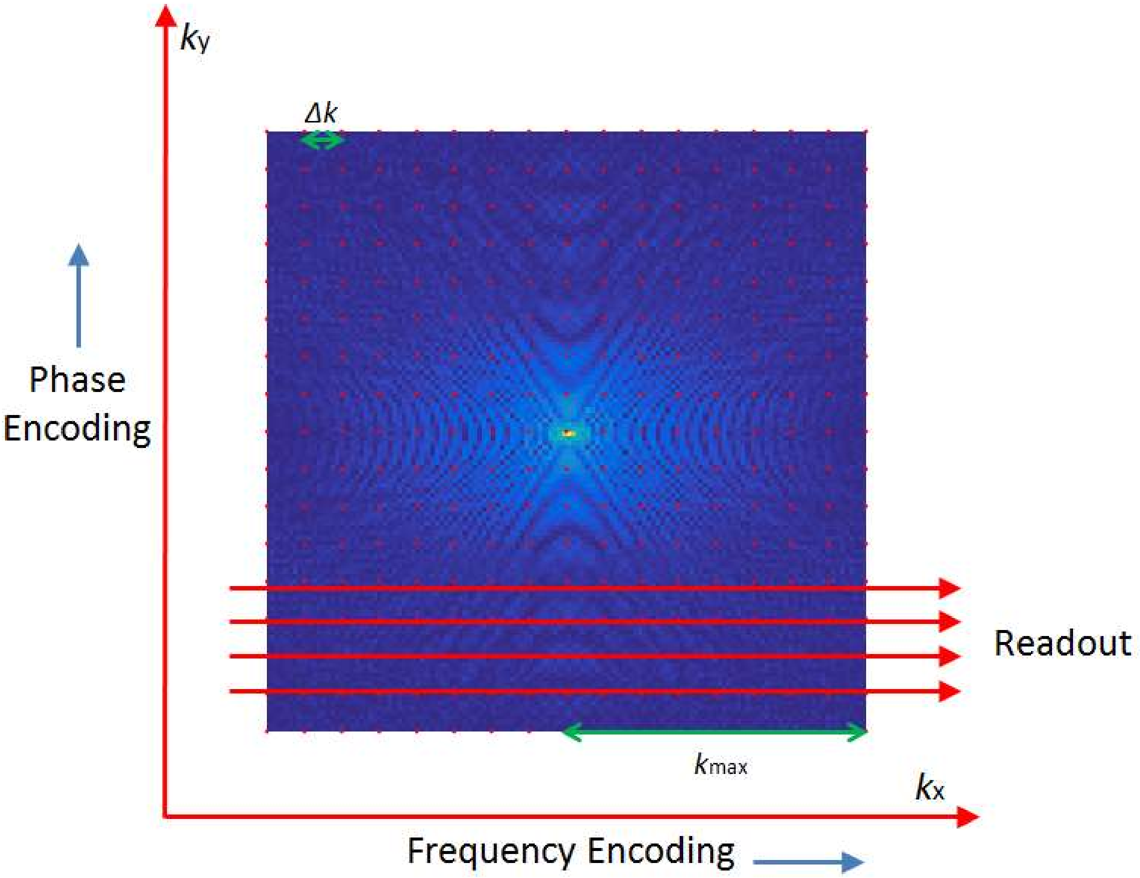

**Figure 2-3. The *k*-space data acquistion by traditional line-by-line Cartesian MRI.**

An example of a conventional 2D line-by-line Cartesian trajectory is illustrated in Figure 2-3. The full *k*-space data are positioned by frequency encoding and phase encoding with magnetic gradient fields. During the frequency encoding, the gradient amplitude is constant and all the points on one row along the $k_x$ direction can be obtained rapidly within one repetition time (TR) using either a spin or gradient echo [17]. As the echo signal is recorded in quadrature, each point in the *k*-space contains real and imaginary components. In phase encoding, the gradient amplitude is normally varied to switch the rows while the gradient duration is kept constant. So each column along the $k_y$ direction represents the line of data points that are obtained for a given amplitude of the phase encoding gradient. The distance between each adjacent row or column is denoted as $\Delta k$, which determines the FOV of the final image. The distance from the centre to the boundary of the *k*-space is denoted as $k_{\max}$, which determines the resolution of the final image.

In the scenarios of high resolution or wide FOV of the images, large amount of *k*-space data is required to meet the Nyquist–Shannon criterion, which can only be acquired by scanning the *k*-space domain along the frequency-encoding direction in a sequential manner. Therefore, the MRI acquisition time can be lengthy. Thus, the loud noise introduced by the high amount of electric current supplied to the system makes patients uncomfortable and leads to some involuntary movement. Additionally, patients are asked to hold their breath in abdominal/thoracic imaging and that is almost infeasible for children and people with respiratory disease or obesity. Consequently, all of these motions during the data acquisition period result in motion artefacts in the final images.

Most physiologic motions such as respiration, cardiac pulsation and gross body movement occur from within a hundred milliseconds to several seconds. Compared with the frequency encoding sampling period, these motions are relatively slow and will only introduce a small number of spatial artefacts along the frequency encoding direction. However, the phase encoding sampling period is generally equal to or longer than the interval of most physiologic motions, therefore, the majority of motion artefacts propagate in the phase encoding direction. There are two types of common artefacts due to motion: blurring and ghost (or misregistration) [17]. The blurring artefact (see Figure 2-4b) is produced by random/nonperiodic movements. The ghost artefact (see Figure 2-4c) is caused by regular/periodic motion like cardiac motion, respiratory motion, vascular pulsation and cerebrospinal fluid pulsation. These motion artefacts significantly affect the quality of MR imaging and sow confusion about a patient's pathology.

In addition to the motion artefacts, the low imaging speed of MRI further limits it application in dynamic or rapid imaging. To overcome the limitations, many innovations in accelerating the scan duration have been tried throughout the history of MRI. In general, these techniques can be separated into accelerated fully-sampled acquisition and acceleration by under-sampled acquisition, which will be reviewed in the following section.

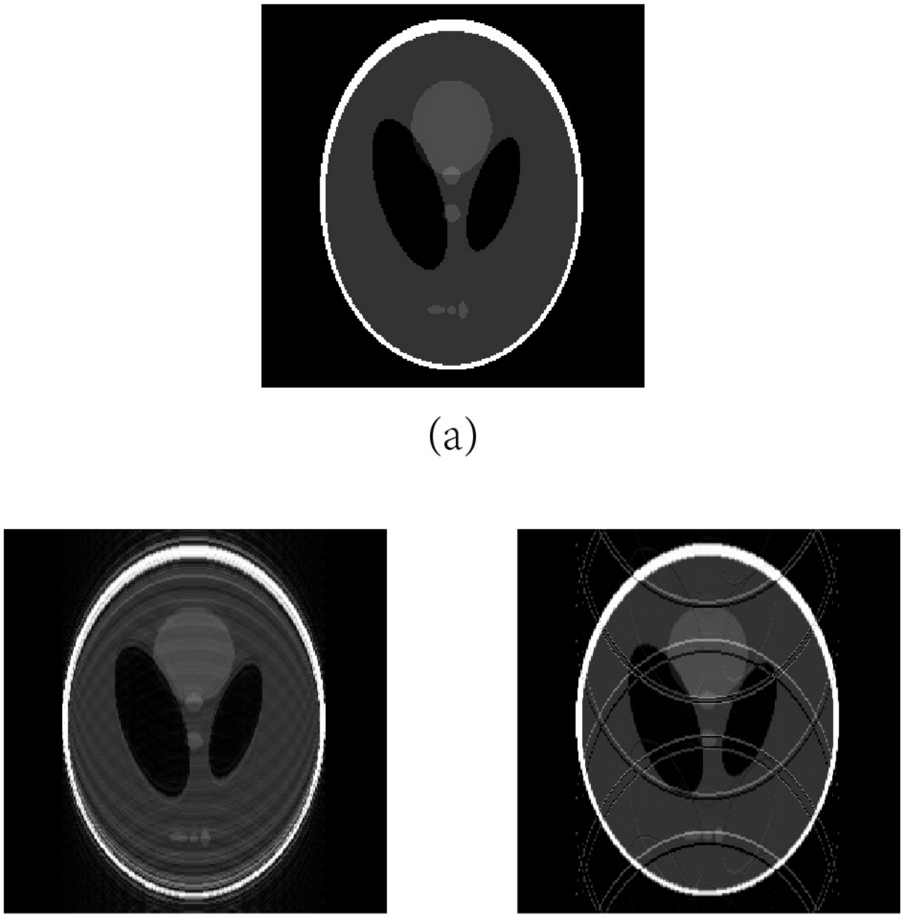
(a)

(b)

(c)

**Figure 2-4. Simulated blurring and ghost artefacts due to motion. (a) Ideal snapshot image. (b) Image with blurring artefacts. (c) Image with ghost artefacts.**

### 2.1.1 Accelerated full *k*-space acquisition

Accelerated full *k*-space acquisition applies the techniques of *k*-space encoding acceleration and still collects the full *k*-space data following the Nyquist–Shannon sampling theorem. Several sequences have been successfully implemented, such as: Fast spin-echo (FSE) imaging and Echo-Planar imaging (EPI).

### *2.1.1.1 Fast Spin-Echo (FSE) imaging*

FSE imaging, also well known as Turbo spin-echo (TSE) imaging, is the clinical practice of Rapid Acquisition with Refocused Echoes (RARE) [18]. The theory was proposed by Hennig et al. in 1986 [18] and conceptually, FSE is an extension of the conventional spin-echo (CSE) [17]. Instead of encoding only one line of the *k*-space per repetition time using CSE, FSE/TSE techniques change the hardware setup so that multiple lines of *k*-space can be encoded per repetition time. The turbo factor, namely the echo train length (ETL), is typically set as 4 to 32 for routine imaging or up to 200 for some specific applications [19].

In addition to the imaging acceleration, the implementation of FSE offers other advantages such as enhanced signal-to-noise ratio (SNR), improved spatial resolution and reduced susceptibility included signal losses. Meanwhile, the FSE has several practical limitations. The first is that FSE may deposit excessive RF power on the object being imaged, due to the fact that a number of pulses are applied in a short time interval in the sequence. This will bring potential hazard to the patients. The second limitation is that FSE may introduce imaging blurring and Gibbs ringing artefacts along the phase-encoding direction, due to the inherent $T_2$ decay during the formation of the echo train [17]. Although $T_2$ decay occurs in both the readout and phase-encoding directions, the imaging blurring is more pronounced in the latter direction. The reason is that the time interval between the first and the last echo is several times longer than a typical readout time interval. In addition, the $T_2$-weighting function along the phase-encoding direction is discontinuous, which will result in the point spread function (PSF) oscillating to introduce the Gibbs ringing artefacts.

### *2.1.1.2 Echo-Planar Imaging (EPI)*

Benefiting from the development of and improvements in MRI hardware, imaging systems with the resultant improved gradient and digital data acquisition technology can acquire each slice within 50-100 ms [17]. EPI is one of these ultra-high-speed imaging techniques. The method was proposed by Mansfield [15] in 1977 and is accomplished by a time-varying gradient. This technique allows the collection of the full *k*-space data for a whole image after a single RF excitation [15]. In this method, a new trajectory, a blipped trajectory (see Figure 2-5), is implemented to traverse the whole *k*-space. EPI can effectively decrease the artefacts due to patient motion and is able to image rapid physiologic processes of the human body. Nevertheless, EPI images suffer from the maximum attainable resolution, which is limited by the $T_2^*$ value. In addition, EPI is sensitive to the inhomogeneity of main magnetic fields. High-performance gradients are also required by EPI to avoid gradient error in imaging. Both of them are caused by hardware limitations. Furthermore, the off-resonance effects and susceptibility effects can affect the performance of EPI by leading to significant artefacts in obtained images [17].

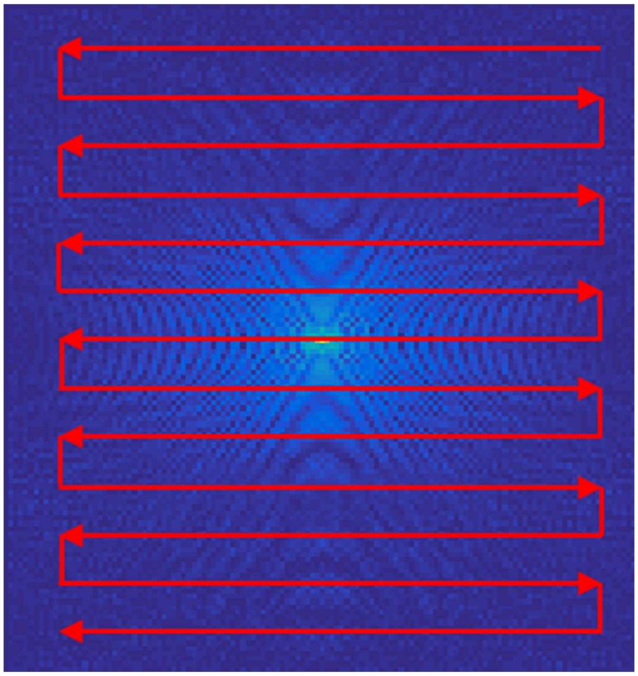

**Figure 2-5. Blipped trajectory used by EPI to traverse the whole *k*-space for data acquistion.**

### 2.1.2 Acceleration by partial *k*-space acquisition

Acquiring partial *k*-space data is a straightforward way to accelerate the scan time. However, as the amount of acquired data cannot satisfy the Nyquist–Shannon criterion, the introduced artefacts degrade the image quality. The kernel of acceleration by under-sampled *k*-space acquisition is exploiting additional information to recover the images with acceptable image quality. Partial Fourier imaging, parallel imaging and compressed sensing reconstruction are the three main branches of this class of acceleration methods.

#### *2.1.2.1 Partial Fourier imaging*

Fast Fourier Transform (FFT), as the key to building the relationship between the *k*-space and image domains, has some inherent mathematical properties that should be exploited. A nice conjugate symmetry property exists in the *k*-space data, specifically for image with a real quantity. In such a case, the signals at two opposite locations in $k$-space has the following relationship: $F(k_x, k_y) = F^*(-k_x, -k_y)$. One example is illustrated in Figure 2-6. In theory, this means that we only need half of the $k$-space data to generate an entire MRI image [20] especially the magnitude information of the image is principally regarded. Two typical practices of this accelerating technique are shown in Figure 2-7 and have been applied to all major brands of MRI scanners as options, and are generally known as read conjugate symmetry ("Partial Echo" by GE and Philips, "Half Echo" by Hitachi, "Asymmetric Echo" by Siemens) and phase conjugate symmetry ("Fractional Numbers of Excitations" by GE, "Half scan" by Philips and Hitachi, "Half Fourier" by Siemens). However, to the cost of reduced scan duration, there is a corresponding reduction in SNR by a factor of $\sqrt{\frac{1}{2}}$ as compared to a comparable fully-sampled sequence. Furthermore, the phase errors introduced in the process of $k$-space data collection will break the conjugate symmetry and make the approximation inaccurate.

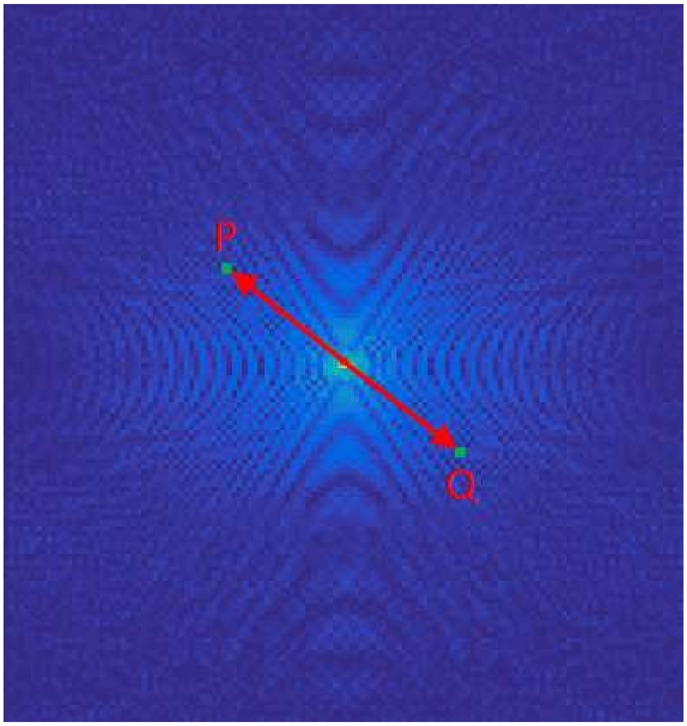

**Figure 2-6. Conjugate Symmetry of FFT in real-value functions. The example shown as is a pair of points P and Q, that are located diagonally across the origin of the *k*-space domain from each other. If the data at P is a complex number *a*+*b*i, the data at Q is immediately known to be P complex conjugate, *a*-*b*i.**

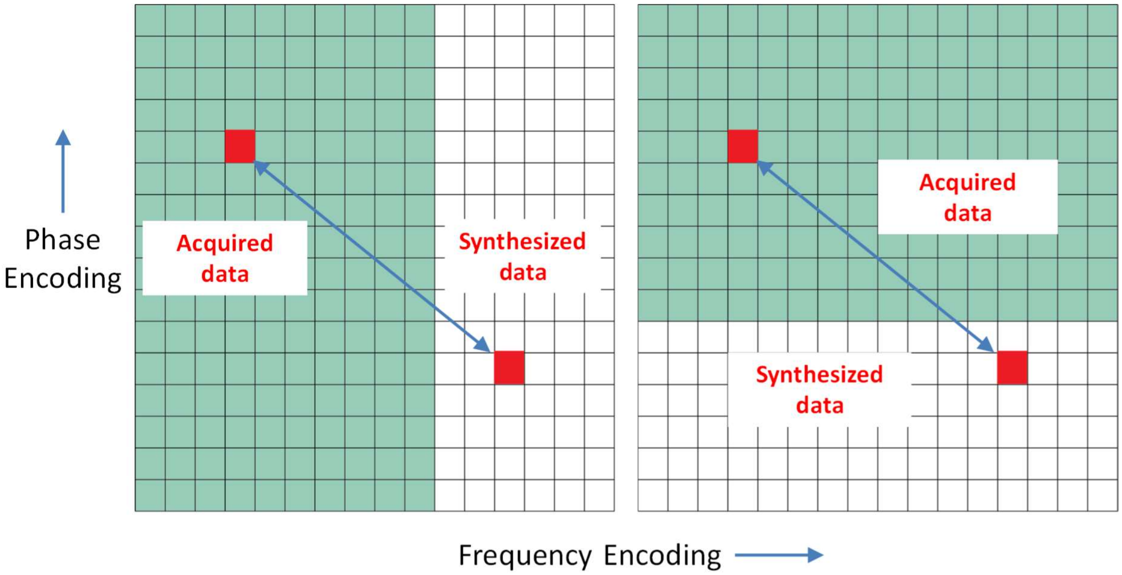

**Figure 2-7. Two types of  partial Fourier imagings. Left: Read-conjugate Symmetry, Right: Phase-conjugate Symmetry.**

*2.1.2.2 Parallel imaging*

Since the 1990s, phased-array coils have been widely used in MRI to improve the SNR [21]. With multiple receivers to acquire signals simultaneously, additional coil information was employed to reconstruct images from acquired partial *k*-space data, which was normally referred to as parallel imaging (PI). In PI, multiple-receiver RF coils are used to implement simultaneous k-space sub-sampling; the object images are then reconstructed with the help of spatial sensitivity information intrinsic to individual coils. One example is illustrated as Figure 2-8.  Four receiver coils were set surrounding an object to detect the MRI signal arising from one selected pixel (see the red dot in Figure 2-8). As each coil has different relative position to the objective tissue, the signal collected by each coil can be defined as a function of position. The difference in sensitivities between individual coil elements in a receive array is well-known as sensitivity maps (see Figure 2-9). The additional information contained by sensitivity maps can unfold wrapped data from each coil and estimate the missing lines of the *k*-space data.

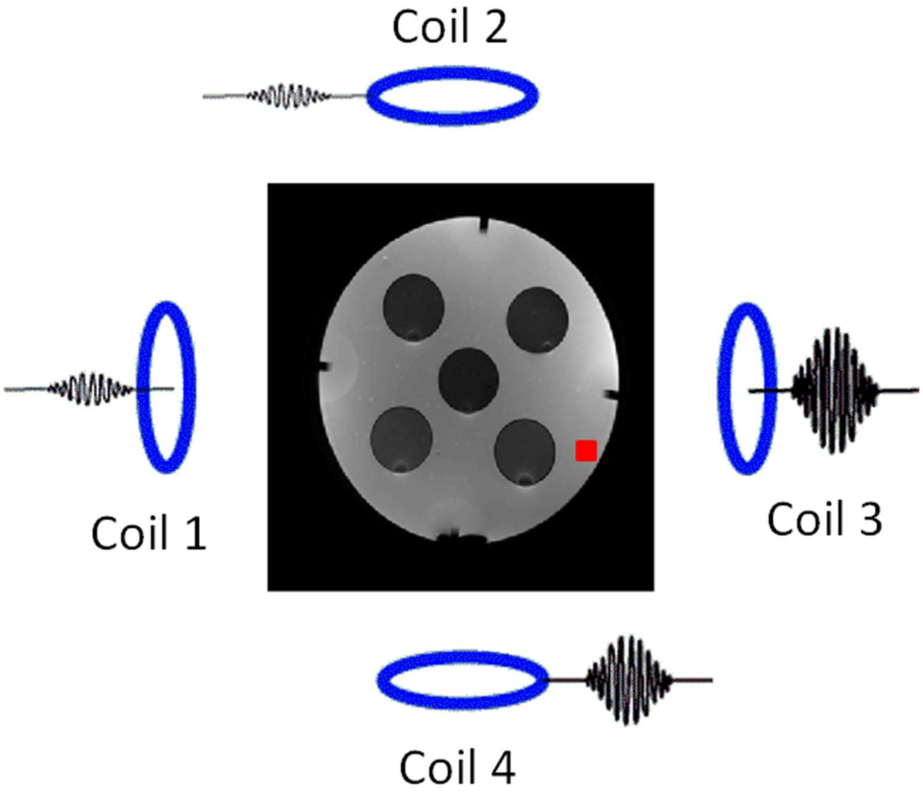

**Figure 2-8. The principle of parallel imaging: use coil sensitivity information to assist in spatial location.**

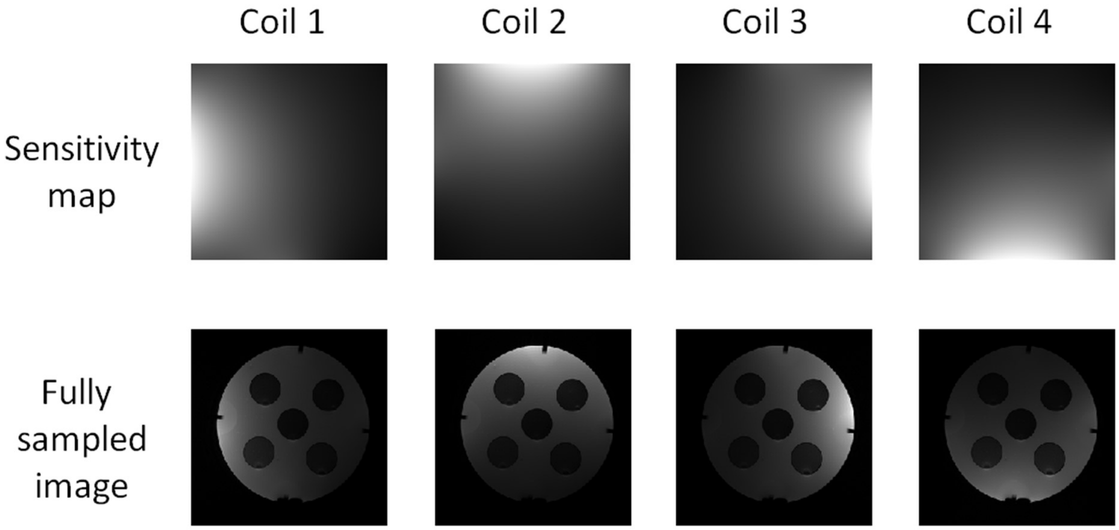

**Figure 2-9. The sensitivity maps and the corresponding fully sampled images of the 4 coil elements as shown in Figure 2-8.**

In the algorithms of PI to reconstruct artefact-free images from the under-sampled *k*-space data of each coil, the sensitivity encoding (SENSE) technique [4, 5] and the generalized auto-calibrating (GRAPPA) technique [6] are used to represent the two general categories. SENSE reconstructs the image in the image domain by acquiring a separate low resolution scan and combining the sensitivity maps to unfold the aliased signals mathematically. GRAPPA reconstructs the images in the *k*-space domain by fully sampling a small central portion of the *k*-space and calculating the missing harmonic *k*-space before standard inverse Fourier transformation. Actually, there is large interchange between the image-based and the *k*-space-based techniques.

PI is widely used in clinical imaging and has proved to be sufficiently robust. The majority of modern MR systems are built using at least one of the parallel imaging methods. The implementation of PI has significantly reduced the image acquisition time and the susceptibility artefacts. Notwithstanding these benefits, this class of acceleration methods is also limited by several factors. First, the acceleration factor of PI is commonly less than the number of coil elements in the receive array. The faithful reconstruction of PI is under the primary assumption that individual coils in the array can provide enough unique spatial information. If the acceleration factor is greater than the number of coil elements, the reconstruction process becomes an underdetermined problem. The additional information provided by sensitivity maps is not sufficient for PI to unfold wrapped images and estimate the missing *k*-space data. This leads to the apparent coherent artefacts and enhanced noise in the reconstructed images [17, 22-24]. One simulation of GRAPPA with four coil elements is illustrated in Figure 2-10. When the acceleration factor is equal to the number of coils, the aliasing artefacts are obvious in the reconstruction of PI (see Figure 2-10c) even in optimal conditions. In practice with the effects such as noises in measurements, the real acceleration factor is far less than the theory limitation to ensure the quality of reconstructed images for diagnosis. The second factor is accuracy of the sensitivity map, which is decided by the geometrical arrangement and correlation of the array [17, 22-24]. Because the kernel of PI reconstruction method is matrix inversion and the matrix is formed by the sensitivity maps, the small error in the estimation of coil sensitivity can be amplified to large errors in the reconstructed images. Limited by the hardware, it is difficult to accurately measure the sensitivity maps. The third consideration is that all PI methods extract a significant penalty in SNR. The reduced *k*-space data acquisition is an inevitable reason for the loss of SNR. The other reason is related to the spatially correlated nature of multiple RF receivers. Factors such as the number, size and orientation of the different coil elements can result in an inhomogeneous SNR within a slice. In addition, the geometric layout of the RF array may not be ideal to provide sufficient independent information to reconstruct the aliased images from each coil [25]. This limits the application of PI to only situations with enough SNR [17, 22-24].

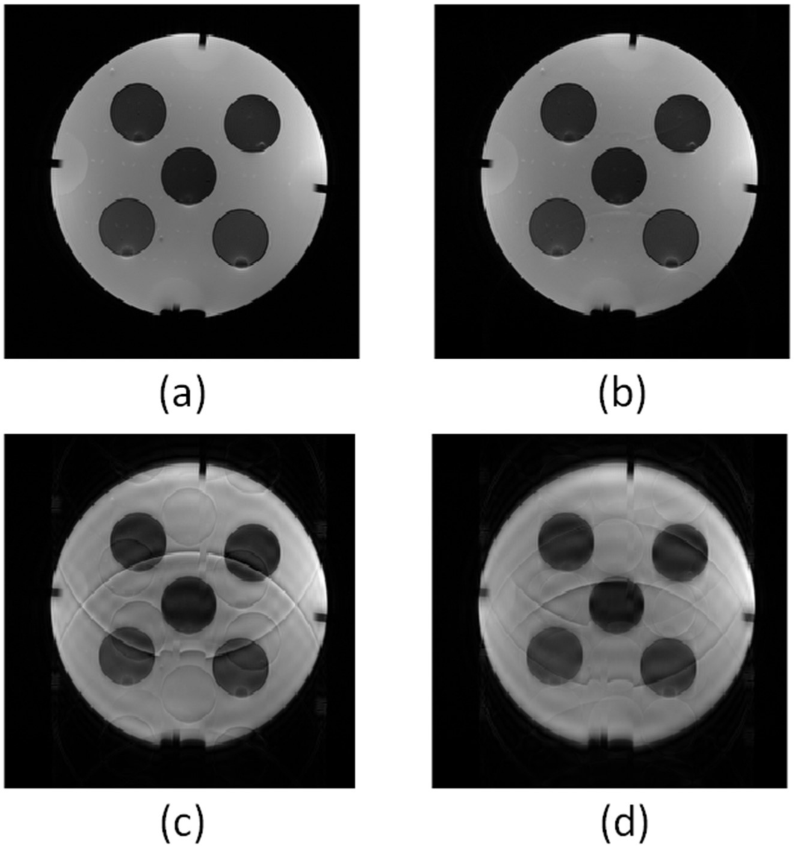

**Figure 2-10. The simulated GRAPPA reconstructions with four coil elements using different acceleration factors. (a) Original image. (b) Recontruction at an acceleration factor of 2. (c) Recontruction at an acceleration factor of 4. (d) Recontruction at an acceleration factor of 6.**

#### *2.1.2.3 Compressed Sensing*

The formerly mentioned two acceleration methods to acquire partial *k*-space data both apply the strategy of regularly missing out the scanning line and combining the additional information to perfectly reconstruct the image in ideal situation. In contrast to these two kinds of methods, Compressed Sensing applies a random under-sampling scheme to make the artefacts noise-like. Meanwhile, CS tends to make the reconstructed image approximate to the original one in a high possibility instead of an extra accurate reconstruction. The concept of CS was theoretically elucidated by Donoho [7] and its application in MRI was later introduced by Lustig et al [8]. Figure 2-11 shows the flowchart of the process of applying CS in MRI. The design of the under-sampling pattern and the optimal reconstruction algorithm are the kernels of CS MRI, which will be further investigated in section 2.3. First, an overview of the theory of CS will be presented.

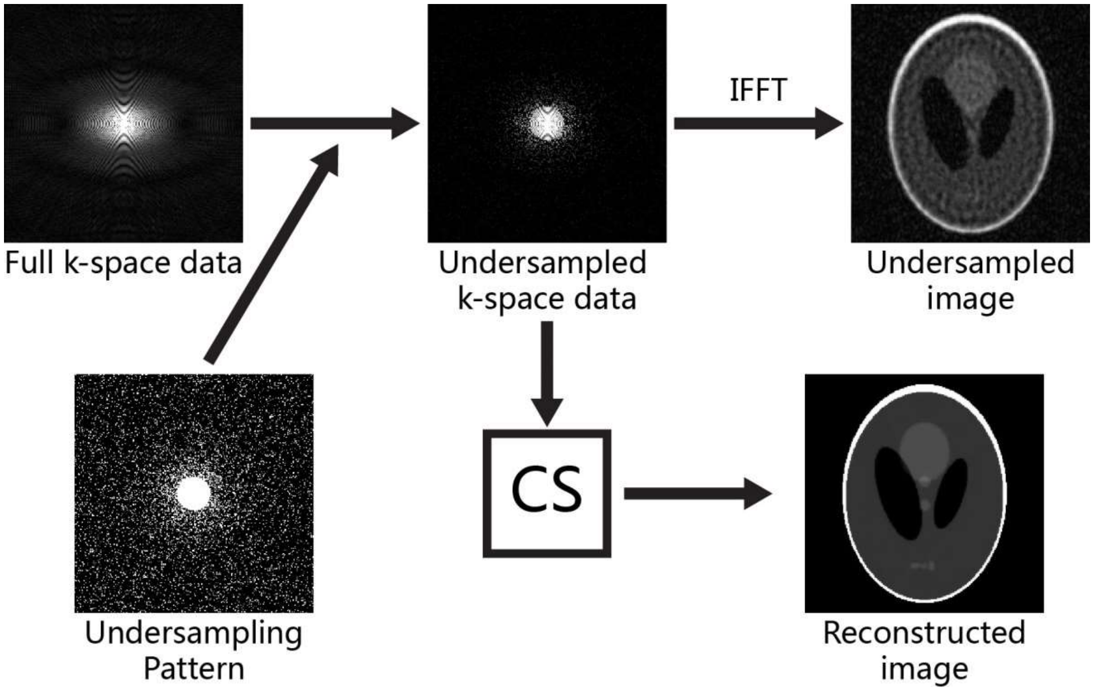

**Figure 2-11. The flowchat of applying CS in MRI.**

## 2.2 The fundamentals of Compressed Sensing

The limitation of achieving enough samples can occur in multiple scenarios, such as limited number of data capturing devices, expensive cost in measurement or high time consumption in capturing data, like MRI. As a new mathematical framework, CS theory provides a promising solution. Banking on finding sparse solutions to underdetermined linear systems, CS asserts that the signals can be reconstructed from far less sampled data than required by the traditional Nyquist paradigm [11]. Essentially, CS merges compression into sampling, which measures only the important coefficients of the signals during the acquisition by compression and enables near-perfect reconstruction of the original signals.

To precisely state the problem mathematically, suppose the N dimensional signal $\boldsymbol{x} \in \boldsymbol{R}^{\mathrm{N}}$ be our signal of interest. As prior information, $\boldsymbol{x}$ is assumed to have the property of *sparsity*, which means very few entries of the signal have non-zero coefficients. Further, let $\boldsymbol{A}$ be a $\mathrm{M} \times \mathrm{N}$ matrix as *sensing matrix*, which acquires $\mathrm{M} \ll \mathrm{N}$ measurements. The Compressed Sensing problem can be formulated as recovering $\boldsymbol{x}$ from the knowledge of $\boldsymbol{y} = \boldsymbol{A}\boldsymbol{x}$.

Now, we face an underdetermined linear system with infinite solutions. Therefore, the theory of CS has three key elements to guarantee the unique reconstruction. The subsequent sections are built up by these three elements: sparsity, sensing matrix, and recovery algorithms.

### 2.2.1 Sparsity

The obtained signal with the property of sparsity is the prior assumption of CS theory. Fortunately, many natural signals such as sound and image signals can become sparse in terms of their projection on suitable basis. For example, a single-frequency sine wave does not exhibit sparsity when recorded over a time domain. However, using the Fourier transform, the transformed vector has all its information in two peaks in the frequency domain. If an image is taken, as shown in Figure 2-12(a), the majority of the coefficients in the image matrix are large (indicated by a lighter colour). Meanwhile, it is well known that a variety of representation systems, such as discrete cosine transforms (DCT), total variation (TV), wavelets [26, 27] and shearlets [28], can provide sparse approximations of most natural images. Figure 2-12(b) illustrates the wavelet decomposition of


(a) (b)

**Figure 2-12. Sparse represenation of an image via a multiscale wavelet transform. (a) Original image. (b) Wavelet representation. Pixels with large coefficients are represented by light colour, while pixels with small coefficients are represented by a dark colour. Observe that most of the wavelet coefficients are close to zero.**

Figure 2-12(a). It can be clearly seen that most coefficients have a small absolute value, indicated by a darker colour. By setting the small coefficients to zero, we can obtain a good approximation of the original image, as the example in Figure 2-13 shows. Hence, sparsity can indeed provide a reasonable foreknowledge of the signals to be sensed. The common notion of sparsity states that a vector has at most *s* non-zero coefficients as a *s*-sparse signal.


(a) (b)

**Figure 2-13. Sparse approximaiton of a natural image. (a) Original image. (b) Approximation of the image obtained by reserving only the largest 10% of the wavelet coefficients in (a).**

**Definition** 2.1: Signal $\boldsymbol{x}$ is defined as *s*-sparse if:

$$\|\boldsymbol{x}\|_0 = \#\{i: x_i \neq 0\} \leq s \qquad (2\text{-}1)$$

where $\boldsymbol{x} = (x_i)_{i=1}^{N} \epsilon\, \boldsymbol{R}^N$, $\|\cdot\|_0$ is the $l_0$ norm, the symbol # donates a number sign. The set of all *s*-sparse vectors is denoted as $\sum_{\boldsymbol{s}}$ [29].

Generally, the signals we deal with are not themselves sparse, but which admit a sparse representation in a proper basis $\boldsymbol{\varphi}$. In this case, we will still refer to $\boldsymbol{x}$ as being *s*-sparse.

**Definition** 2.2: Signal $\boldsymbol{x}$ is defined as *s*-sparse in basis $\boldsymbol{\varphi}$ if:

$$\boldsymbol{x} = \sum_{\mathrm{i}=1}^{\mathrm{N}} \varphi_{\mathrm{i}} \alpha_{\mathrm{i}}\,,\ \mathbf{s.t.}\ \|\boldsymbol{\alpha}\|_0 = \#\{i: \alpha_i \neq 0\} \leq s \qquad (2\text{-}2)$$

where the basis $\boldsymbol{\varphi} = (\varphi_i)_{i=1}^{N} \epsilon\, \boldsymbol{R}^{\mathrm{N}}$, which herein is called the ‘sparsity basis’ [29].

### 2.2.2 Sensing matrix

In the case where the original signal $\boldsymbol{x}$ is sparse, the design of sensing matrix $\boldsymbol{A}$ is critical to ensure it can preserve the information in the signal [30]. In this segment, the emphasis is on the desirable properties of sensing matrix $\boldsymbol{A}$, which prove the accurate recovery of signal $\boldsymbol{x}$ from the measurements $\boldsymbol{y} = \boldsymbol{Ax}$.

*2.2.2.1 Null space condition*

In order to get the unique recovery of $\boldsymbol{x}$ from measurements $\boldsymbol{y} = \boldsymbol{Ax}$, any pair of distinct vectors $\boldsymbol{x}, \boldsymbol{x}' \in \sum_s$ should make $\boldsymbol{Ax} \neq \boldsymbol{Ax}'$. Otherwise, it is impossible to distinguish $\boldsymbol{x}$ from $\boldsymbol{x}'$ with only the measurements $\boldsymbol{y}$. If $\boldsymbol{Ax} = \boldsymbol{Ax}'$ is observed, we can get $\boldsymbol{A}(\boldsymbol{x} - \boldsymbol{x}') = 0$ with $\boldsymbol{x} - \boldsymbol{x}' \in \sum_{2s}$. It means that $\boldsymbol{A}$ can uniquely represent all $\boldsymbol{x} \in \sum_s$ if and only if $N(\boldsymbol{A})$ contains no vector in $\sum_{2s}$, where $N(\boldsymbol{A}) = \{\boldsymbol{z} : \boldsymbol{Az} = 0\}$ is the null space of $\boldsymbol{A}$. As there are many equivalent ways to characterize the property, we introduce the most common one: spark [31].

**Definition** 2.3: Given an $M \times N$ matrix $\boldsymbol{A}$, the spark of $\boldsymbol{A}$ is the minimum number of linearly-dependent columns within $\boldsymbol{A}$, denoted by ***spark(A)***.

**Lemma** 2.1: Given an $M \times N$ matrix $\boldsymbol{A}$, then

$$\boldsymbol{spark}(\boldsymbol{A}) = \min\{s: N(\boldsymbol{A}) \cap \textstyle\sum_s \neq \{0\}\} \tag{2-3}$$

and $\boldsymbol{spark}(\boldsymbol{A}) \in [2, \mathrm{M} + 1]$.

Straightforwardly, the notion enables us to derive the following guarantee.

**Theorem** 2.1 [31]: For any vector $\boldsymbol{y} \in \boldsymbol{R}^{\mathrm{M}}$, there exists at most one solution $\boldsymbol{x} \in \sum_s$, such that $\boldsymbol{y} = \boldsymbol{Ax}$ if and only if $\boldsymbol{spark}(\boldsymbol{A}) > 2\mathrm{s}$.

Therefore, Theorem 2.1 yields that the minimum amount of measurements for unique recovery should satisfy $\mathrm{M} \geq 2\mathrm{s}$.

The spark provides a complete characterization of exactly sparse vectors. However, the signals we deal with in practice are often approximately sparse. Thus, more restrictive conditions should be considered for the null space of $\boldsymbol{A}$.

**Definition** 2.4 [29]: Given an $M \times N$ matrix $\boldsymbol{A}$, it satisfies the null space property (NSP) of order $s$ if there exists a constant $C > 0$ for all h $\in N(\boldsymbol{A})$ and all index sets $|\Lambda| \leq k$ such that,

$$||h_\Lambda||_2 \leq C \frac{||h_{\Lambda^c}||_1}{\sqrt{s}} \tag{2-4}$$

where $\Lambda \subset \{1,2, \dots, N\}$ is a subset of indices and $\Lambda^C = \{1,2, \dots, N\} \backslash \Lambda$, $h_\Lambda$ is the length N vector by setting the entries of h indexed by $\Lambda^C$ to zero.

To illustrate the implications of NSP in dealing with general non-sparse $\boldsymbol{x}$, the following theorem states how to measure the performance of sparse recovery by NSP.

**Theorem** 2.2 [32]: Let $\boldsymbol{A}: \boldsymbol{R}^\mathrm{N} \rightarrow \boldsymbol{R}^\mathrm{M}$ denote a sensing matrix and $\Delta: \boldsymbol{R}^\mathrm{M} \rightarrow \boldsymbol{R}^\mathrm{N}$ denote an arbitrary recovery algorithm. If the pair $(\boldsymbol{A}, \Delta)$ satisfies:

$$||\Delta(\boldsymbol{Ax}) - \boldsymbol{x}||_2 \leq C \frac{\sigma_s(\boldsymbol{x})_1}{\sqrt{s}} \tag{2-5}$$

then $\boldsymbol{A}$ must necessarily satisfy the NPS of order 2$s$, where $\sigma_s(\boldsymbol{x})_1 = \min_{\hat{\boldsymbol{x}} \in \sum_s} ||\boldsymbol{x} - \hat{\boldsymbol{x}}||_1$ and $\hat{\boldsymbol{x}} \in \sum_{\boldsymbol{s}}$.

This guarantees the NSP of order 2s is sufficient to exactly recover all possible $s$-sparse signals, but also ensures the robustness to recover non-sparse signals directly depending on how well the signals are approximated by $s$-sparse vectors [29].

*2.2.2.2 The restricted isometry property*

While NSP is both necessary and sufficient for guaranteeing the exact recovery of sparse signals, it is under the scenario without the consideration of noise. So it is necessary to consider stronger conditions in practice when facing the noise contaminated measurements or quantization errors. To address this, an isometry condition was introduced for matrix $\boldsymbol{A}$ [33] in following notion.

**Definition** 2.5: Given an $M \times N$ matrix $\boldsymbol{A}$, it satisfies the restricted isometry property (RIP) of order $s$, if there exists a $\delta_s \in (0,1)$ such that

$$(1 - \delta_s)||\boldsymbol{x}||_2^2 \leq ||\boldsymbol{Ax}||_2^2 \leq (1 + \delta_s)||\boldsymbol{x}||_2^2 \quad \text{for all} \quad \boldsymbol{x} \in \textstyle\sum_s \tag{2-6}$$

To any measurements vectors $\boldsymbol{y_1} = \boldsymbol{Ax_1}$ and $\boldsymbol{y_2} = \boldsymbol{Ax_2}$ $\boldsymbol{y} = \boldsymbol{Ax}$, RIP measures whether the distance between the two vectors is proportional to distinguish the correlated sparse signals $\boldsymbol{x_1}$ and $\boldsymbol{x_2}$. Thus, the fulfilment of the RIP is sufficient for many algorithms to be able to successfully recover a sparse signal from noisy measurements and maintain the stability of solutions. The notion automatically ensures the robustness to noise and establishes its critical role in CS.

In the application of CS, we also need to consider how many measurements are adequate to satisfy the RIP. The following theorem [34] establishes the measurement bounds.

**Theorem** 2.3: Given an $M \times N$ matrix $\boldsymbol{A}$, that satisfies the RIP of order $2s$ with constant $\delta \in \left(0, \frac{1}{2}\right]$. Then

$$M \geq Cslog\left(\frac{N}{s}\right) \tag{2-7}$$

where $C = \frac{1}{2log(\sqrt{24}+1)} \approx 0.2817$.

As mentioned formerly, the RIP is a strictly stronger than the NSP. The following notion [29] will prove that if a matrix satisfies the RIP, then it will also satisfy the NSP.

**Theorem** 2.4: Given an $M \times N$ matrix $\boldsymbol{A}$, it satisfies the RIP of order 2s with constant $\delta_{2s} < \sqrt{2} - 1$. Then $\boldsymbol{A}$ satisfies the NSP of order 2s with constant

$$C = \frac{\sqrt{2}\delta_{2s}}{1-(\sqrt{2}+1)\delta_{2s}} \tag{2-8}$$

*2.2.2.3 Mutual coherence*

Apparently, spark, NSP and RIP can be part of the design criteria of a sensing matrix. However, there is a combinatorial computational complexity in verifying whether a matrix $\boldsymbol{A}$ can satisfy any of these criteria. As in each case, there exist $C_S^N$ submatrices that need to be essentially considered. When applying CS to large-scaled signals, it is NP hard and prohibitive. In practice, we prefer to utilize the properties of $\boldsymbol{A}$ which are computable to provide more substantive guarantees. The mutual coherence of the matrix is one option [35-36].

**Definition** 2.6: The mutual coherence of a given $M \times N$ matrix $\boldsymbol{A}$, denoted as $\mu(\boldsymbol{A})$, is the largest absolute inner product between any two columns $\alpha_i, \alpha_j$ of $\boldsymbol{A}$:

$$\mu(\boldsymbol{A}) = \max_{i \neq j} \frac{|\langle \alpha_i, \alpha_j \rangle|}{\|\alpha_i\|_2 \|\alpha_j\|_2} \in \left[\sqrt{\frac{N-M}{M(N-1)}}, 1\right] \tag{2-9}$$

The upper bound of $\mu(\boldsymbol{A})$ is straightforward to calculate in the case that two columns of the matrix are linearly dependent. The lower bound of $\mu(\boldsymbol{A})$, known as the famed Welch bound [37], can be reached by the optimal Grassmannian frames [38]. Meanwhile, as $\mathrm{M} \ll \mathrm{N}$ is assumed in the statement of CS, the lower bound can be further approximated as $\mu(\boldsymbol{A}) \geq \frac{1}{\sqrt{M}}$.

The mutual coherence can also be related to the formerly introduced spark, NSP and RIP by some explicit constructions.

**Lemma 2.2**: For any matrix $\boldsymbol{A}$,

$$\boldsymbol{spark}(\boldsymbol{A}) \geq 1 + \frac{1}{\mu(\boldsymbol{A})} \tag{2-10}$$

By merging Theorem 2.1 with Lemma 2.2, the uniqueness can be guaranteed if the following condition is posed on matrix $\boldsymbol{A}$.

**Theorem 2.5**: Given an $M \times N$ matrix $\boldsymbol{A}$, if

$$s \leq \frac{1}{2}\left(1 + \frac{1}{\mu(\boldsymbol{A})}\right) \tag{2-11}$$

Then for each measurement vector $\boldsymbol{y} \in \boldsymbol{R}^{\mathrm{M}}$, there exists at most one signal $\boldsymbol{x} \in \sum_{\boldsymbol{s}}$ such that $\boldsymbol{y} = \boldsymbol{Ax}$.

Together with the lower bound of $\mu(\boldsymbol{A})$ in Equation (2-10), Theorem 2.5 provides the upper bound on the level on signal sparsity *s* for a unique recovery using mutual coherence: $s = O(\sqrt{M})$.

Theorem 2.5 also connects mutual coherence to RIP as shown follows:

**Lemma 2.3** [29]: If $\boldsymbol{A}$ has unit-norm columns and mutual coherence $\mu(\boldsymbol{A})$, then $\boldsymbol{A}$ satisfies the RIP of order *s* with $\delta = (s-1)\mu(\boldsymbol{A})$ for all $s < \frac{1}{\mu(\boldsymbol{A})}$.

These relations allow us to easily compute or estimate other properties, if a sensing matrix is constructed for a particular one.

### 2.2.3 Recovery algorithm

Based on the preconditions that the original signal $\boldsymbol{x} = \boldsymbol{\varphi\alpha}$ is $s$-sparse in basis $\boldsymbol{\varphi}$ and given measurements $\boldsymbol{y} = \boldsymbol{Ax}$ provides an assurance of accurate recovery, it is intuitive to consider recovering $\boldsymbol{x}$ by constructing an optimization problem to ensure the signal sparsity as:

$$\widehat{\boldsymbol{\alpha}} = arg \min_{\boldsymbol{z}} \|\boldsymbol{z}\|_0 \text{ subject to } \boldsymbol{z} \in \boldsymbol{\beta}(\boldsymbol{y}) \tag{2-12}$$

where $\boldsymbol{\beta}(\boldsymbol{y}) = \{\boldsymbol{z}: \boldsymbol{A\varphi z} = \boldsymbol{y}\}$ or $\boldsymbol{\beta}(\boldsymbol{y}) = \{\boldsymbol{z}: \|\boldsymbol{A\varphi z} - \boldsymbol{y}\|_2 \leq \epsilon\}$ to ensure that $\widehat{\boldsymbol{x}} = \boldsymbol{\varphi}\widehat{\boldsymbol{\alpha}}$ is consistent with the measurements $\boldsymbol{y}$.

Under the suitable assumptions on sensing matrix $\boldsymbol{A}$, the perfect recovery exists in probability [39, 40]. While the objective $l_0$ norm minimization is nonconvex, it has combinatorial complexity, which is not rewarding to solve it in practice. Finding a solution for a general matrix $\boldsymbol{A}$ to approximate the true minimum is considered to be NP-hard [41].

One alternative is to translate the problem into another tractable form, such as to replace $\|\cdot\|_0$ ($l_0$ norm) with its closest convex approximation $\|\cdot\|_1$($l_1$ norm) [42-52], which is denoted as:

$$\|\boldsymbol{x}\|_1 = \sum_{i=1}^{N} |x_i| \tag{2-13}$$

This leads Equation (2-12) to the following optimization problem, which is also known as basis pursuit (BP):

$$\widehat{\boldsymbol{\alpha}} = arg \min_{\boldsymbol{z}} \|\boldsymbol{z}\|_1 \text{ subject to } \boldsymbol{z} \in \boldsymbol{\beta}(\boldsymbol{y}) \tag{2-14}$$

Provided that objective function is convex, Equation (2-14) has the computational complexity which is polynomial with the signal length [53]. Furthermore, when $\boldsymbol{\beta}(\boldsymbol{y}) = \{\boldsymbol{z}: \boldsymbol{A\varphi z} = \boldsymbol{y}\}$, the optimization problem can be adapted as a linear program [38].

Translating $l_0$ minimization to $l_1$ minimization not only deduces a provably accurate recovery, but also leads to the ability to utilize a tremendous number of different algorithms, which are designed to give efficient and accurate numerical solution in the context of CS. In the following section, we will briefly overview three typical types of algorithms: convex optimization, greedy algorithm and combinatorial algorithms.

*2.2.3.1 Convex optimization*

Equation (2-14) has illustrated the constrained version of the convex optimization. Meanwhile, there are several equivalent forms of this problem. In the literature [54, 55], the unconstrained version is the one used by the majority of convex optimization algorithms, and is shown as follows:

$$\widehat{\boldsymbol{x}} = arg\ \min_{\boldsymbol{z}} \frac{1}{2} \|\boldsymbol{A\varphi z} - \boldsymbol{y}\|_2 + \lambda \|\boldsymbol{z}\|_1 \tag{2-15}$$

where $\lambda$ is a particular parameter to make these two problems equivalent.

Basis Pursuit (BP) [42], Basis Pursuit De-Noising (BPDN) [42], modified BPDN [56] are the popular algorithms of convex optimization. In addition to the BP-based solutions, various adapted convex optimization algorithms predated the field of CS, such as interior-point methods [10], projected gradient methods [57], and iterative thresholding methods [58]. All these algorithms solve the sparse recovery problem by linear programming [59], which requires very few measurements for exact reconstruction, but is computationally costlier.

*2.2.3.2 Greedy algorithms*

To balance the computational complexity and number of measurements, greedy algorithms do a good trade-off in solving the sparse representations [39, 60-70]. Relying on iterative approximation of the coefficients and the support of the signals, this class of algorithms display superiorities in execution speed and implementation. The approximated solutions are guaranteed to have remarkably similar performance to those obtained by convex optimization approaches [29].

There are two well-known simplest greedy approaches: Orthogonal Matching Pursuit (OMP) [67, 71] and Iterative hard thresholding (IHT) [72]. The OMP approach finds the columns of sensing matrix $\boldsymbol{A}$ most correlated with the measurements in a greedy fashion. At each iteration, the least square error of the partial estimate and the original measurement is minimized. The stopping criterion can be either the maximum number of iterations or minimum signal residual. The IHT approach implements a more straightforward way to iterate a gradient descent step followed by hard thresholding until meeting the stop criterion of convergence. However, the performance of this kind of algorithm in computational costs will degrade when the recovered signal is not very sparse [11].

*2.2.3.3 Combinatorial algorithms*

Compared to convex optimization and greedy algorithms, combinatorial algorithms are extremely fast and efficient. To the $s$-sparse signal $\boldsymbol{x} \in \boldsymbol{R}^{\mathrm{N}}$, the complexity of the convex optimization and greedy algorithms is at least linear to N [29]. Meanwhile, the complexity of combinatorial algorithms can be linear to the $s$ [29, 73, 75]. However, the advantage in calculation speed is based on many specific measurements, which requires the broad freedom in designing the sensing matrix $\boldsymbol{A}$. The full control over sensing matrix $\boldsymbol{A}$ limits the practical application. Heavy Hitters on Steroids (HHS) pursuit [74], Chaining Pursuits [76] and sub-linear Fourier transform [77] are typical examples of this class of algorithms [11, 29].

## 2.3 The application of Compressed Sensing in MRI

### 2.3.1 Requirements of applying CS for MRI

As mentioned in section 2.1, the data acquired by MRI is in the frequency domain (*k*-space) which means each sample is the linear combination of all the image pixels. In addition, most of MR images are represented sparsely in an appropriate transform domain [8]. Both the coded nature of MR acquisition and the transform sparsity of other MR images, reveal the natural fit between CS and MRI [8, 9, 26]. Generally, the successful application of CS in MRI is based on three fundamental requirements: transform sparsity, incoherence of under-sampling artefacts and nonlinear reconstruction.

*2.3.1.1 The transform sparsity of MR images*

The sparsity of MR images can be well demonstrated by a series of sparsifying transform. The main challenge is choosing the appropriate transform for a particular sort of MR images to exploit the sparsity. The total variation (TV) sums the gradients in intensity between neighbouring pixels [17]. The summary of the absolute variations in the pixels has a compressive performance in MR angiography, which is already sparse in the image domain and primarily used to detect boundaries of the blood vessels [8]. Meanwhile, it is often used as a finite-difference penalty as well when other sparsifying transforms are implemented in the objectives [8, 63]. Wavelet transforms, which are central to the JPEG-2000 image compression standard [78], have proved to be a powerful sparsity constraint for nature and real-life images [8]. As a multiscale representation, both the coarse and fine details can be identified by the corresponding coefficients. The coefficients also offer the information in the time and frequency domains simultaneously. For brain and cardiac images, wavelet transforms have advantages in handling the textures of these images [8]. Singular value decomposition (SVD), well known as a factorization of a matrix in linear algebra, has also validated its advance as a sparsifying transform with properties of being data adaptive and having low computational complexity [79]. In dynamic MRI, the spatiotemporal correlations within different frames can be exploited and the sparsity in different dimensions can be extended by 3D wavelet transform or Higher-order Singular Value Decomposition (HOSVD) [80].

The joint use of different sparsifying transforms and other prior knowledge can further reduce the sparsity of images to improve the reconstructions of CS. However, deciding how to balance the weightings between different constraints and determine the optimal values is becoming more complex as the number of constraints increase [17].

#### *2.3.1.2 Pseudo-random under-sampling pattern*

As mentioned in section 2.2.1, the sparsity provides an estimation for the number of *k*-space data implementers that need to be sampled to get an accurate reconstruction. With the number of samples, the design of the under-sampling scheme has an impact on the performance of CS MRI. According to the criteria in section 2.2.2, the artefacts introduced by *k*-space under-sampling should be noise-like (incoherent) in the sparsifying transform domain [8]. The Monte-Carlo design procedure is implemented to find an optimal under-sampling pattern that maximizes the incoherence for a limited number of samples [8].

Another consideration arises from the non-uniform energy distribution of the MR image in the *k*-space, as the majority of the *k*-space energy concentrates near the origin part and fall away rapidly towards the periphery [8]. To address these two issues, the variable density random under-sampling pattern was put forward and is extensively used in CS MRI [81].

Although the real random under-sampling scheme proves to have perfect performance in CS MRI, using the relative under-sampling trajectory to get a true random subset of the *k*-space is almost infeasible. As in any practice, any trajectory must follow the MRI hardware and corresponding physiological constrains [8]. As mentioned in section 2.1, Cartesian and non-Cartesian trajectories are the two types of sampling trajectories in practise. A Cartesian grid is the most commonly used trajectory in MRI because of its robustness in data collection, practical implementation and simple reconstruction. However, in its application for CS, the random phase-encode under-sampling by

Cartesian trajectory is demonstrated to be coherent when compared with real random under-sampling [8]. The main reason is that the incoherence of random phase-encode under-sampling is only in one dimension (the phase-encoding direction). In addition, the uniform weighting of the *k*-space collection in the Cartesian grid contradicts the non-uniform *k*-space energy distribution. It brings with it the burden of an under-sampling scheme to keep the balance between central and periphery parts acquisition. In the section 1.1, we have illustrated the performance degradation in CS MRI caused by the limitation of the random phase-encode under-sampling design and the related solutions used to improve the quality of the reconstructed images. For the non-Cartesian approaches such as radial and spiral trajectories, the non-uniform sampling density agrees with the *k*-space distribution to gain higher SNR and collect more important data points for a faithful reconstruction. Nevertheless, as mentioned in section 1.1, there is no fast and accurate Fourier transform for a non-Cartesian grid to connect the frequency and image domains [82]. This limitation restricts the extent of applications of non-Cartesian trajectories in CS MRI.

### *2.3.1.3 Image reconstruction*

In addition to an appropriate sparsifying transform and a suitable under-sampling pattern, the reconstruction algorithm is the last element to decide the final performance of CS MRI.

Adapted from equation (2-12), the reconstruction problem in CS MRI can be depicted as follows: Suppose $\boldsymbol{I}$ is an object MR image with N × N pixels, which has a sparse representation in a basis $\boldsymbol{\Psi}$. A subset of its full k-space measurements is obtained using certain under-sampling patterns. The constrained optimization problem for reconstruction is

$$Minimize: \|\boldsymbol{\Psi}(\boldsymbol{m})\|_0,\ subject\ to\ \|\boldsymbol{P}\boldsymbol{\varphi}(\boldsymbol{m}) - \boldsymbol{y}\|_2 < \varepsilon \qquad (2\text{–}16)$$

where $\|\cdot\|_0$ is the number of nonzero components, $\boldsymbol{\Psi}$ denotes the sparse transform, $\boldsymbol{m}$ is the reconstructed image, $\boldsymbol{\varphi}$ the Fourier transform, $\boldsymbol{P}$ the random under-sampling pattern, $\boldsymbol{y}$ consists of the measurements, and ε is the tolerance that controls the reconstruction data fidelity and relates to the expected noise level.

In contrast to the theoretical analysis of the recovery algorithm in section 2.2.3, the primary consideration of applying CS in MRI is the balance between the sparsity of the image representation and the consistency of the acquired *k*-space data. Due to the non-linear reconstruction process of CS, the computational cost and efficiency of the algorithm cannot satisfy the requirement of real-time imaging in rapid MRI.

Considering these constraints, the nonlinear conjugate gradient (NCG) method has been widely used and well investigated in CS MRI. NCG calculates the gradient direction of equation (2-16) and the length of the step along this direction to do a line-search. The strong robustness renders it have a stable performance in different scenarios, while the reconstruction time of NCG limits its further application in CS MRI as it is an iterative algorithm. Recently, a fast composite splitting algorithm (FCSA) was proposed as an efficient algorithm to shorten the optimization time for reconstruction [83]. FCSA separated equation (2-16) into the terms of a least square data fitting and $l_1$ norm regularization. By existing techniques, the two sub-problems can be solved efficiently. The reconstruction can be obtained by the weighted linear combinations of the two sub-problems' solutions. These processes render FCSA the properties of strong convergence and low computation complexity. In order to handle the fast imaging challenge in dynamic MRI, *k*-t space FOCal underdetermined system solver (*k*-t FOCUSS) raised the idea to exploit the data sparsity along the temporal dimension and provided high resolution reconstructions [84]. All these reconstruction algorithms make the application of CS in MRI more feasible and extend the implements of CS MRI.

### 2.3.2 Typical applications of CS in MRI

#### *2.3.2.1 Dynamic contrast enhanced (DCE) Imaging*

DCE MRI can provide the information about physiological tissue characteristics, which makes it an effective non-invasive diagnosis method for tissues or tumours. In DCE MRI, the increasing spatial resolution and temporal resolution can provide more morphological information of tumours and kinetic analysis [26]. However, the corresponding lengthy scan time by conventional fully-sampled MRI will introduce the motion artefacts by the movement of objective organs especially in liver or kidney with breathing motion. So there is a conflict between the requirements to have fine anatomical details and fast acquisition to get accurate images in conventional method.

Many studies reveal the power of applying CS in DCE. Reference [85] under-sampled each *k*-space data frame randomly to acquire more images per time (improving temporal resolution) and obtain high resolution reconstruction with the help of a reference image obtained in advance. In reference [86], a method was proposed to combine CS and PI to accelerate the scanning. The results of arterial and venous phase imaging by DCE liver MRI in eight volunteers was compared with standard breath-hold Cartesian 3D MRI, which demonstrated the performance. In reference [87], a DCE-MRI with eightfold acceleration rate in perfusion measurement proved the capacity of CS in heart imaging by exploiting the temporal redundancy.

#### *2.3.2.2 Cardiac Imaging*

The majority of morbidity and mortality in heart diseases are caused by myocardial infarction and heart failure [26, 88]. Cardiac MRI can create both still and dynamic images with high resolution as well as high soft tissue contrast to detect the relative diseases. However, the current Cardiac MRI is constrained by not only the slow data acquisition to produce images with high temporal and spatial resolution, but also the contaminated images by motion artefacts.

One approach taken in reference [89] presented a four-fold accelerated cardiac perfusion MRI through exploiting the sparsity of the dynamic image set in x-f space and employing *k*-t random under-sampling by CS. Combined with PI, a joint reconstruction approach, named *k*-t JOCS (joint CS) can highly accelerate the acquisition (more than six-fold) by using Fourier transform in time and spatial TV [89]. Another approach also merges CS into PI in Cardiac MRI to evaluate left ventricular volumes and function with high accuracy in patients with the acceleration rate up to 11 [90].

#### *2.3.2.3 Angiography*

Magnetic resonance angiography (MRA) is a medical imaging technique based on MRI to visualize vascular structures for evaluation of abnormalities. The most frequently applied MRA use intravenous contrast agents for imaging and the dynamics of the contrast agents contains the important diagnosis information. The accuracy of capturing the dynamics depends on the spatial and temporal resolution of MRI. The application of CS in MRA is particularly suitable. The inherent sparse represention of angiography data in both wavelet and finite difference domain highlight the potential of the CS-based MRA. It can strongly improve the temporal and spatial resolution without increasing scanning time and suppressing the artefacts from under-sampling.

An example [8] of contrast-enhanced 3D angiography reconstruction results is illustrated in Figure 2-14. With the increase of acceleration rate, we can note the diffused boundaries in the reconstructions by low-resolution and the increase of apparent noise in the reconstructions by zero-filling with density compensation. In contrast, the CS method exhibits good reconstructions and preserves the good sharp boundaries of the very bright vessels, even at high accelerations.

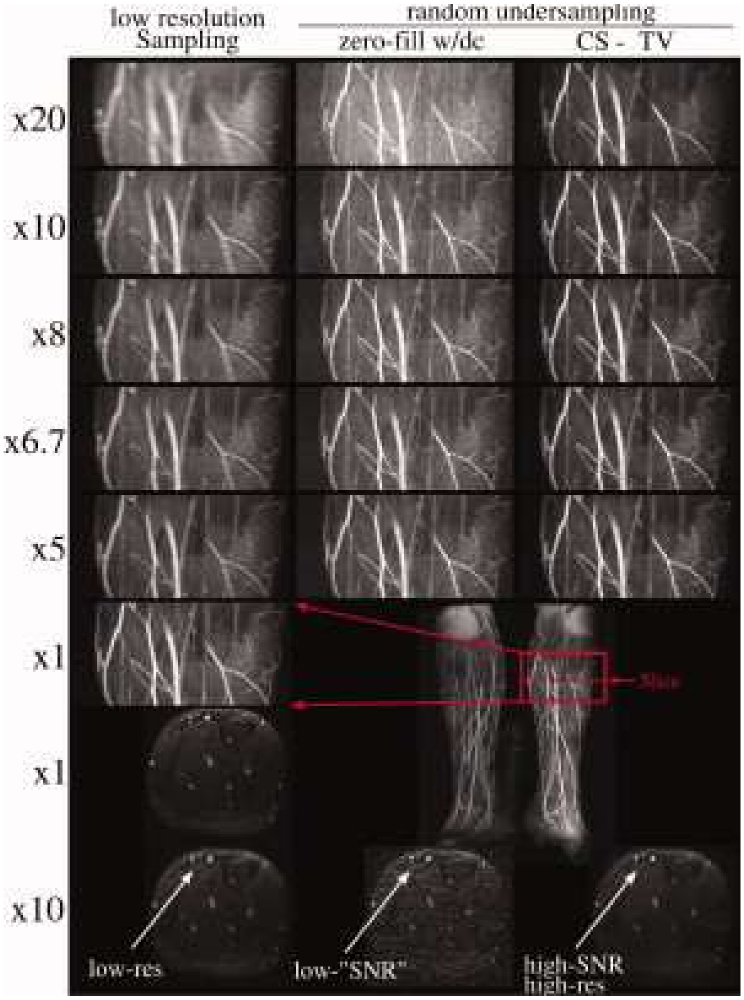

**Figure 2-14. Contrast-enhanced 3D angiography reconstuction results by different methods as a function of acceleration. [8] (Reproduced with permisson). Left column: accerelration by low-resolution. Mdidle column: accerelration by zero-filling with density compensation (zero-fill w/dc). Right: CS reconstruction with TV penalty from random under-sampled *k*-space.**

In reference [91], the *k*-space data were retrospectively randomly under-sampled by factors of 2, 4, 6, 8 and 10 and then reconstructed using distributed CS and coil-by-coil CS methods. Evaluated by two blinded readers, both CS methods resulted in image quality score similar to the fully-sampled reference images at under-sampling factors up to 6-fold for distributed CS and 4-fold for coil-by-coil CS reconstructions [91].

#### 2.3.2.4 Brain Imaging

Brain imaging, one of the most common clinical applications of MRI, is proved to be helpful in evaluating persistent headaches, dizziness and detecting certain chronic diseases of nervous system. Brain images have been demonstrated to present transform sparsity in wavelet domain [8]. One example of applying CS in brain imaging is shown as Figure 2-15. A brain image (see Figure 2-15b) was acquired by a full Nyquist-sampled data. Random phase-encode under-sampling trajectory is illustrated as Figure 2-15(a) with a random subset of 201 trajectories from 512 possible trajectories, an acceleration rate 2.55. Compared with zero-filling with density compensation reconstruction from the incoherent under-sampling (see Figure 2-15c), CS reconstruction (see Figure 2-15c) is

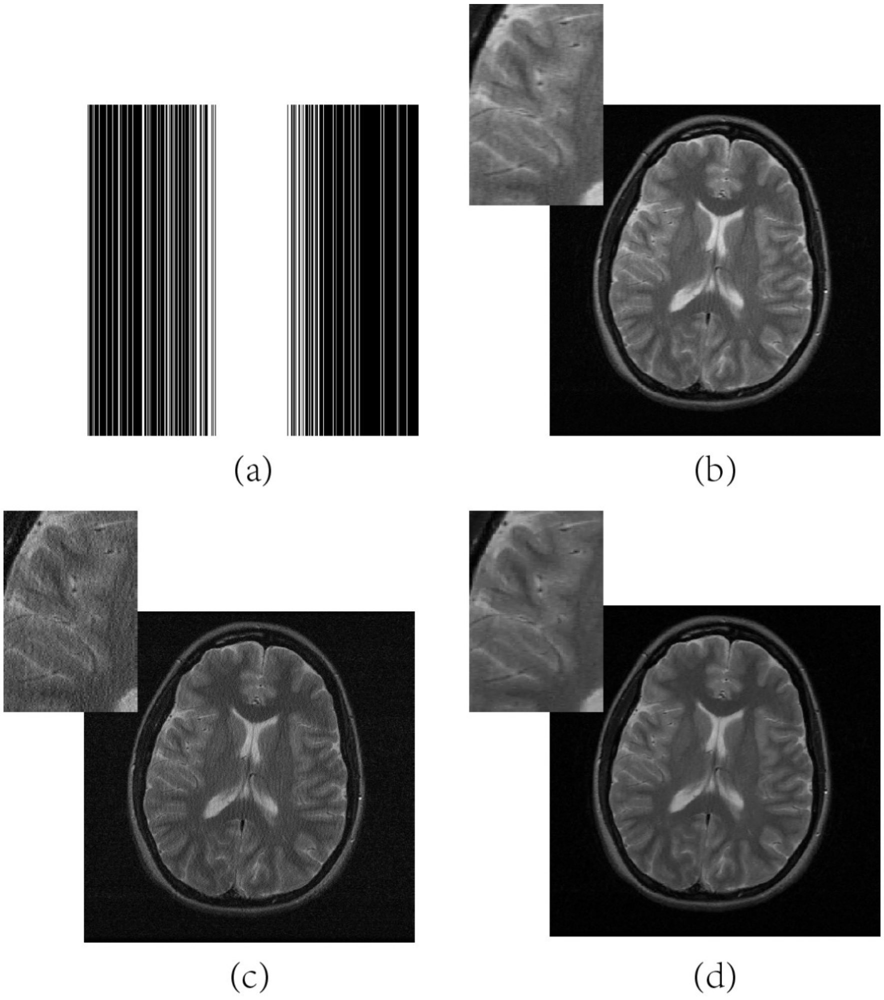

**Figure 2-15. The application of CS in a brain image when acceleration rate equals 2.55. (a) The random phase-encode under-sampling pattern (the white lines indicate the sampled part). (b) The fully sampled image. (c) The zero-filling with density compensation reconstruction from the under-sampled data. (d). The CS recosntruction from the under-sampled data.**

demonstrated to have a better suppression of aliasing artefacts and a comparable image quality to a fully sampled image. Reference [92] applied CS to recover brain images with 20% of fully sampled *k*-space data and illustrated the promising reconstructed results. Reference [93] developed a novel method based on CS to accelerate diffusion spectrum MRI. The experiments in brains proved that the application of CS can either reduce acquisition time without losing critical information or improve the resolution without using additional scan time.

#### *2.3.2.5 Functional MRI*

As a standard tool for function study of brain, functional MRI (fMRI) has a wide impact in both clinical diagnose and research. Using the positive blood oxygen level-dependent (BOLD) response signal as a measurement, functional MRI detects the activated nerve cells in the brain. The change of BOLD signal is very small compared with MR signal, which requires fast scan to avoid the noisy signal due to the subject motion or tissue pulsation [94]. Meanwhile, hemodynamic responses, another basic of functionality for fMRI, require the sufficient temporal resolution to be detected and measured. And the data collection of hemodynamic signals with high resolution is demanded to be finished during hundreds or a few milliseconds for various event related cognitive fMRI study. In all these cases, the acceleration of data acquisition in fMRI becomes necessary to eliminate the induced image distortion and resolve the resolution limitation [94].

The traditional acceleration technique PI is implemented to shorten the acquisition process. Compared with fully sampled images, the reconstructed images by PI present no significant difference visually [94]. However, the decreased SNR, residual aliasing artefacts introduced by under-sampling and the incomplete g-factor lead the detected activated area after statistical processing appears different from that of fully sampled ones [94]. Therefore, reference [95] investigated the CS approach in functional MRI. Using *k*-t FOCUSS as the CS reconstruction, the in-vivo rat experiments with gradient-recalled echo and EPI validated the performance of CS with reduction factors of 2 and 4. The work reported in reference [96] applied CS in functional MRI with non-EPI sequences to weaken the noises caused by local magnetic field inhomogeneity at high magnetic fields. The results confirmed the combination of CS and functional MRI with non-EPI was a good solution to get fine resolution images at high fields.

## 2.4 Current challenges in CS MRI

Despite the many successful applications of CS MRI, as mentioned previously, conventional CS MRI is still incapable of providing diagnostically accurate images in some specific cases. For example, residual incoherent artefacts may be present when reconstruction fails at a high acceleration rate; and pseudo random sampling may cause coherent aliasing artefacts. In the past few years, various methods have been proposed to improve the reconstruction quality of CS for MRI. These methods can be generally categorized into three groups. The first group focuses on methods to design random $k$-space sampling, which is essential for CS [12, 55, 97]. Irregular sampling patterns, such as variable density $k$-space sampling, are effective ways to improve incoherence between the sparse transform and sampling domains making aliasing interference less prominent. The second approach attempts to use a range of sparsity bases in spatial and temporal dimensions, such as discrete wavelet transform, curvelet transform [98] and singular value decomposition based transforms [99] to provide sufficient sparsity for faithful reconstruction using a subset of the largest transform coefficient. The third category concentrates on the nonlinear optimization methods for signal recovery [8, 10, 100]. This group of methods have been a research focus since CS was introduced. The algorithms, such as focal underdetermined system solution, iterative re-weighted least squares and conjugate gradients enforce both the image sparsity and data consistency between reconstruction and acquisition. Generally, a simple regularization scheme is applied to keep the balance between the two competing requirements [8, 100].

With the further application of CS MRI in rapid imaging, there are still some challenges that must be faced. One is pushing CS MRI to reconstruct the image with less sampled $k$-space data. In addition, further shortening the scanning time is required to meet the demands of dynamic imaging. As the reduction factor ($\mathrm{R} = \frac{D}{N}$, where N is the number of samples taken, D is the grid points defining the image) of current PI can be 3 or more, the reduction factor of CS MRI needs to break through this benchmark. Meanwhile, the residual reconstruction errors in the CS MRI reconstructed image at higher reduction factors limit the potential to use CS MRI in further applications. Figure 2-16 illustrates the comparison of reconstructed image by CS using the 2D random under-sampling pattern (the ideal under-sampling pattern) when R = 4 and 8. It is apparent that the residual artefacts in the reconstructed image at the higher reduction factor blurred the edges and details of the phantom image.

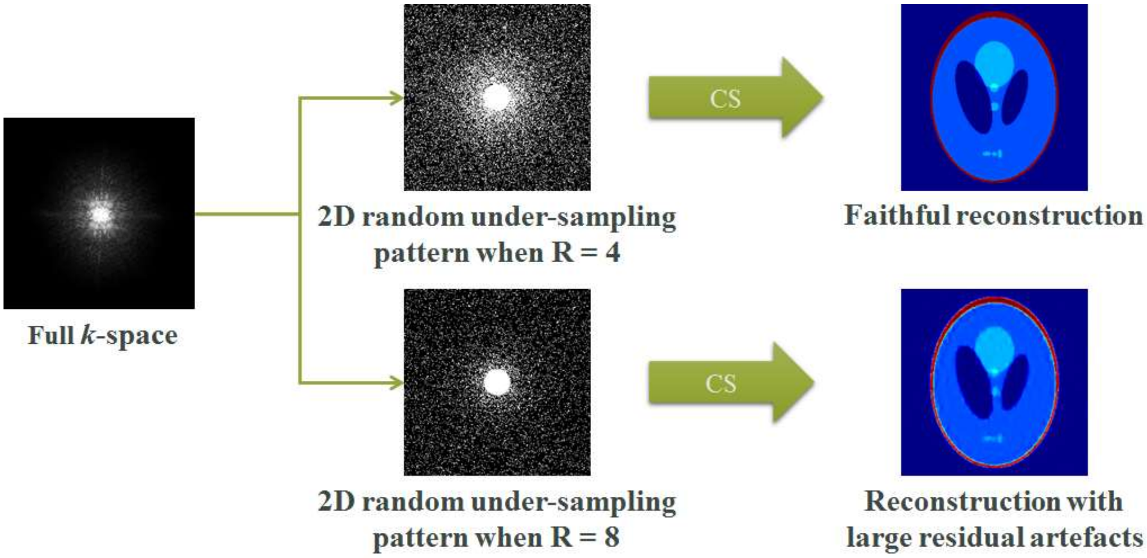

**Figure 2-16. The comparison of the image reconstruction by CS using the 2D random under-sampling pattern at different reduction factors.**

The feasibility is another challenge that limits the application of CS MRI in real clinical research. The main limitation is the creation of the under-sampling pattern that is a prerequisite for accurate reconstruction using the CS theory. As shown in Figure 2-17, using the real 2D random under-sampling pattern will cause the incoherent/noise-like artefacts in the under-sampled image and CS is ideal to use to faithfully reconstruct the image. But this is difficult to achieve on MRI machine in practice because the required rapid gradient switching is constrained by hardware. Furthermore, the resulting eddy current and relative artefacts can seriously degrade the quality of the reconstructed image [26].

Instead of real 2D random under-sampling, random phase-encode under-sampling can be implemented easily by adapting the current system based on a Cartesian trajectory, which is the most commonly used trajectory in MRI, and simply to reconstruct the images from the obtained *k*-space data. But the cost of compromise in 2D static MRI is that the randomness of random phase-encode under-sampling pattern is presented only in one direction (see Figure 2-17). This deteriorated randomness leads to large coherent aliasing artefacts along the frequency direction in the under-sampled image. These artefacts will weaken the effect of CS and degrade the reconstructed image quality. One example is illustrated in Figure 2-17. The images contaminated with aliasing artefacts cannot supply the accurate information required for clinical diagnosis.

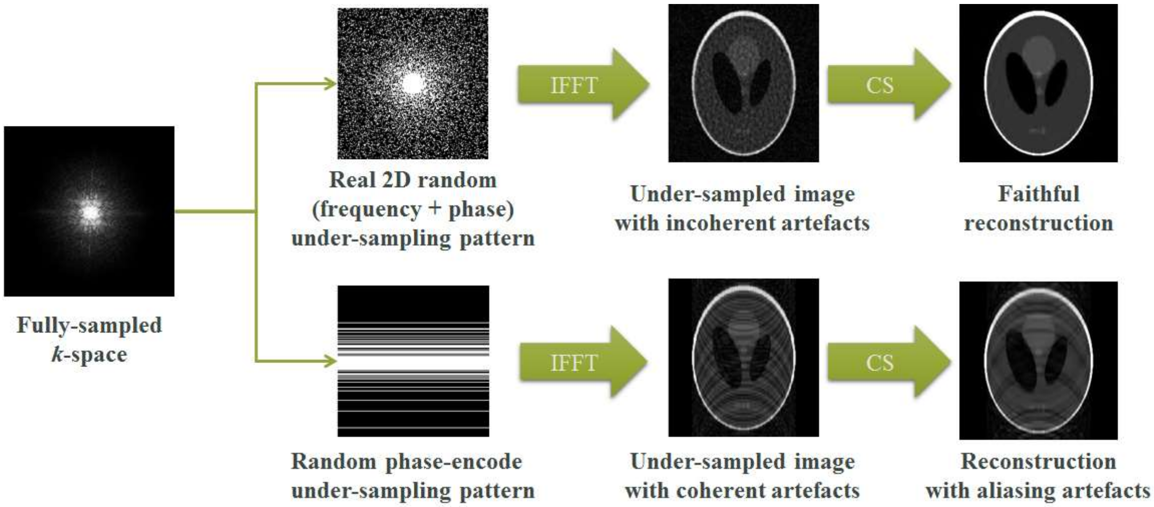

**Figure 2-17. The comparison of the effects of implementing the real 2D random under-sampling pattern and the phase-only random under-sampling pattern in CS.**

To solve the incoherence problem of the under-sampling pattern, a popular solution is to use a non-Cartesian approach such as radial trajectory. A traditional numerical metrics (PSF) approach [8] was used to measure the randomness of under-sampling pattern with different trajectories, which demonstrated the advantage of the radial trajectory for the incoherence property. In addition, radial trajectories sample more points in and around the centre of the *k*-space leading to a higher gain of SNR. The non-uniform distribution of sampling points with the radial trajectory is more fitted to the density distribution of the *k*-space data, since the majority of information is contained in the low-frequency components in the centre rather than the high-frequency components in the peripher [26]. Furthermore, each spoke of a radial trajectory samples the central *k*-space data, and the averaged central *k*-space data makes the radial trajectory less sensitive to motion effects. This makes a radial trajectory superior to a Cartesian trajectory in dynamic MRI such as cardiac MRI, because a breath hold is required in Cartesian scanning to avoid motion artefacts, whereas radial scanning can allow for a free breathing scan.

However, there are almost no non-Cartesian trajectories implemented in routine clinical use [17]. Even in practical clinical research, there are very few applications despite the extensive excellent work on radial trajectory based MRI over the last 20 years. Meanwhile, traditional FFT based on a Cartesian grid cannot be directly used to convert the *k*-space data collected using a radial trajectory into the images. The common method to reconstruct the *k*-space data collected using a radial trajectory is a regridding algorithm, which convolves each data point with a gridding kernel and re-samples the convolution interpolation on the Cartesian grid [101]. The traditional FFT can be implemented in these re-sampled data to get the final image. Although the regridding algorithm can overcome the burden of reconstructing *k*-space data based on a radial trajectory, it will cost a considerable time to compute the convolution and interpolation. The problem will deteriorate seriously when combined with CS, as the regridding and inverse regridding are necessary at every iteration of CS. Meanwhile, the highly under-sampled data used by CS leads to significant performance deterioration of regridding and the interpolation process of regridding also introduces errors that degrade the reconstructed image quality [101, 102].

The specific aim of this thesis is to resolve these challenges and issues by exploiting the properties of *k*-space data and developing novel reconstruction strategies to improve the reconstructed image quality of CS MRI. One important property is that the information content is not uniformly distributed in the *k*-space. The sparsity and the spatial frequency properties can be significantly different over various portions of the *k*-space. A new algorithm based on a multistage reconstruction strategy is developed to provide different treatments tailored to the specific portions of the *k*-space, thereby improving reconstruction quality. Another property of the *k*-space data is the parallelization of two-dimensional (2D) Fast Fourier Transform (FFT). 2D FFT is constituted of a series of parallel 1D FFT, which inspired the novel reconstruction strategy to separate a 2D image reconstruction into sequential parallel 1D signal reconstructions. Exploiting the 1D incoherence in these 1D signal reconstructions, the method is capable of eliminating the above mentioned large coherent aliasing artefacts introduced by the weak incoherence of the random phase-encode sampling pattern. In addition to the traditional Cartesian grid based *k*-space data, properties of a novel non-Cartesian grid are investigated. Compared with current non-Cartesian grids, the speed and accuracy of its relative transform between the *k*-space and image domain demonstrate the image quality of the reconstruction and promote its application in CS MRI for clinical diagnosis.

# 3. Compressed Sensing MRI via two-stage reconstruction

As mentioned in Chapter 2, CS has been applied MRI for the acceleration of data collection. However, existing CS techniques usually produce images with residual artefacts, particularly at high reduction factors.

In this chapter, a proposed method via two-stage reconstruction is introduced to reduce the residual artefacts. The method starts with segmenting the under-sampled k-space data into low-frequency and high-frequency domains. Then, in stage one, using dense measurements, the low-frequency region of *k*-space data was faithfully reconstructed. The fully reconstituted low-frequency k-space data from the first stage is then combined with the high-frequency k-space data to complete the second stage reconstruction of the whole of k-space. With this two-stage approach, each reconstruction inherently incorporates a lower data under-sampling rate than conventional approaches. Because the restricted isometric property was easier to satisfy, the reconstruction consequently produces lower residual errors at each step to improve the reconstructed image quality.

This chapter is largely based on the journal article “Compressed Sensing MRI via Two-stage Reconstruction,” accepted for publication by *IEEE Transactions on Biomedical Engineering*.

***Publication details***

Yang Yang, Feng Liu, Wenlong Xu and Stuart Crozier, "Compressed Sensing MRI via Two-stage Reconstruction," *IEEE Transactions on Biomedical Engineering*, vol. 62, pp. 110-118, 2015.

***Manuscript history***

| | |
|---|---|
| Received | 20 Oct 2013 |
| Interim Decision (major revision) | 21 Nov 2013 |
| Revision submission | 29 May 2014 |
| Accepted | 10 Jul 2014 |

| | |
|---|---|
| Available online | 23 Jul 2014 |

***Author contribution***

| Contributor | Statement of contribution |
|---|---|
| Yang Yang | Methodology development, code implementation, analysis and interpretation, manuscript preparation |
| Feng Liu | Analysis and interpretation, manuscript reviews |
| Wenlong Xu | Analysis and interpretation, manuscript reviews |
| Stuart Crozier | Analysis and interpretation, manuscript reviews |

## 3.1 Introduction

CS, a relatively new signal-processing theory, has been successfully applied to accelerate MRI [103]. MR images can be represented by a relatively small number of significant coefficients with nonzero values in an appropriate transform domain. CS takes advantage of the MR image sparsity and reconstructs the image from under-sampled data far less than that required by the Nyquist sampling theorem [9, 10, 104]. However, in stationary two-dimensional (2D) imaging, CS is still limited in providing diagnostically accurate images because it usually results in MR images with large residual artifacts [105].

Over the past few years, various methods have been proposed to improve the reconstruction quality of CS MRI. These methods can be generally categorized in three ways. First, designing irregular $k$-space sampling, such as variable density $k$-space sampling and random sampling, is an effective way. It makes the aliasing interference less visually prominent and incoherent in the sparse transform domain, which is an essential aspect for CS [55, 97, 105]. However, artefacts are difficult to distinguish from real signals at larger reduction factors (the ratio between the amount of subsampled data (D) and fully sampled data (N), i.e., $R = \frac{D}{N}$) [2]. This is because the final reconstructed image quality not only relies on the limited randomness of the $k$-space sampling, but it is also largely determined by another major factor, that is the total amount and property of the collected signal [105-108].

A second approach attempts to use a range of sparsity bases in spatial and temporal dimensions to provide sufficient sparsity for faithful reconstruction using a subset of the largest transform coefficients. For example, the discrete wavelet transform [8], curvelet transform [98], walsh transform [109] and singular value decomposition-based transforms [80, 99] are commonly used as sparsity transform. However, without sufficient *k*-space data, sparse coefficients transformed from the sampling signals cannot faithfully represent the original object and thus the quality of the reconstructed images is degraded.

The third category refers to optimization methods for nonlinear signal recovery [7, 8, 109] These have been a focus of research interest since CS was introduced. These algorithms, such as the focal underdetermined system solution, the iterative re-weighted least squares and the conjugate gradients, enforce both the image sparsity and data consistency between the reconstruction and the acquisition. In these methods, a simple regularization scheme is typically used to balance the sparsity of the whole image, relative to the required data consistency [8, 100]. However, one threshold may not satisfy both conditions simultaneously. Thus, it affects the final reconstruction accuracy, especially with high reduction factors [8, 113, 114]. Typically, the sparsity properties of the low-frequency and high-frequency *k*-space data can be significantly different [105, 114]. Frequency-specific regularization schemes could be used to resolve this issue.

In this chapter, we introduce a novel reconstruction scheme to relieve some of the shortcomings of previous methods. The two-part CS framework proposed in [110] reconstructs MR images with combined algorithms, while our method focuses on the study of the underlying signal properties of under-sampled *k*-space data. It consists of a two-stage reconstruction procedure to treat the low-frequency and high-frequency parts progressively. In this algorithm, an image outline will first be reconstructed based on the densely sampled *k*-space center, and then a full image will be recaptured using the recovered low frequency *k*-space data and the sparsely sampled high-frequency data. The feasibility and accuracy of the proposed method will first be theoretically analyzed and then validated through typical cardiac cine, brain, angiography, Lego phantom, cherry tomato, live mouse brain MRI imaging examples.

## 3.2 Methodology

### 3.2.1 Compressed Sensing MRI (CS MRI)

CS MRI can be briefly described as equation (2-16) in Section 2.3.1.3.

In this optimization problem, the first $l_0$ norm term promotes the sparsity of the reconstructed image *m* and the constraint $||\boldsymbol{P\varphi}(\boldsymbol{m}) - \boldsymbol{y}||_2 < \varepsilon$ enforces the data fidelity[8].

In CS MRI, the restricted isometry property (RIP) is usually used to analyse the performance and robustness of the CS algorithms. If the RIP condition holds [7], the reconstructed image $\boldsymbol{m}$ will be close to the original image.

Equation (2-16) is a well-known Non-deterministic Polynomial-time (NP) hard problem [7]. By replacing the $l_0$ norm with the $l_1$ norm to enforce the sparsity, it can be solved efficiently as a convex optimization, as follows:

$$\text{Minimize: } ||\boldsymbol{\Psi}(\boldsymbol{m})||_1, \text{ subject to } ||\boldsymbol{P\varphi}(\boldsymbol{m}) - \boldsymbol{y}||_2 < \varepsilon \quad (3\text{-}1)$$

### 3.2.2 Non-uniform signal sparsity

It is known that the *k*-space distribution concentrates in the region of origin while it has low levels at the borders (see Figure 3-1c), which shows the *k*-space data of a phantom). This reveals that the signal sparsity varies in different sections of the *k*-space. The non-uniform sparsity distribution can also be clearly seen in 2D Fourier transform (see Figure 3-1c).

Naturally indexed on dyadic cubes, the wavelet has a tree structure under inclusion [111]. The wavelet coefficients are monotonically non-increasing along the tree branches, outwards from the root. In the example shown in Figure 3-1, the tree structure (Figure 3-1a) illustrates that a wavelet coefficient is non-zero only if the wavelet coefficient in the coarser scale (the area in the red box in Figure 3-1(b), corresponding to the lower frequency part of image) is non-zero (except in very few situations) [105]. The leaves of the trees (the high frequency sub-bands) are typically the sparsest.

During the reconstruction process, the sparsity is constrained by the $l_1$ norm, which conventionally includes both the coarser scale and high frequency sub-bands. It is difficult to balance the different sparsities of these parts during optimization [98, 114]. Therefore, it is not an optimal method for sparsifying the images by global sparsity constraint.

In addition, the global sparsity constraint in conventional CS methods tends to select the signals with large magnitude in the *k*-space [114]. The *k*-space signal magnitudes corresponding to these two parts of the wavelet coefficients also show different features. As shown in Figure 3-1(c), the signal magnitudes in the central part of the *k*-space are much higher than the peripheral part. Thus, the global sparsity constraint leads the CS reconstruction to focus on the central region of *k*-space data. However, the $l_2$ norm operation in (3-1) is restricted by this in a conventional CS algorithm. The $l_2$ norm of the entire *k*-space is minimized to ensure the data fidelity. Although the signal magnitude of the *k*-space is typically smaller in the peripheral data, if it is not reconstructed faithfully, the error can accumulate over a population much larger than in the central region, and can strongly affect the effectiveness of the $l_2$ norm. To solve this problem, different weights are applied to balance $l_1$ and $l_2$ norms. However, this is a somewhat difficult implementation and the accuracy of reconstruction cannot be guaranteed [112].

Focusing on non-uniform sampling, [114] introduced a method with local sparsity constraints instead of a global one. Here, we will propose a new method based on *k*-space segmentation.

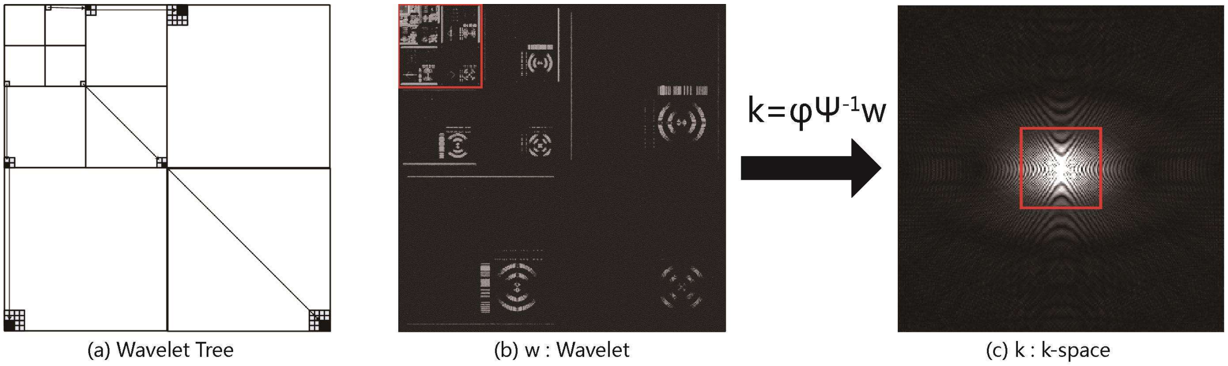

**Figure 3-1. The relationship between wavelet domain and k-space domain. (a) The tree structure of the Wavelet. Wavelet coefficients flow from the coarsest scale to the finest as the arrow shows. (b) the Wavelet coefficients of a phantom image. The non-zero coefficients focus on the coarser scale as in the red box. (c) the k-space data are transformed from the Wavelet coefficients by $k = \varphi\Psi^{-1} w$. The signal magnitudes of the central part in the red box (corresponding to the wavelet coefficients in the red box of (b)) are much higher than the peripheral part.**

### 3.2.3 *k*-space segmentation

As shown in Section 3.2.2, the energy of the $k$-space is concentrated close to the central region for the majority of MR images. The variable density-sampling pattern generally collects more data near the $k$-space centre (low-frequency parts) and less in the periphery of the $k$-space (high-frequency parts). One example of a random sampling pattern ($256 \times 256$ pixels) with the reduction factor $\mathrm{R} = \frac{256*256}{16395} = 3.99$ is illustrated in Figure 3-2(a). Its central region (the red square box with $64 \times 64$ pixels) has a reduction factor $\mathrm{R_{center}} = \frac{64*64}{2296} = 1.36$, which is much lower than the reduction factor of the whole $k$-space. Hence, the central region of the $k$-space can be reconstructed more faithfully with a low reduction factor.

In addition, the aforementioned wavelet coefficients in the coarser-scale part can be obtained from the faithfully recovered $k$-space data in the central region. Using the tree structure of the wavelet coefficients, the non-zero coefficients in the high frequency sub-band can be constrained based on the reconstructed coarser-scale data [105]. Because the sparsities of both the coarser-scale and high frequency sub-bands in the wavelet domain have been improved, the reconstruction accuracy of the whole image is meliorated.

In this section, we will describe how to segment the $k$-space in accordance with different sampling patterns. Suppose the size of the $k$-space is $\mathrm{N} \times \mathrm{N}$, a square box with size $\mathrm{n} \times \mathrm{n}$ is chosen in the $k$-space centre, as shown in the previous example in Figure 3-2(a). The sampling density of the selected part can be calculated by $\mathrm{D} = \mathrm{k}/\mathrm{n}^2$, where k is the number of the sampled points in the square box. With the increase of n as $\mathrm{n} = 2\mathrm{m}, \mathrm{m} \in [1, \mathrm{N}/2]$, the curve of D can be obtained. Figure 3-2(b) illustrates the sampling density curve of the random sampling pattern in Figure 3-2(a). It is obvious that the sampling density of the selected central part is much higher than that in the whole of the $k$-space.

Not only the sampling density, but also the $k$-space power of the selection is essential for the faithful reconstruction of the representative outline. If the central part is too small to obtain a high sampling density, it will contain too little $k$-space information. Thus, the image outline corresponding to the selected part cannot be representative of the whole image.

The determination of the size of the central part is important to the reconstruction of the image outline and also the final CS MRI solution. To find the proper size of a central $k$-space region, we define the *k*-space power ratio of the selected part by $\mathrm{P} = \frac{\mathrm{p(n)}}{\mathrm{p(N)}}, \mathrm{n} = 2\mathrm{m}, \mathrm{m} \in [1, \mathrm{N}/2]$, where the function p(n) means the sum of the power in the selected square area with size $\mathrm{n} \times \mathrm{n}$. Figure 3-2(d) shows the power ratio curve of under-sampled cardiac cine MRI data with the sampling pattern from Figure 3-2(a). As Figure 3-2(d) shows, it is clear that the power ratio P increases with the extension of the selected area.

A proper balance of the sampling density and power ratio is considered for the selection of the central region size. A higher sampling density ensures more accurate information in the central *k*-space region. A larger power ratio indicates that the *k*-space data in the selected region contains more information for the whole image. However, with the increase of n (size of the selected area), the sampling density and the power ratio show the opposite trends (see Figure 3-2b and Figure 3-2d). Therefore, a proper size for segmenting the k-space should be considered.

To balance the two contrary elements of the segmentation and to designate the segmentation, we define the average power ratio (AP) of the selected part as:

$$\mathrm{AP} = \mathrm{D} \times \mathrm{P} \tag{3-2}$$

The average power ratio can be thought of as a metric of the k-space power/information density of the selected region. One example is shown in Figure 3-2(e) by combining the sampling density (D) data from Figure 3-2(b) and the power ratio (P) data from Figure 3-2(d). The peak point of the AP curve in Figure 3-2(e) at $\mathrm{n} = 42$ is obviously the optimal choice of selected region size.

For the consideration of 2D wavelets, in the sparse base used here, the n value will be rounded to the power of 2. However, the peak point of AP $\mathrm{n} = 42$ does not satisfy the condition $\mathrm{n} = 2^{\mathrm{j}}, \mathrm{j} \in \mathbb{N}$, which is a fundamental property of the 2D-Wavelet transformation. Therefore, the proper choice n of the selected central part should satisfy $\mathrm{n} = 2^{\mathrm{j}}, \mathrm{j} \in \mathbb{N}$ and is closest to the peak point of the average power ratio curve. In the example shown in Figure 3-2(e), $\mathrm{n}_1 = 32$ and $\mathrm{n}_2 = 64$ are the two satisfied choices and $\mathrm{AP}(\mathrm{n}_1) < \mathrm{AP}(\mathrm{n}_2)$, $\mathrm{n}_2 = 64$ is the more suitable choice.

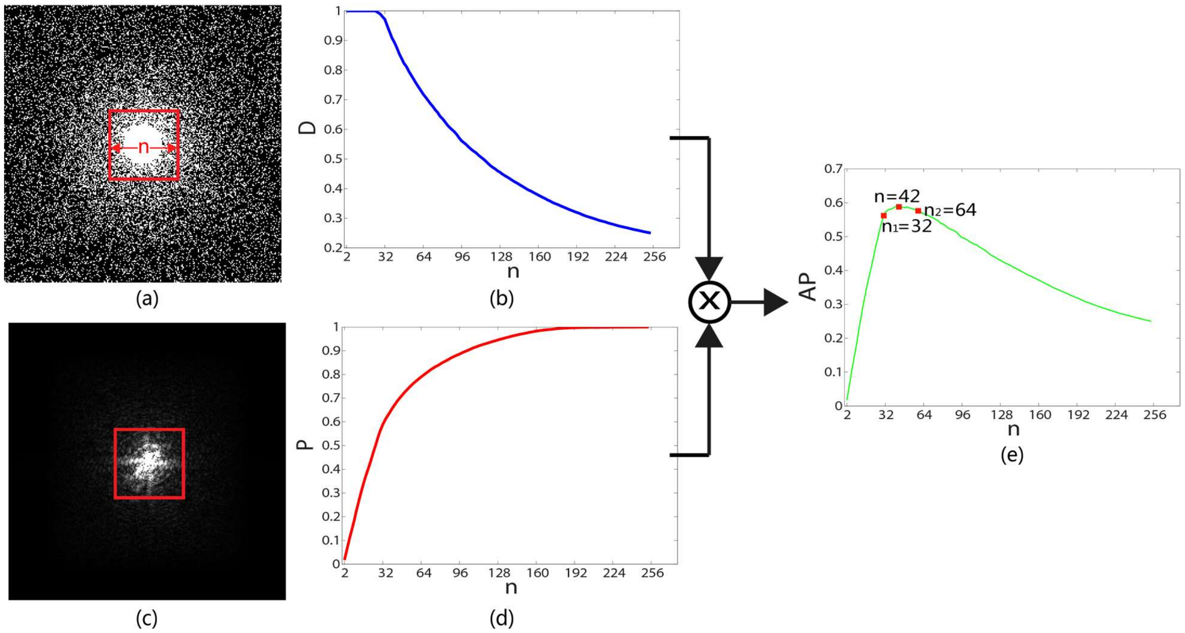

**Figure 3-2. *K*-space segmentation. (a) The selected central part (the area in the red square box with $\mathbf{n} \times \mathbf{n}$ pixels) in a random sampling pattern ($\mathbf{256 \times 256}$ pixels) when the reduction factor R = 4. (b) The sampling density of the selected central part ($\mathbf{n} \times \mathbf{n}$ pixels) in the sampling pattern as in (a) with $\mathbf{n = 2m, m \in [1, 128]}$. (c) The under-sampled k-space of a cardiac cine MR image with the sampling pattern as in (a). (d) The power ratio of the selected central part ($\mathbf{n} \times \mathbf{n}$ pixels) in (c) when $\mathbf{n = 2m, m \in [1, 128]}$. (e) The average power ratio in the selected central part of the under-sampled k-space data as in (c).**

### 3.2.4 Proposed two-stage reconstruction

We now detail the image reconstruction procedures involved in the two-stage process.

Step 1: Initialization. Suppose $\boldsymbol{m}$ is a MR image with $N \times N$ pixels, $\boldsymbol{p}$ is the under-sampling pattern, $\boldsymbol{y}$ consists of the under-sampled measurements with pattern $\boldsymbol{p}$, $\boldsymbol{\varphi}$ is the Fourier transform, $\boldsymbol{\Psi}$ is the 2D wavelet transform in advance and ε is the tolerance in (3-1).

Step 2: *k*-space segmentation. Using the strategy explained in Section C, II Theory, we segment the k-space into two parts.

Step 3: The reconstruction of the image outline (Level 1 reconstruction). According to the segmentation, the central part of the k-space measurements and sampling pattern can be obtained as $\boldsymbol{y}_c$ and $\boldsymbol{p}_c$. According to the Truncated-Fourier transform, the central part of the k-space data corresponds to the image outline [103]. The outline of the image $\boldsymbol{m}_{\mathrm{C}}$ can be reconstructed by the CS algorithm for solving the following problem:

$$\min_{\boldsymbol{m}_{\mathrm{C}}} \|\boldsymbol{\Psi}(\boldsymbol{m}_{\mathrm{C}})\|_1, \text{ subject to } \|\boldsymbol{p}_{\mathrm{C}}\boldsymbol{\varphi}(\boldsymbol{m}_{\mathrm{C}}) - \boldsymbol{y}_{\mathrm{C}}\|_2 < \varepsilon \tag{3–3}$$

Step 4: *k*-space combination. Transformed from the reconstructed image outline $m_c$ , the recovered *k*-space central part $\boldsymbol{k}_{\mathrm{C}} = \boldsymbol{\varphi}(\boldsymbol{m}_{\mathrm{C}})$ will replace the corresponding part $\boldsymbol{y}_{\mathrm{C}}$ in the whole *k*-space measurement y to obtain the new *k*-space data $\boldsymbol{k}_{\mathrm{R}}$.

Step 5: The reconstruction of the whole image (Level 2 reconstruction). Because the central region of the *k*-space has been reconstructed, for the Level 2 reconstruction, we use $\boldsymbol{p}_{\mathrm{R}} = \boldsymbol{p} + \boldsymbol{p}_{\mathrm{ac}}$ ($\boldsymbol{p}_{\mathrm{ac}}$ represents the central region to be all 1s) as the new sampling pattern. Using $m_{\mathrm{R}} = \boldsymbol{\varphi}^{-1}(\boldsymbol{k}_{\mathrm{R}})$ as the initial solution, the whole image $\mathrm{m}_{\mathrm{R}}$ can be reconstructed by the CS as follows:

$$min_{\boldsymbol{m}_{\mathrm{R}}} \|\boldsymbol{\Psi}(\boldsymbol{m}_{\mathrm{R}})\|_1, \; subject\ to\ \|\boldsymbol{p}_{\mathrm{R}}\boldsymbol{\varphi}(\boldsymbol{m}_{\mathrm{R}}) - \boldsymbol{y}\|_2 < \varepsilon \tag{3–4}$$

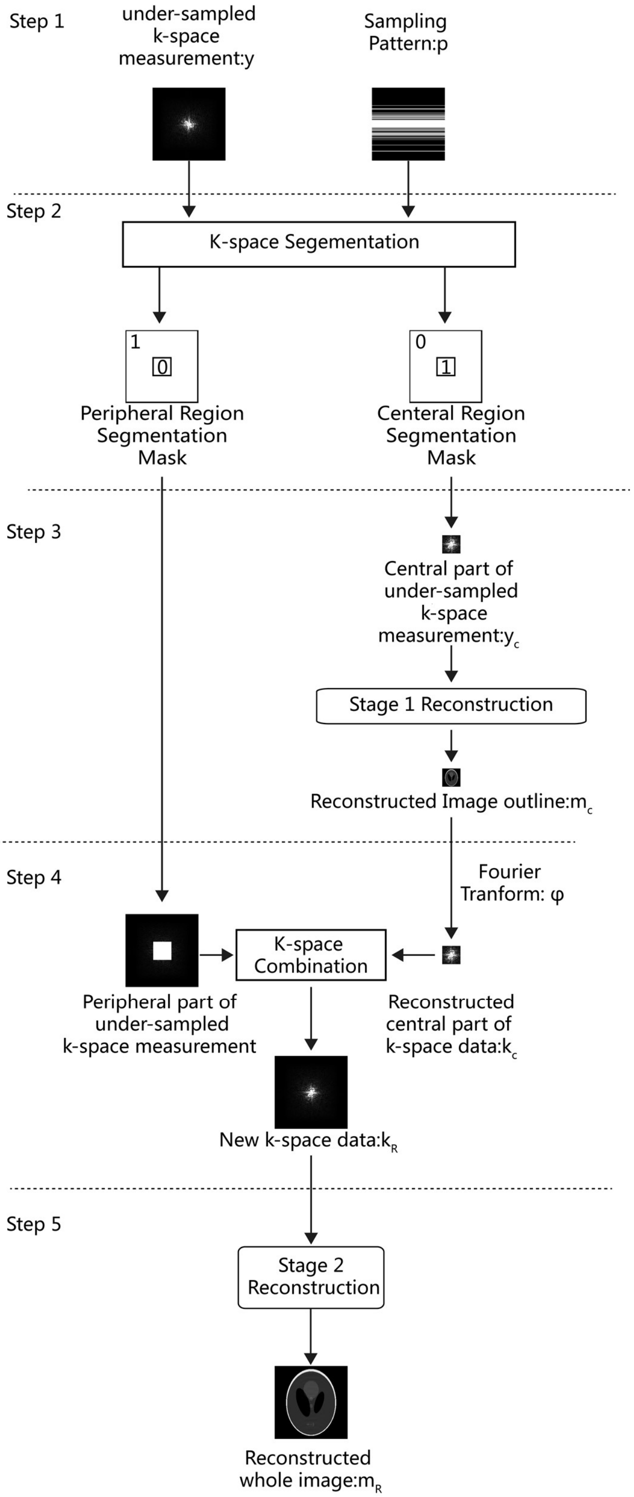

**Figure 3-3. The flowchart of the proposed two-stage reconstruction algorithm**

### 3.2.5 Experimental method

The performance of the proposed method was tested with a series of MR datasets: cardiac cine MR data, sagittal brain MR data, MR angiograms, a LEGO phantom, a cherry tomato and a live mouse brain.

The cardiac cine MR data was a frame of full *k*-space data acquired using a 1.5T Philips system, as a typical test case. The brain MR image, as a complex form with large contrast in the pixel domain was employed to test the algorithm performance for the cases with general MR images. The angiogram MR images were chosen to represent MR images already being sparse in the pixel domain. The *k*-space was fully acquired by a Siemens (Siemens Magnetom TIM Trio, Erlangen, Germany) 1.5T MRI system (CCAI, 2012). The LEGO phantom, cherry tomato and live mouse were collected by a 9.4T Bruker Biospin MRI preclinical scanner (Ettlingen, Germany) with a birdcage volume radiofrequency coil of 40 mm diameter. For all these cases, the image size was 256×256 pixels.

In MRI application, it is infeasible to implement 2D random under-sampling. So the data collection was implemented with 1D (only in phase direction) random under-sampling pattern on the fully sampled *k*-space data. It used a variable-density sampling scheme with a denser sampling at low frequency, which can be easily implemented by randomly changing the amplitudes of the phase-encoding [97]. For all the cases, the reduction factor R = 6 that means only 16.67% of the *k*-space data were sampled (see Figure 3-4).

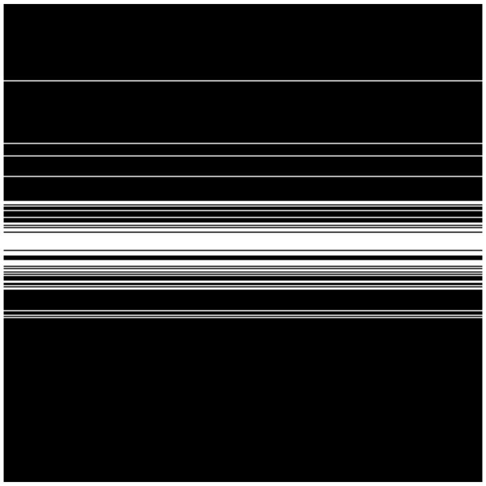

**Figure 3-4. 1D random under-sampling patterns used for Catesian *k*-space with R = 6.**

However, the incoherence of a 1D random pattern is weaker than a 2D random pattern, which can cause regular aliasing interference along the phase-encoded direction (data sampled randomly in this direction) in the reconstructed image. We will mainly evaluate the robustness and sensitivity of the proposed algorithm using this sampling scheme.

The algorithm in [8] is considered as the conventional CS method, which utilizes nonlinear conjugate gradients and a backtracking line-search for solving the optimization problem in (see Equation (3-1)). In the reconstruciton, the initial estimations are obtained from the under-sampled *k*-space data with zero-pading. The regularization parameters (Lagarangian multipliers for sparsity and TV terms) in both methods were tuned individually to achieve optimal reconstruction qualities. In the proposed method, the size of the selected central region was experimentally set at n = 64 to all the datasets. All the reconstructions were implemented with MATLAB (R2013b: The Mathworks, Natick, MA, USA) on a desktop computer with Intel Core i7–3770 eight-core Processor and 12GB of RAM.

The peak signal-to-noise ratio (PSNR) is used as the metric for the quality assessment. PSNR is most commonly used to be a quality measurement between the original and a lossy reconstructed image, which includes the mean square error of the reconstructed image in comparison with the reference image [115]. The PSNR was calculated as:

$$PSNR = 20log_{10}\left(\frac{MAX_I}{\sqrt{\frac{1}{mn}\sum_{i=1}^{m}\sum_{j=1}^{n}[I(i,j)-I_{rec}(i,j)]^2}}\right) \tag{3-5}$$

where $\boldsymbol{I}$ is the benchmark (fully sampled image), $MAX_I$ is the maximum possible pixel value of the image and $I_{rec}$ is the reconstructed image.

In addition, the intensity difference between the reconstructed images and the fully sampled images are also used to visually assess the reconstruction quality.

## 3.3 Results

### 3.3.1 Reconstruction performance with different reduction factors

The PSNR of the reconstructed images by a conventional CS method and the proposed method was recorded with respect to the reduction factor. The results of cardiac cine, brain and angiography MR datasets are shown as Figure 3-5, Figure 3-6 and Figure 3-7, respectively. The results of Lego phantom, cherry tomato and live mouse brain are shown as Figure 3-8, Figure 3-9 and Figure 3-10, respectively. The circles in the figure represent the conventional method, while the squares denote the two-stage method. As these figures illustrate, the improvements of the proposed method were very obvious in various cases and sampling patterns. They yielded an enhancement in quality of about 1.5 to 4 dB.

With the comparison of six different cases, the proposed method shows its capability in handling the cases with larger reduction factors. As we mentioned before, the 1D random pattern with Cartesian trajectories is more coherent compared with the 2D random pattern. Under the 1D random pattern, the PSNR curve of a conventional CS method decreases steeply with the increase of reduction factor R. The proposed method uses the higher sampling ratio in the selected region to suppress the aliasing artefacts in the reconstructed image outlines. For the tree structure of a 2D wavelet, the more accurately recovered image outline lead to a better sparsity representation of (the minimization of $l_1$ norm in Equation (3-1)) of the whole image, which can avoid the cartoon-like textures in the reconstruction introduced by over- minimization of $l_1$ norm in CS. Displayed in Figure 3-5 to Figure 3-10, the proposed method showed substantial improvement compared with the conventional ones.

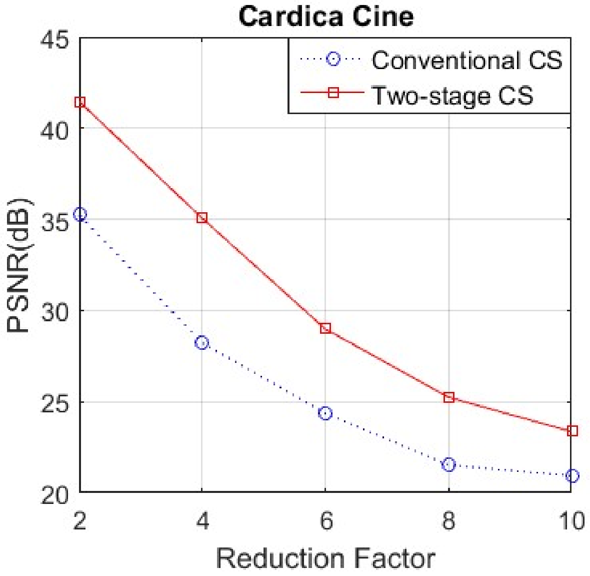

**Figure 3-5. Performance comparison between conventional CS and two-stage CS for cardiac cine MR data under different reduction factors with 1D random sampling pattern.**

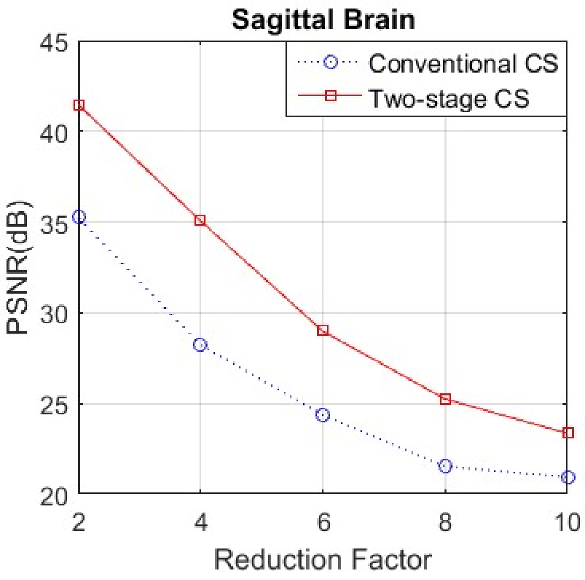

**Figure 3-6. Performance comparison between conventional CS and two-stage CS for sagittal brain MR data under different reduction factors with 1D random sampling pattern.**

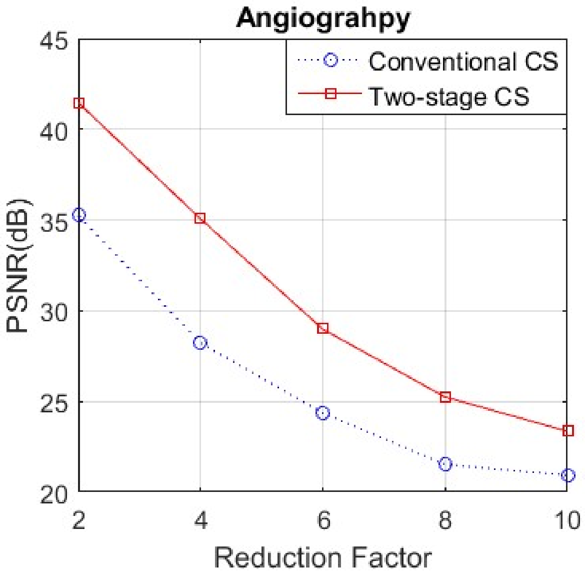

**Figure 3-7. Performance comparison between conventional CS and two-stage CS for angiography MR data under different reduction factors with 1D random sampling pattern.**

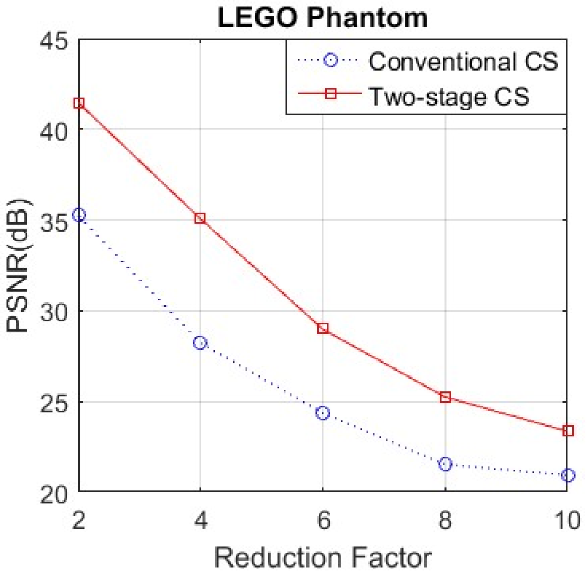

**Figure 3-8. Performance comparison between conventional CS and two-stage CS for Lego phantom MR data under different reduction factors with 1D random sampling pattern.**

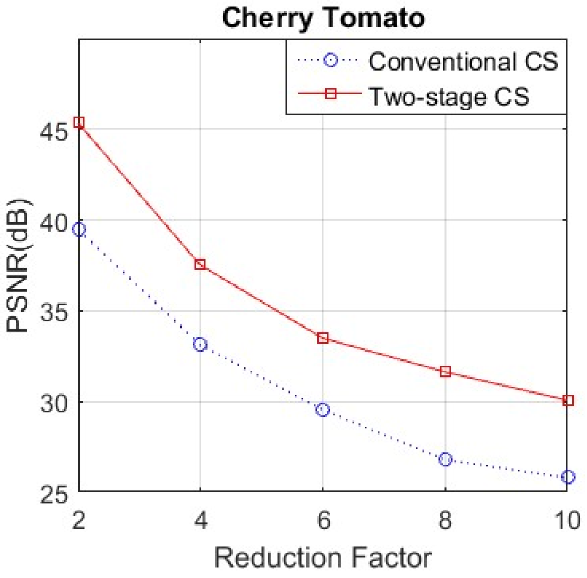

**Figure 3-9. Performance comparison between conventional CS and two-stage CS for cherry tomato MR data under different reduction factors with 1D random sampling pattern.**

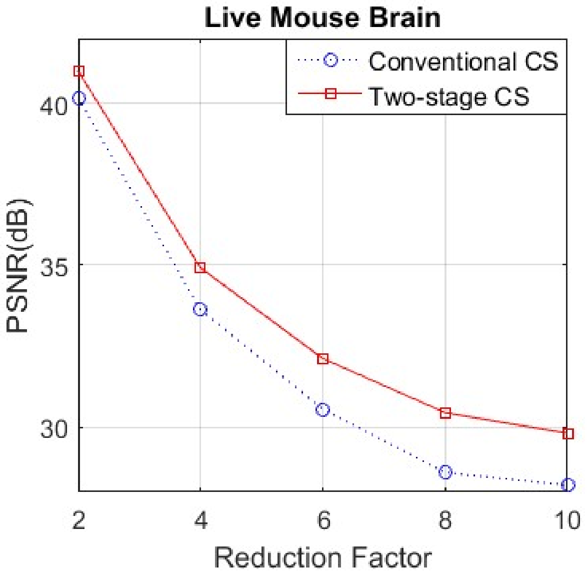

**Figure 3-10. Performance comparison between conventional CS and two-stage CS for live mouse brain MR data under different reduction factors with 1D random sampling pattern.**

### 3.3.2 Comparison of image reconstruction

The reconstruction results of the conventional method and the proposed method are presented. In Figure 3- 11 ~ Figure 3-16, six imaging cases (cardiac cine, brain, angiography, lego phantom, cherry tomato and live mouse brain) are compared, and in each case R = 6. For the situation at other reduction factors, Figure 3-17 illustrates the lego phantom in R = 4 as an example. The differences between the reconstructed images and the originals are also shown to facilitate comparison. For better visualization, the difference image in each case is normalized by its individual maximum.

The imaging studies indicate that the proposed method effectively reduces the aliasing artefacts in 1D random sampling pattern. In most cases, the proposed method offers higher fidelity in the reconstruction of image details than the conventional method. For the examples, note the improvements marked by red arrows in Figure 3- 11 ~ Figure 3-17.

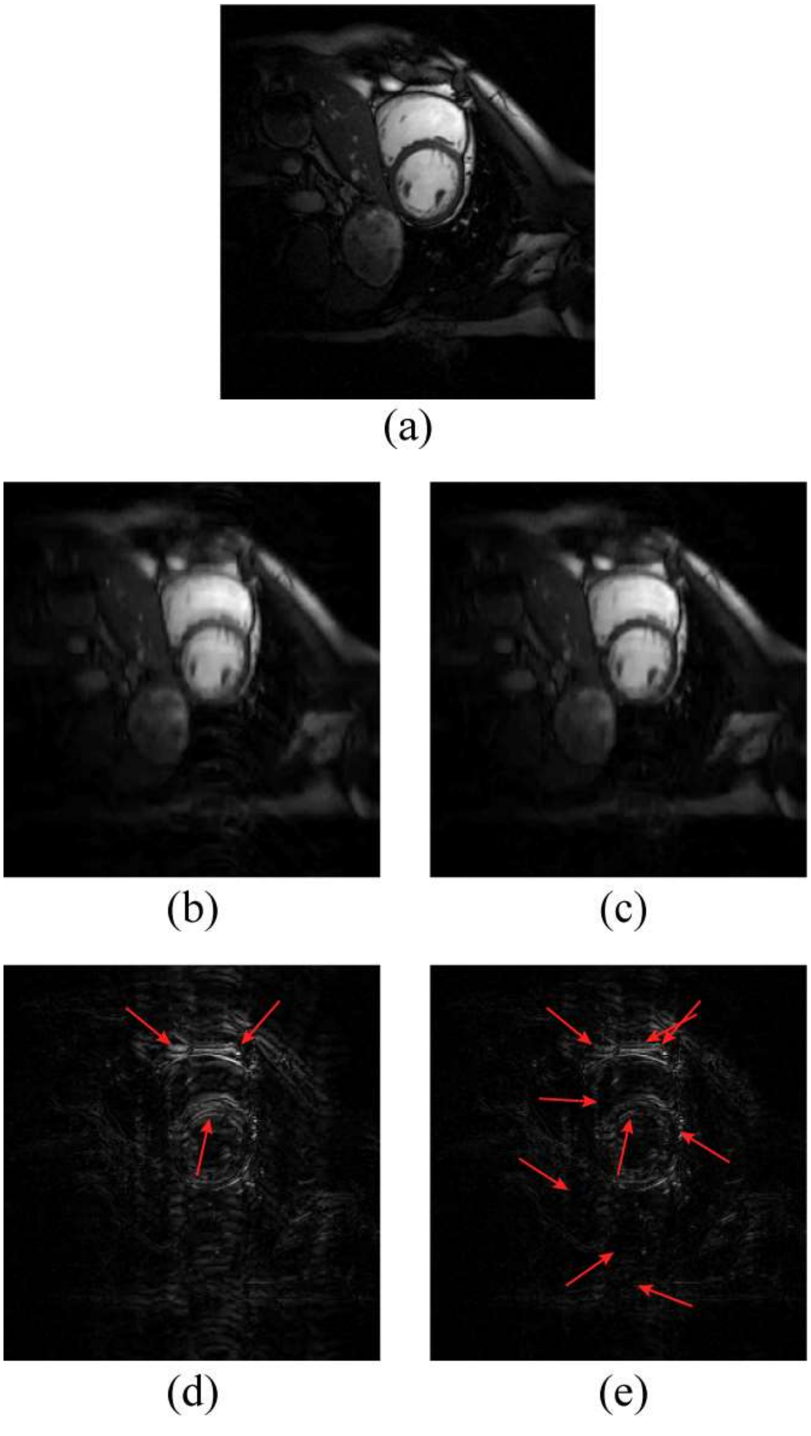
(a)
(b) (c)
(d) (e)

**Figure 3- 11. Reference image (a) and reconstructed images of cardiac cine MR data (b and c) and difference images (d and e) under 1D random sampling pattern at R = 6: (left) with conventional CS, (right) with the proposed two-stage CS.**

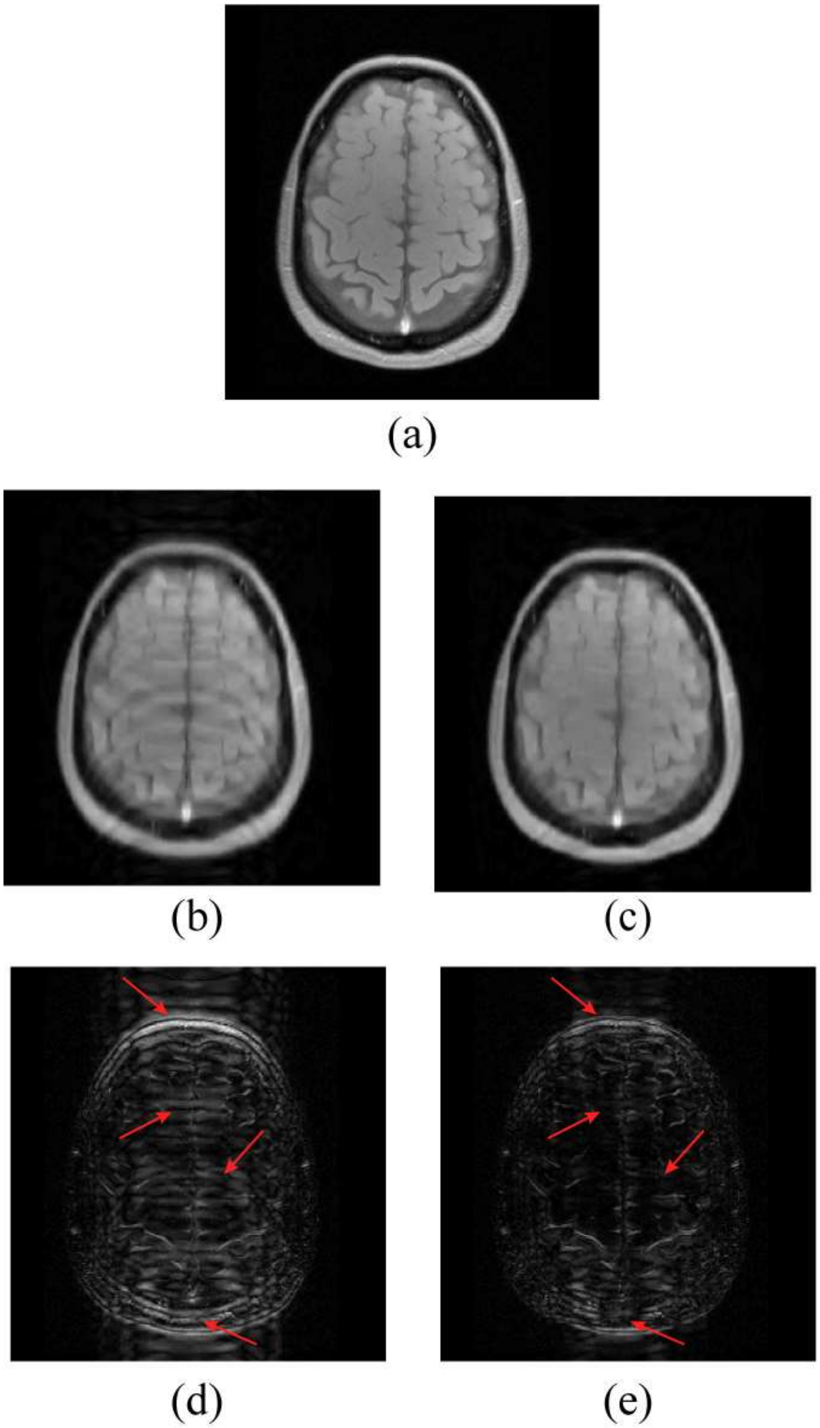

(a)

(b) (c)

(d) (e)

**Figure 3-12. Reference image (a) and reconstructed images of brain MR data (b and c) and difference images (d and e) under 1D random sampling pattern at R = 6: (left) with conventional CS, (right) with the proposed two-stage CS.**

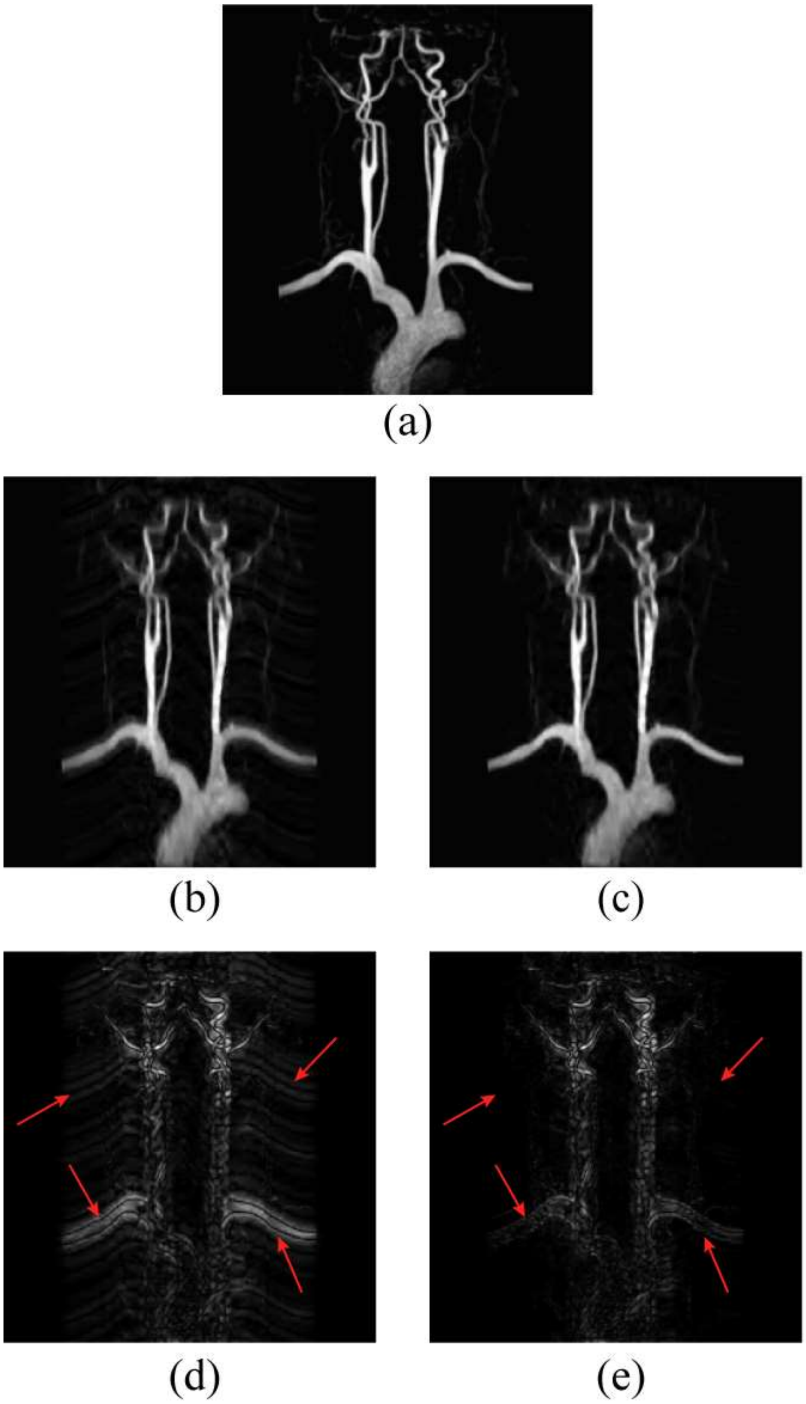

**Figure 3-13. Reference image (a) and reconstructed images of angiography MR data (b and c) and difference images (d and e) under 1D random sampling pattern at R = 6: (left) with conventional CS, (right) with the proposed two-stage CS.**

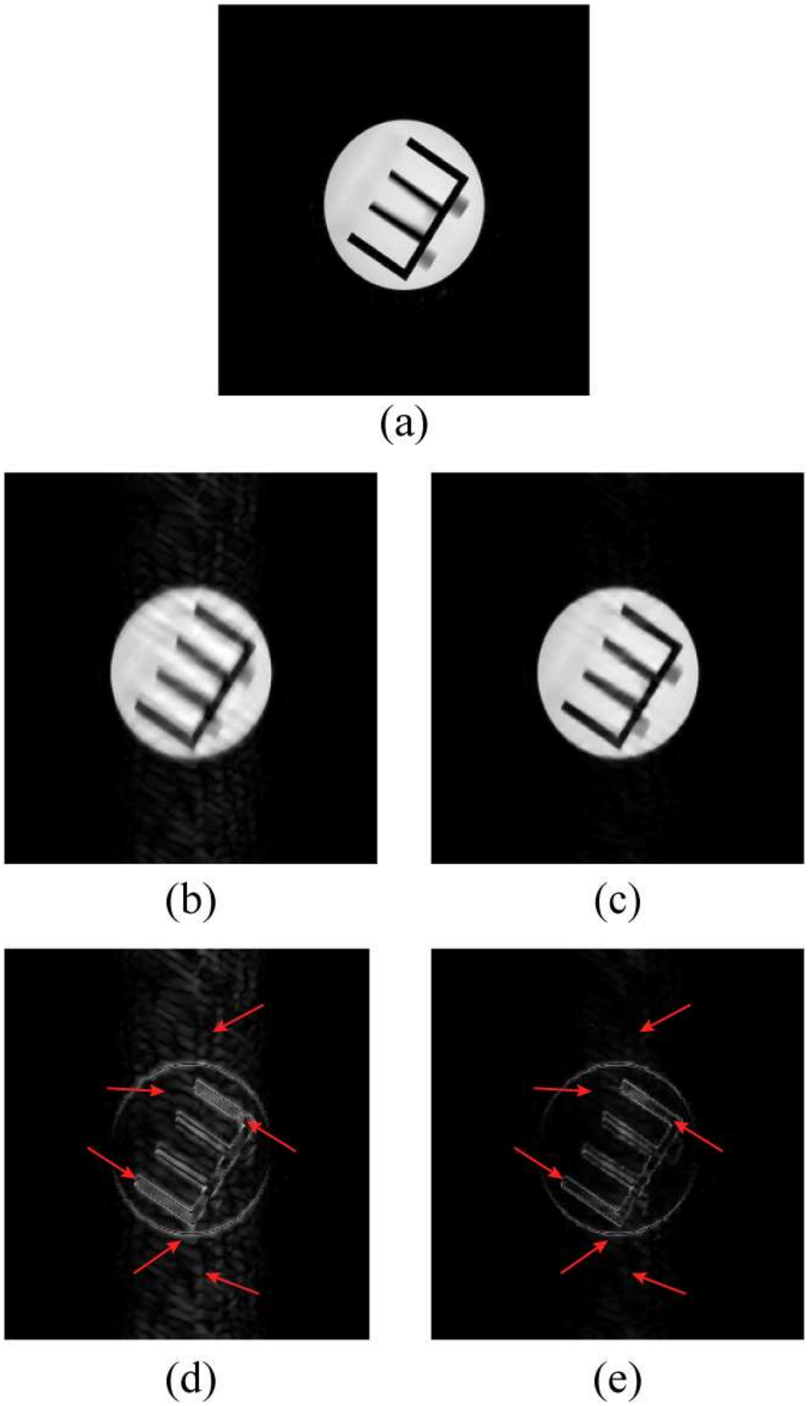

(a)

(b) (c)

(d) (e)

**Figure 3-14. Reference image (a) and reconstructed images of Lego phantom MR data (b and c) and difference images (d and e) under 1D random sampling pattern at R = 6: (left) with conventional CS, (right) with the proposed two-stage CS.**

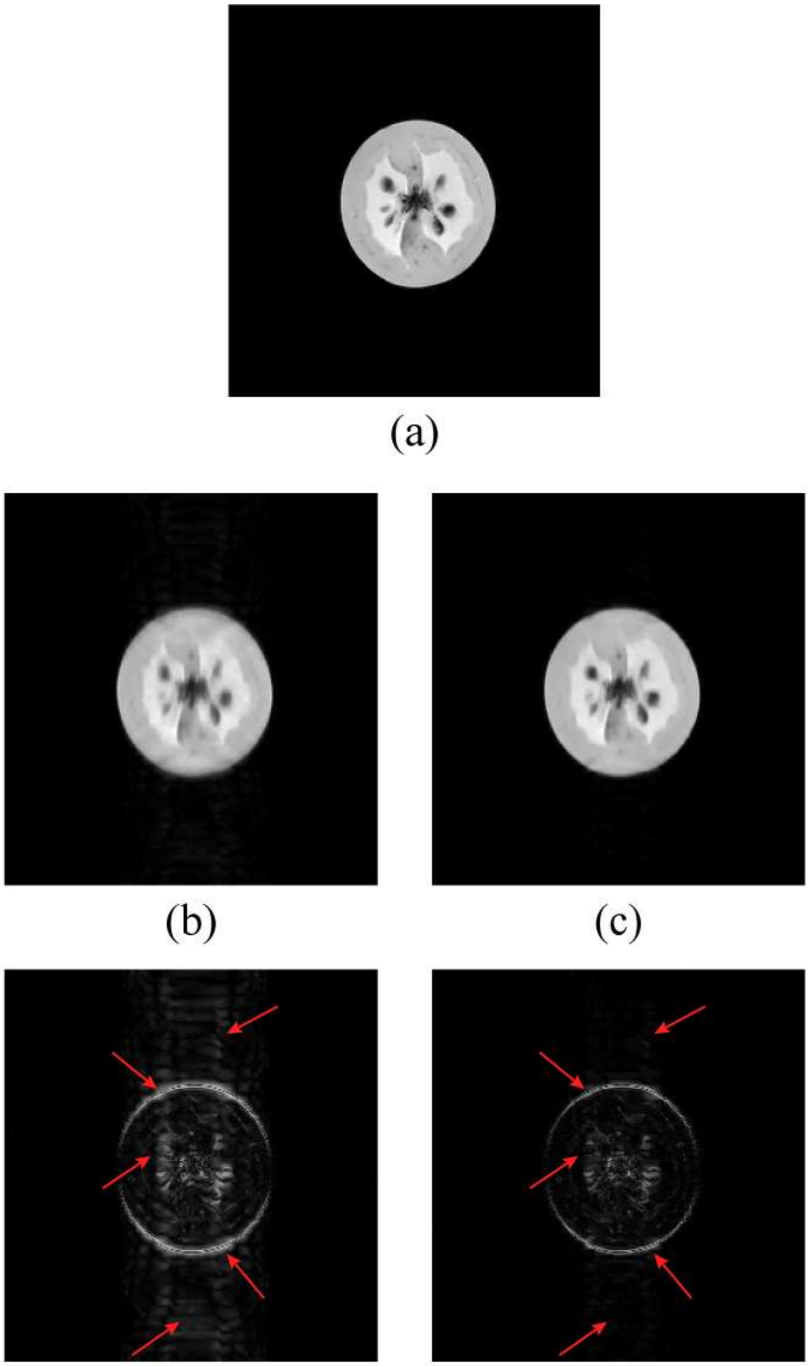

(a)

(b) (c)

(d) (e)

**Figure 3-15. Reference image (a) and reconstructed econstructed images of cherry tomato MR data (b and c) and difference images (d and e) under 1D random sampling pattern at R = 6: (left) with conventional CS, (right) with the proposed two-stage CS.**

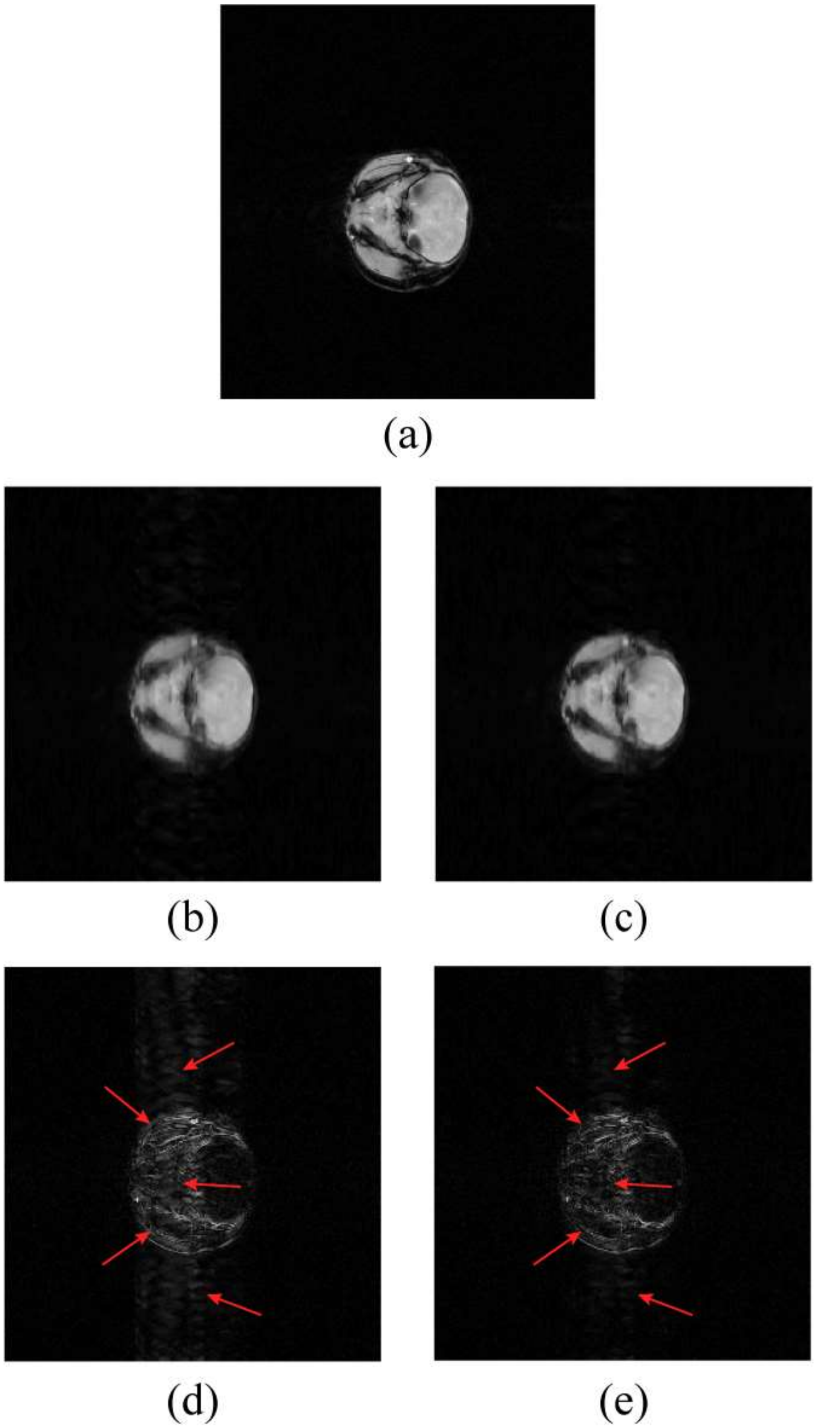

**Figure 3-16. Reference image (a) and reconstructed econstructed images of live mouse brain MR data (b and c) and difference images (d and e) under 1D random sampling pattern at R = 6: (left) with conventional CS, (right) with the proposed two-stage CS.**

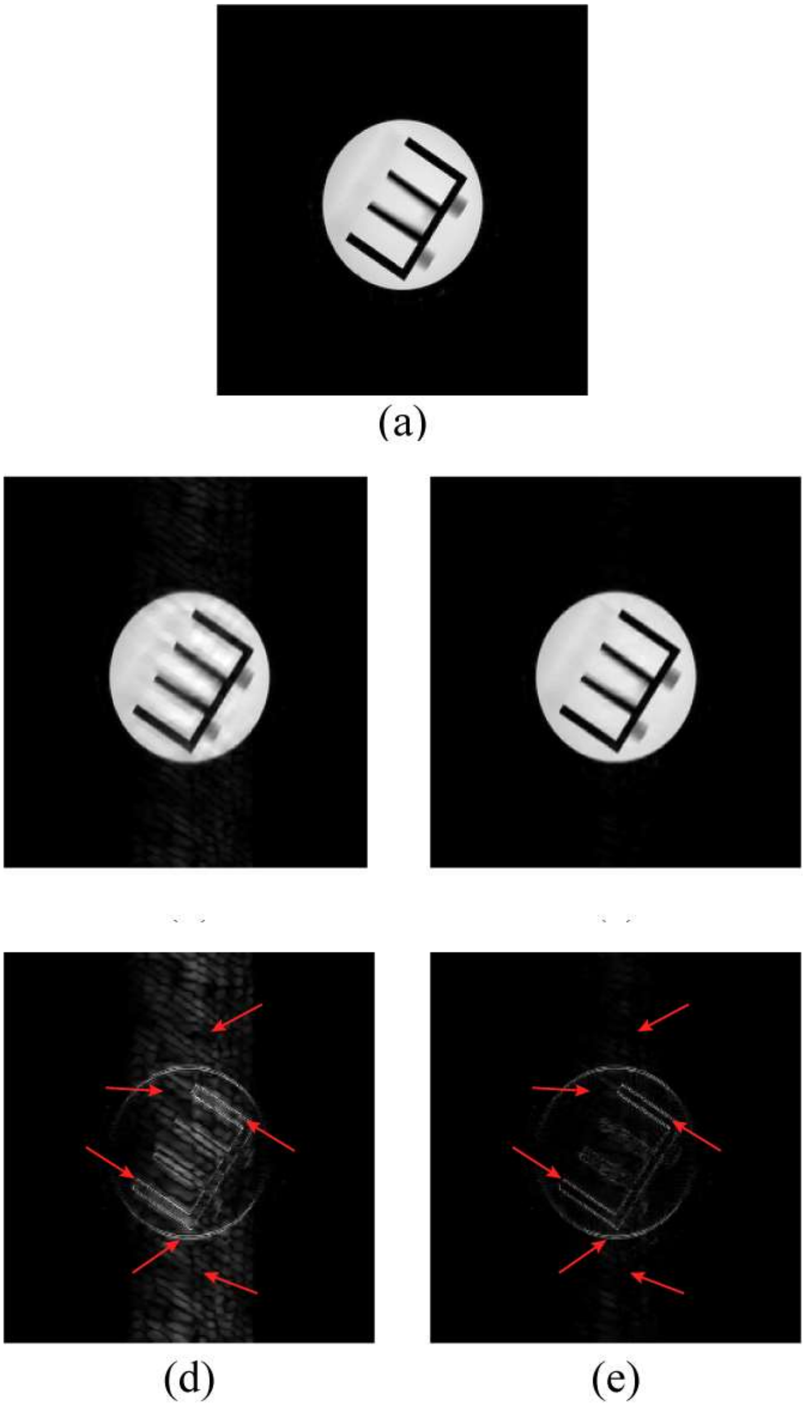

**Figure 3-17. Reference image (a) and reconstructed images of Lego phantom MR data (b and c) and difference images (d and e) under 1D random sampling pattern at R = 4: (left) with conventional CS, (right) with the proposed two-stage CS.**

## 3.4 Discussion

Compared with the conventional method, the reconstruction of a two-stage method localizes to different parts of the *k*-space to exploit the redundancy of the sampled data. To balance the reduction factor and reconstruction quality, the two-stage CS method takes advantage of the inhomogeneous distribution of the *k*-space power and the variable-density of the sampling pattern. The higher sampling ratio of the selected central *k*-space data leads to a more faithful reconstruction. The reconstructed image outlines in stage one can conduct a better initial solution for the whole *k*-space reconstruction of stage two. The corresponding wavelet coefficients in the coarser scale can approach the sparsity control of the whole image. The solution also avoids most incoherent artefacts caused by the estimation errors at the low-frequencies. For the 1D random sampling pattern, the reconstruction of the conventional CS schemes usually has more aliasing artefacts, because the sampling pattern is only random in one direction. Using the proposed method, the low-frequency *k*-space information was recovered with a lower reduction factor first that could reduce the aliasing effects. With a more faithful image outline (coarser scale of wavelet coefficient), the whole image reconstruction was more accurate and with less aliasing artefacts by the sparsity control of wavelet tree structure.

As mentioned, the sparsity of the wavelet coefficients in the coarser scale and the high frequency sub-band are different. It is useful to adjust the weights of $l_1$ and $l_2$ in the two-stage optimization process of the CS algorithm. From previous case studies, the results manifested the effects of weighting adjustment in different *k*-space parts. We also note that, the 2D wavelet sparsity in the two-stage reconstruction can be replaced by other proper sparsifying transformations [80, 109].

In the implementation of the proposed two-stage reconstruction, the algorithm convergence of each iteration is better owing to smaller problem size (in stage one) and better initial condition (in stage two). Therefore, although the total iteration times of two stages are similar to those of the conventional method, the two-stage CS has less total computational time.

## 3.5 Conclusion

To reduce the large reconstruction artefacts that occur when using existing CS schemes with high reduction factors, we have proposed a two-stage CS method that recovers the central and peripheral *k*-space data in a sequential manner. From the relatively dense sampled inner k-space part, an image outline is first reconstructed. Using image outline from stage one and the sampled peripheral *k*-space data, a full image recovery is then implemented. This stepped reconstruction naturally solves a number of technical difficulties in conventional CS methods, including the processing of a large magnitude contrast between the low-frequency and high-frequency *k*-space data. The new method has been applied to cardiac cine, brain and angiography MRI datasets and compared with non-staged CS schemes; we have demonstrated that the new method improves the reconstruction accuracy and reduces the reconstruction time. Because the presence of aliasing artefacts also limits the application of the CS in dynamic MRI, in our future work, we plan to extend the developed CS algorithm to dynamic MRI studies.

# 4. Aliasing Artefact Suppression in Compressed Sensing MRI for Random Phase-encode Under-sampling

As introduced in Chapter 2, random phase-encode under-sampling of Cartesian *k*-space trajectories is widely implemented in CS MRI instead of the ideal pure 2D random under-sampling pattern. However, its 1D randomness inherently introduces large coherent aliasing artefacts along the under-sampled direction in the reconstruction, and thus degrades the image quality.

This chapter approached a novel reconstruction scheme to reduce the 1D under-sampling induced aliasing artefacts. The proposed reconstruction progress was separated into two steps in our new algorithm. In step one, the method transferred the original 2D image reconstruction into a parallel 1D signal reconstruction procedure, which takes advantage of the superior incoherence property in the phase direction. In step two, using the new *k*-space data obtained from the 1D reconstructions, the method implements a follow-up 2D CS reconstruction to produce a better solution, which exploits the inherent correlations between the adjacent lines of 1D reconstructed signals.

A large part of this chapter is based on the journal article "Aliasing Artefact Suppression in Compressed Sensing MRI for Random Phase-encode Under-sampling," accepted for publication by *IEEE Transactions on Biomedical Engineering*.

***Publication details***

Yang Yang, Feng Liu, Zhaoyang Jin and Stuart Crozier, "Aliasing Artefact Suppression in Compressed Sensing MRI for Random Phase-encode Undersampling," *IEEE Transactions on Biomedical Engineering*, vol. 62, pp. 2215-2223, 2015.

***Manuscript history***

| | |
|---|---|
| Received | 17 Dec 2014 |
| Interim Decision (major revision) | 13 Jan 2014 |
| Revision submission | 27 Feb 2014 |

| | |
|---|---|
| Accepted | 26 Mar 2014 |

***Author contribution***

| Contributor | Statement of contribution |
|---|---|
| Yang Yang | Methodology development, code implementation, analysis and interpretation, manuscript preparation |
| Feng Liu | Methodology development, analysis and interpretation, manuscript reviews |
| Zhaoyang Jin | Analysis and interpretation, manuscript reviews |
| Stuart Crozier | Analysis and interpretation, manuscript reviews |

## 4.1 Introduction

In MRI, the raw image data is acquired in the *k*-space (frequency domain), which is transformed by Inverse Fourier Transform to obtain the diagnostic image. Limited by physical and physiological constraints, the sequential acquisition of the full *k*-space is inherently slow. This intrinsically lengthy scan process causes additional discomfort to the patient, invites involuntary motion artefacts and reduces the temporal resolution critical for diagnosis.

CS, as a novel mathematical framework, has gained considerable attention for its application in MRI because it can significantly reduce acquisition time [7, 10, 11, 55]. CS reconstructs images using far fewer samples than required when using conventional methods.

In CS MRI, the obtained samples are incomplete, violating the classical Shannon Nyquist sampling criterion, thereby leading to distortions in the acquired MR images. By taking advantage of the sparse representations of MR images in certain mathematical transforms, CS exploits the underlying data structure to overcome the distortions and faithfully reconstruct the images.

A successful application of CS in MRI has three requirements: transform sparsity, nonlinear reconstruction and incoherent under-sampling patterns [8, 9]. The design of under-sampling patterns is critical to the performance of CS MRI because it determines the quality of reconstructed images and the scanning time.

The under-sampling scheme should make the collected subset of the *k*-space data be efficiently representative of the whole image and be incoherent with respect to the sparsifying transform. In stationary CS MRI, the 2D random under-sampling scheme is the ideal choice for its perfect incoherence performance [8-10]. Recently, 2D random under-sampling trajectories were specially designed for CS MRI [105, 116-118]. Meanwhile, the 2D random under-sampling pattern is physically impractical because of MRI hardware constraints. In non-Cartesian trajectories (e.g. spiral, radial), their inherent presence of incoherent aliasing artefacts for under-sampling makes them suitable for the performance of CS [119]; however, additional gridding and regridding processes are time-consuming and may degrade the CS reconstruction effort. In practice, random phase-encode under-sampling of Cartesian *k*-space trajectories is implemented with minor modification of the existing pulse sequences. Owing to its effectiveness in compressed data collection, as well as its robustness against system imperfections, it has been widely used for CS MRI research [8, 9, 26, 120].

The random phase-encode under-sampling can degrade the quality of reconstructed images by CS. Its 1D randomness makes the incoherence significantly worse than 2D random under-sampling patterns. To address this issue, various approaches have been proposed which mainly focus on the *k*-space under-sampling pattern design. For example, reference [97] proposes a pseudo 2D random under-sampling scheme to under-sample the *k*-space along one direction first and then the other. Reference [121] introduces an under-sampling pattern that mainly collects high-energy points. Reference [117] designs under-sampling patterns based on certain reference images and samples the *k*-space data with statistically high energy. Reference [122] processes the low-frequency and high frequency *k*-space data separately through a two-stage reconstruction procedure. Reference [116] shows the possibility of automatically constructing an adaptive random under-sampling pattern by using measured *k*-space data as a reference.

In this chapter, we propose a novel reconstruction scheme that will take advantage of the 1D incoherence of random phase-encode under-sampling patterns. In this new method, we first decouple the under-sampled 2D *k*-space data to a series of 1D signals. Then using the incoherence property of these randomly collected 1D signals, a parallel 1D CS reconstruction is implemented. With the outputs of 1D reconstruction, we implement a follow-up 2D reconstruction to take advantage of the correlation in the image domain between the contiguous 1D signals. To demonstrate the performance of the proposed method, we used various typical MR images, cardiac cine, brain, foot and angiography as test datasets, at reduction factors up to 10. Using PSNR and structural similarity (SSIM) index as numerical metrics for image quality of reconstruction, we have compared our new solution with conventional one.

## 4.2 Methodology

### 4.2.1 CS MRI

As mentioned in Section 2.3.1.3, the standard CS MRI operation can be mathematically described as follows. Suppose the object MR image as $\boldsymbol{x} \in \boldsymbol{C}^{\mathrm{M \times N}}$**,** which has a sparse representation in a basis $\boldsymbol{\Psi}$. The CS MRI reconstruction model can thus be described as the following constrained optimization problem [8, 9]:

$$\text{Min} \quad \|\boldsymbol{\Psi}(\boldsymbol{x})\|_1 \quad \text{s.t.} \quad \|\emptyset_{\boldsymbol{P}}(\boldsymbol{x}) - \boldsymbol{y}\|_2 < \varepsilon \tag{4-1}$$

where $\boldsymbol{\Psi}$ denotes the sparse transform, $\emptyset_{\boldsymbol{P}}$ is the partial Discrete Fourier transform (DFT) with an under-sampling pattern $\boldsymbol{P}$, $\boldsymbol{y} = \emptyset_{\boldsymbol{P}}(\boldsymbol{I})$ consists of the *k*-space measurements, ε is related to the expected noise level of the measurements [8, 9].

### 4.2.2 Incoherence problem in the random phase-encode under-sampling

The incoherence of the under-sampling pattern is an essential ingredient for the sparse signal reconstruction in CS. The theoretical mathematical condition for incoherence, Restricted Isometry Property (RIP), is hard to verify in practical applications. In general, the point spread function (PSF) can be used to evaluate the incoherence property of the under-sampling pattern [8]. The PSF is defined as $\mathrm{PSF}(i,j) = \boldsymbol{e}_j^{*}\boldsymbol{F}_u^{*}\boldsymbol{F}_u\boldsymbol{e}_i$, where $\boldsymbol{F}_u$ is the under-sampled Fourier operator and $\boldsymbol{e}_i$ is the ith vector of the canonical basis, the operator * stands for the conjugate transposing. Under-sampling causes pixels to interfere and the PSF to produce nonzero values. The convolution of the under-sampling pattern's PSF and the fully sampled image is the under-sampled image. Thus, the standard deviation of the PSF side lobes was used to quantify the power of the resulting incoherent artefacts (pseudo-noise) and incoherence was computed using the main lobe to pseudo-noise ratio of the PSF [119].

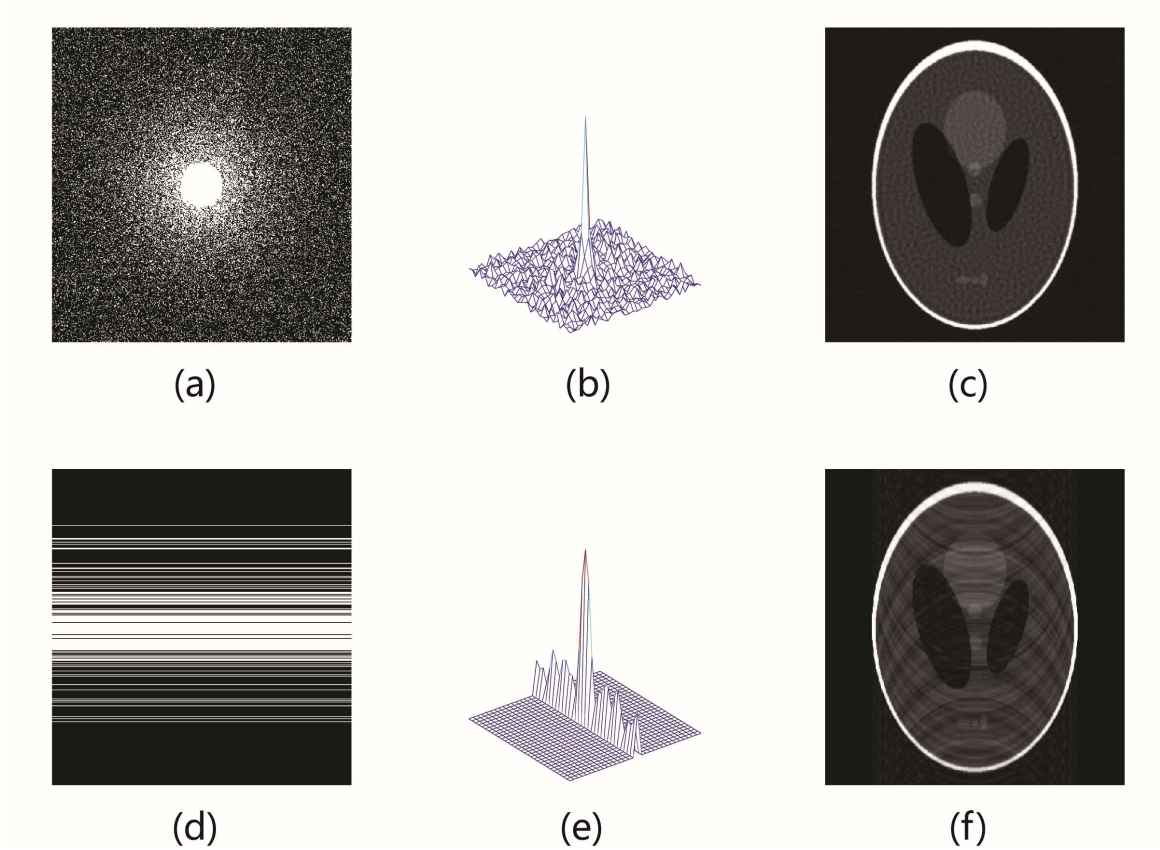

**Figure 4-1. Comparison of 2D random ((a)-(c)) and random phase-encode ((d)-(f)) undersampling patterns. (a) 2D random undersampling; (b) The point spread function (PSF); (c) Reconstructed image with typical artefacts. (d) Random phase-encode undersampling; (e) The PSF; (f) Reconstructed image with typical artefacts.**

In CS-MRI, the 2D random under-sampling (Figure 4-1a) is shown to achieve high incoherence as it obtains a completely random subset of *k*-space [8]. Its PSF profile distributes randomly as shown in Figure 4-1b. It leads to incoherent artefacts in the image domain such as zero-mean random white Gaussian noise (see Figure 4-1c). In the case of random phase-encode under-sampling (see Figure 4-1d), its parallel line sampling trajectory make its achievable incoherence significantly worse than with 2D random under-sampling [8, 120]. The PSF of random phase-encode under-sampling has all the nonzero values assembled on only one column with a peak value in the centre, as illustrated in Figure 4-1e. This reveals all the artefacts existing along the position of the same column (see Figure 4-1f). Meanwhile the random phase-encode under-sampling reduces the incoherence of aliasing interference. This is illustrated by a comparison of typical artefacts caused by these two kinds of random under-sampling schemes, which are shown in Figure 4-1c and Figure 4-1f. From data of PSF in Figure 4-1b and in Figure 4-1e, we find that the incoherence is 10.29 with 2D random under-sampling and 4.37 using random phase-encoding.

### 4.2.3 2D Inverse DFT (IDFT) in sequential 1D IDFTs

In order to reduce the artefacts caused by phase-encode random under-sampling, we decided to split the 2D image reconstruction problem into several parallel 1D signal reconstruction problems.

Normally, the MR images are directly obtained from 2D IDFT of the *k*-space data, as shown in (4-2) as follow:

$$\boldsymbol{I}(m,n) = \sum_{u=0}^{M-1} \sum_{v=0}^{N-1} \boldsymbol{K}(u,v) \exp\left[2\pi i \left(\frac{mu}{M} + \frac{nv}{N}\right)\right] \tag{4-2}$$

$$= \sum_{u=0}^{M-1} \left[\sum_{v=0}^{N-1} \exp\left(\frac{2\pi inv}{N}\right) \boldsymbol{K}(u,v)\right] \exp\left(\frac{2\pi imu}{M}\right) \tag{4-3}$$

where $m \in [0, M-1], n \in [0, N-1]$, ***I***(m,n) means the image with the dimension of M×N, and ***K***(u,v) is the corresponding *k*-space data.

Here, the 2D IDFT actually involves a number of 1D IDFT. Through altering the calculation sequence, the traditional operation of 2D IDFT in (4-2) can be easily split into two 1D IDFTs in sequence as (4-3) illustrated.

A schematic representation is illustrated in Figure 4-2. For the *k*-space data ***K*** with a matrix of M (columns) × N (rows), we firstly apply a 1D IDFT to all the N rows along the frequency direction. This will transform the *k*-space data ***K***(u,v) to ***G***(m,v) of an intermediate domain, in which the horizontal axis corresponds to the dimension **M** in the image domain and the vertical axis represents dimension **V** in the *k*-space domain. As the correlation between each column data of ***K***(u,v) has been decoupled by the 1D IDFT, the column data of ***G***(m,v) are treated independently. In the second process, we apply another 1D IDFT to each unassociated column data of ***G***(m,v). The output of this process 2, the new data ***I***(m,n), will be in image domain.

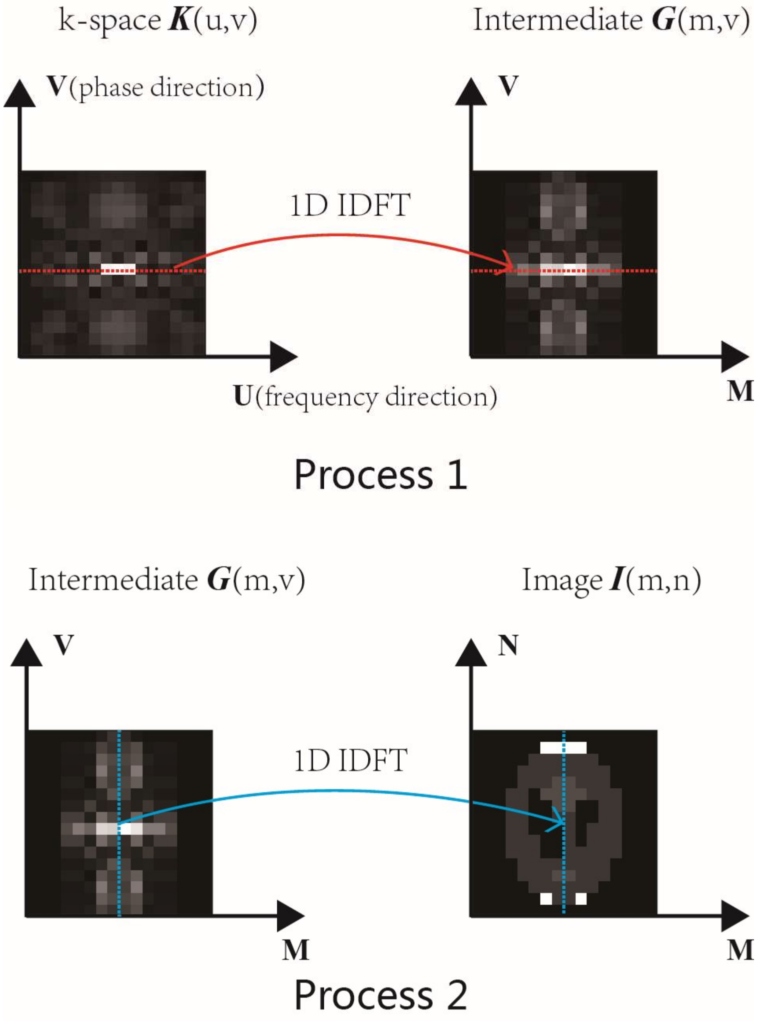

**Figure 4-2. The schematic principle of splitting 2D Inverse Discrete Fourier Transform (IDFT) into sequential 1D IDFTs. A 1D IDFT is applied in process 1 to the rows of *k*-space data *K*(u,v), thus an intermediate data *G*(m,v) is obtained. Then in process 2, another 1D IDFT to the columns of *G*(m,v) will produce the corresponding MR image *I*(m,n).**

### 4.2.4 Proposed method

As explained in section 4.3.3, through sequential 1D IDFTs operation, the 2D image reconstruction has been transformed to recovery of parallel 1D signals. The CS recovery of these 1D signals will take advantage of the excellent incoherence property resulting from the pure random under-sampling along the phase direction. This will essentially help the exploitation of the 1D sparsity and elimination of the coherence aliasing artefacts. The solution of the proposed method is illustrated in Figure 4-3, consisting of the following four steps:

Step 1: 1D random under-sampling along the phase direction. Suppose $\boldsymbol{I}$ is the object MR image with M(columns) ×N(rows) pixels, $\boldsymbol{P}$ is the random phase-encode under-sampling pattern, $\emptyset_{\boldsymbol{P}}$ is the partial Fourier transform with the under-sampling pattern $\boldsymbol{P}$, $\boldsymbol{y} = \emptyset_{\boldsymbol{P}}(\boldsymbol{I})$ consists of the sampled *k*-space data.

Step 2: Transform the *k*-space measurements $\mathbf{y}$ to data $\boldsymbol{g}$ in the intermediate domain $\boldsymbol{G}$ by $\boldsymbol{g}_v = \emptyset_{1D}^{-1}(\boldsymbol{y}_v)$, where $\mathbf{y}_{\mathrm{v}}$ means the $\mathrm{v}_{\mathrm{th}}$ row data of $\boldsymbol{y}$ along frequency direction and $\emptyset_{1D}^{-1}$ is the inverse Discrete Fourier transform (IDFT) of the 1D signal. The 2D data $\boldsymbol{g}$ can be separated in to M columns. Each column contains the 1D data $\boldsymbol{g}_m$ (the $\mathrm{m}_{\mathrm{th}}$ column data of $\boldsymbol{g}$ in intermediate domain, $n \in [1, M]$). The 2D data $\boldsymbol{g}$ has been decoupled by IDFT so that each column data $\boldsymbol{g}_m$ can be processed independently.

Step 3: Parallel 1D signal reconstructions. The 1D signal reconstruction can be solved by the CS algorithm as follows:

$$Min \ \ \|\boldsymbol{\Psi}_{1D}(\boldsymbol{x}_m^{1D})\|_1 \qquad s.t. \ \ \left\|\emptyset_{P_{1D}}(\boldsymbol{x}_m^{1D}) - \boldsymbol{g}_m\right\|_2 < \varepsilon \tag{4-4}$$

where $\emptyset_{\boldsymbol{P}_{1D}}$ is the 1D partial Fourier transform with the under-sampling pattern $\boldsymbol{P}_{ID}$ (one column of $\boldsymbol{P}$), $\boldsymbol{\Psi}_{1D}$ is the 1D total variation (TV) transform [8], $\boldsymbol{x}_m^{1D}$ is the reconstructed 1D signal in the $\mathrm{m}_{\mathrm{th}}$ column data along the vertical direction **N** in the image domain.

Step 4: 2D reconstruction of the image data. Combining the sequentially reconstructed 1D signals $\boldsymbol{x}_m^{1D}, m \in [1, M]$ from step 3, we can obtain the image $\boldsymbol{x}^{1D}$ with the upgraded *k*-space data. Using $\boldsymbol{x}^{1D}$ to set the initial solution $\boldsymbol{x}_0$, we then carry out a 2D CS reconstruction to obtain the final reconstructed image $\boldsymbol{x}$, where $\boldsymbol{\Psi}$ denotes the 2D wavelet transform (as the sparse transform in (4-1)).

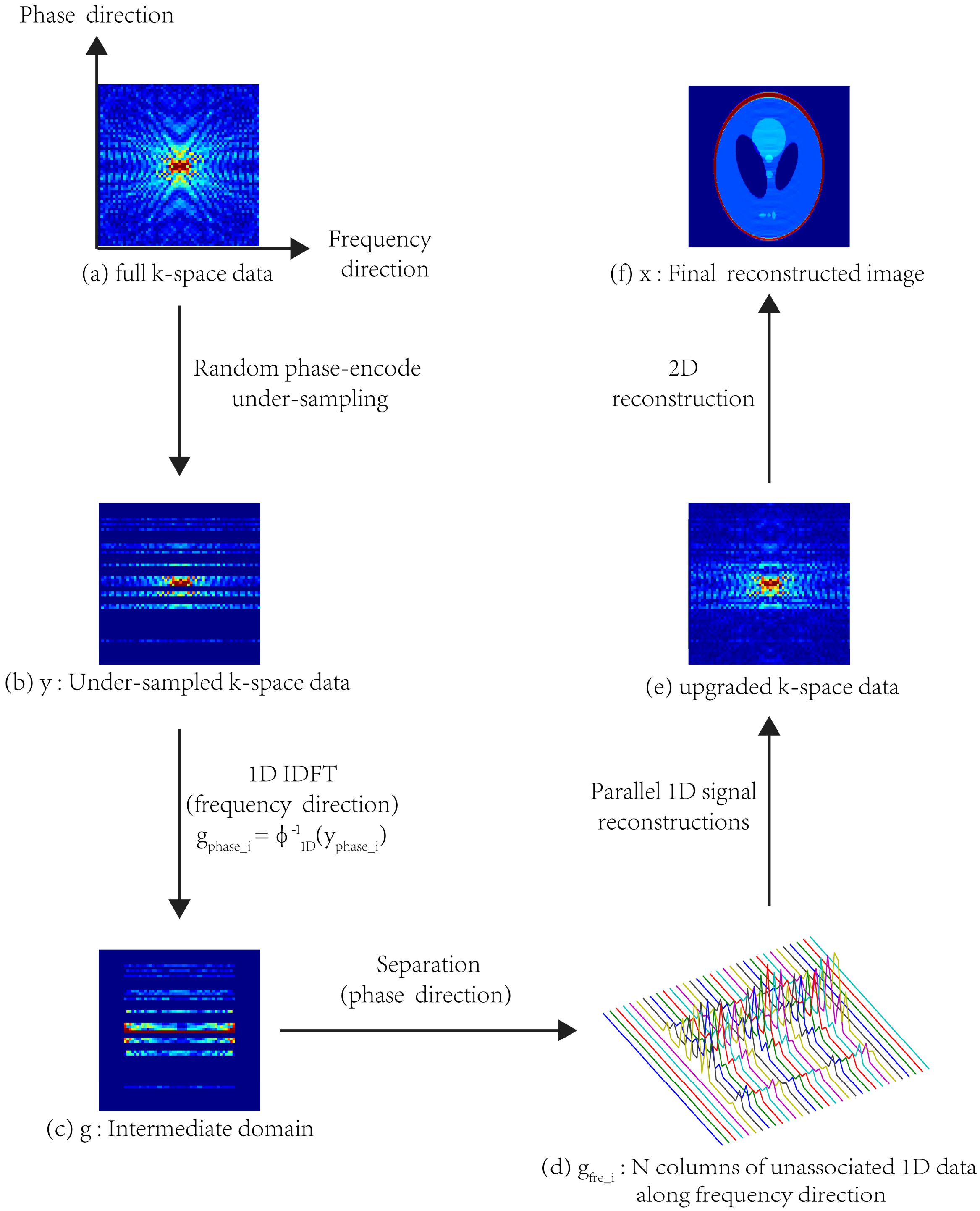

**Figure 4-3. The flow chart of the proposed compressed sensing MRI. In the method, the full *k*-space data (a) is randomly sampled along the phase direction to get the undersampled data (b), which transformed into an intermediate domain via 1D IDFT (c). The intermediate data g will be treated as a series of 1D signals (d) and reconstructed using 1D CS method (e). In the final step, a 2D CS reconstruction of the image will be carried out, with an initial solution obtained from the reconstructed 1D signals (f).**

### 4.2.5 Experimental method

To verify the performance of the proposed method, four typical MR datasets were chosen including cardiac cine, brain, foot and angiography. The cardiac cine MR data was a frame of full *k*-space data acquired using a 1.5T Philips system. The images of brain, foot and angiography were fully sampled using a Siemens Magnetom Avanto 1.5T system. All the considered MR images contain 256×256 pixels.

A variable-density under-sampling scheme was implemented to generate the random phase-encode under-sampling pattern [8]. Gaussian distribution function with zero mean was utilized to sample more in the *k*-space centre. The standard deviation σ was obtained experimentally with different reduction factors.

All simulations were carried out on a computer with an Intel Core i7-3770 eight-core processor and 12GB of memory utilizing Matlab (R2013b: The Mathworks, Natick, MA). The constrained convex optimization problems as shown in Equations (4-1) and (4-4) are converted to unconstrained problem with Lagrangian form [8]:

$$\boldsymbol{Arg}\,\min_{\boldsymbol{x}}(\|\emptyset_{\boldsymbol{P}}(\boldsymbol{x})-\boldsymbol{y}\|_{\mathbf{2}}+\boldsymbol{\lambda}\|\boldsymbol{\Psi}(\boldsymbol{x})\|_{\mathbf{1}}) \tag{4-5}$$

where $\lambda$, as a regularization parameter determines the trade-off between the data sparsity ($l_1$ norm) and consistency ($l_2$ norms). The value of $\lambda$ is experimentally set for different conditions. For exampling, it is $\lambda_{\mathrm{TV}}$=0.001 for 1D reconstructions and $\lambda_{\mathrm{Wavelet}}$=0.001, $\lambda_{\mathrm{TV}}$=0.00174 for 2D reconstructions respectively. A nonlinear conjugate gradients and backtracking line-search [8] was used for solving the optimization problem involved in the CS MRI study. For comparison, the algorithm in [8] is considered as the conventional CS method, which utilizes both Wavelet and TV as sparse transforms.

For a comparison between the proposed and conventional method, both visual and numerical metrics are used for the reconstructed image quality assessment. The differences between the reconstructed images and fully sampled images of both methods were also shown. We used the PSNR (define as equation (3-5)) and SSIM [123] as the numerical criteria for the evaluation of the reconstruction quality.

The SSIM matric is an alternative way for image quality assessment. The SSIM value is computed as follows:

$$SSIM(\boldsymbol{I}, \boldsymbol{I}_{rec}) = \frac{(2\mu_I \mu_{I_{rec}} + c_1)(2\sigma_{I\,I_{rec}} + c_2)}{(\mu_I^2 + \mu_{I_{rec}}^2 + c_1)(\sigma_I^2 + \sigma_{I_{rec}}^2 + c_2)} \tag{4-6}$$

Where $\mu_I$ and $\mu_{I_{rec}}$ are the average pixel values of $\boldsymbol{I}$ and $\boldsymbol{I}_{\mathrm{rec}}$, $\sigma_I^2$ and $\sigma_{I_{rec}}^2$ are the variance of $\boldsymbol{I}$ and $\boldsymbol{I}_{\mathrm{rec}}$, $\sigma_{I\,I_{rec}}$ is the covariance of $\boldsymbol{I}$ and $\boldsymbol{I}_{\mathrm{rec}}$, $c_1$ and $c_2$ are two variables to stabilize the division with weak denominator.

SSIM is used for measuring the similarity between the reference image and the reconstructed image. Different from PSNR estimating the accuracy of each pixel, SSIM is a perception-based model that considers image degradation as perceived change in structural information [123-145]. SSIM is proven to be more consistent with human visual perception.

## 4.3 Results

### 4.3.1 Comparative study of the proposed and conventional CS reconstructions at different reduction factors

To demonstrate the performance degradation with the decreased amount of sampled data using the random phase-encode under-sampling scheme, PSNR curves of the conventional [8] and proposed methods were plotted at different reduction factors of 2, 4, 6, 8 and 10. In Figure 4-3, we can see the proposed method has a gain of PSNR from 2 to 8 dB compared with the conventional approach. From Figure 4-4 we can see that, at higher reduction factors, the conventional method cannot keep the PSNR at a high value. It reveals that the aliasing artefacts degrade the image quality and that the conventional method cannot effectively suppress these artefacts. In contrast, the improvements of the proposed method are more obvious for the cases with higher reduction factors. For standard MR images such as cardiac cine, brain and foot, the PSNR improvements are 3.12 dB, 3.29 dB and 2.04 dB of respectively (see Figure 4-4a, Figure 4-4b, Figure 4-4c) when the reduction factor is set as 10. For sparse MR images as in the case of angiography, the quality improves by 4.94 dB of the PSNR, much higher than the situation of standard MR images as Figure 4-4(d) shows.

The reconstruction errors of the conventional method and the proposed method are also measured by SSIM in Table 4-1. At the low reduction factors, such as R = 2 or 4, both methods have good performance in all the cases and the SSIM values are all above 0.94. This reveals that, there is almost no visual difference between the reference and the reconstructed images. When the reduction factors are over 4, however, we can see the SSIM value of the conventional method reduces, which means

**Table 4-1. SSIM indexes of the reconstrctions by conventional and the proposed method**

| | Cardiac Cine (Proposed / Conventional) | Brain (Proposed / Conventional) | Foot (Proposed / Conventional) | Angiography (Proposed / Conventional) |
|---|---|---|---|---|
| R = 2 | 0.9707 / 0.9703 | 0.9743 / 0.9714 | 0.9678 / 0.9674 | 0.9947 / 0.9933 |
| R = 4 | 0.9445 / 0.9404 | 0.9559 / 0.9075 | 0.9390 / 0.9438 | 0.9855 / 0.9859 |
| R = 6 | 0.8966 / 0.8642 | 0.9012 / 0.8487 | 0.9049 / 0.8796 | 0.9598 / 0.8997 |
| R = 8 | 0.8798 / 0.7851 | 0.8658 / 0.7671 | 0.8917 / 0.7945 | 0.9516 / 0.8059 |
| R = 10 | 0.8401 / 0.6842 | 0.8458 / 0.7086 | 0.8621 / 0.7187 | 0.9218 / 0.6968 |

the reconstructed images are obviously blurred with the aliasing artefacts introduced by the random phase-encode under-sampling pattern. In contrast, with high reduction factors, the SSIM value of the proposed method still maintains at a stable level (over 0.84). These prove the reconstructed images are with an acceptable quality.

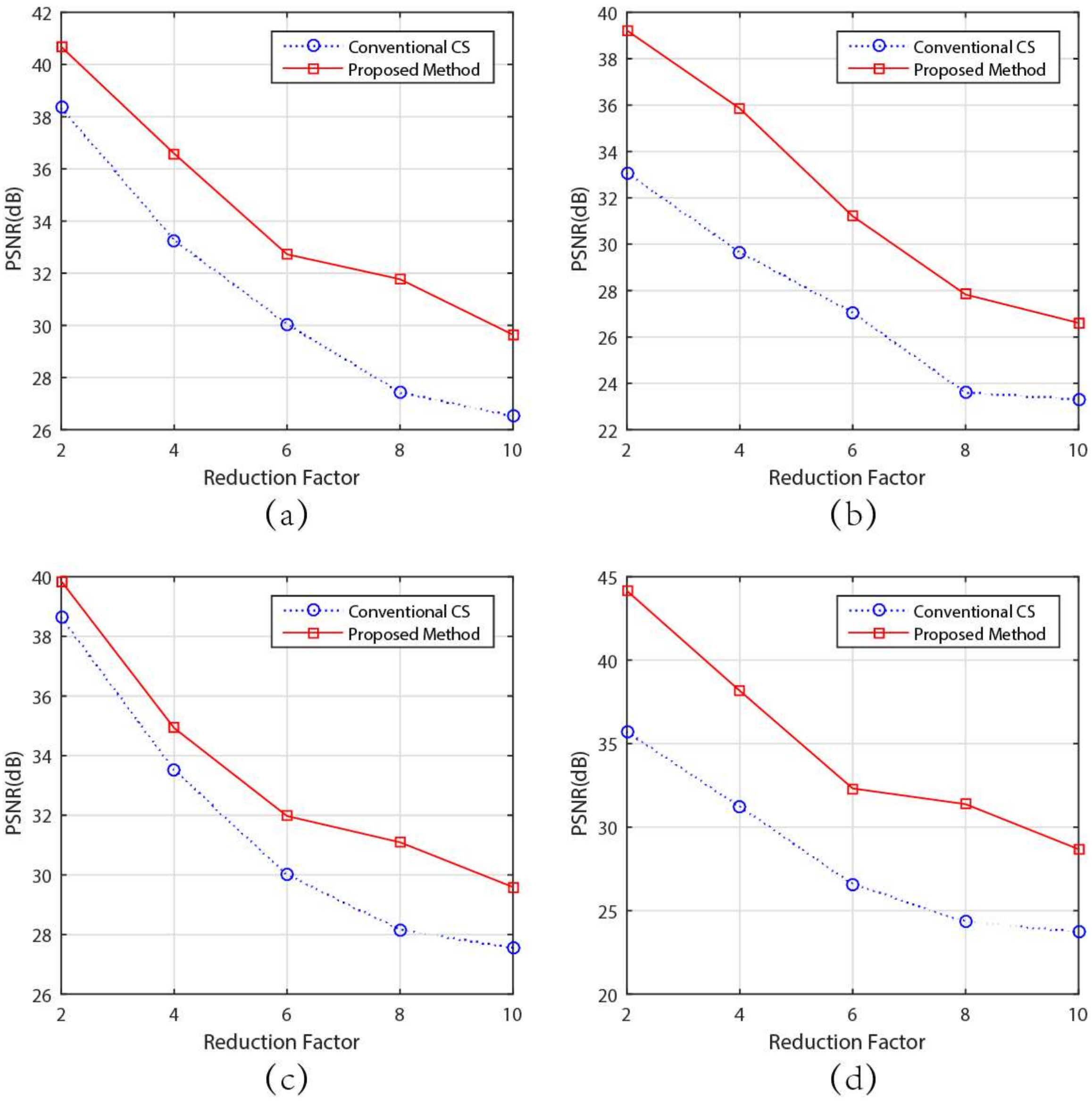

**Figure 4-4. Performance comparison between conventional CS and the proposed method at different reduction factors in the case of (a) cardiac cine image; (b) brain image; (c) foot image; (d) angiography image.**

### 4.3.2 Comparative study of the proposed and conventional CS reconstructions in image quality

We compared the reconstruction performance of the conventional method and the proposed method at the reduction factor of 6 (16.67% of the fully sampled data). It is noted that there are 256 phase encoding lines in total in the original full *k*-space data.

The reconstruction results of the proposed and conventional method are shown in Figure 4-5. In the case of cardiac cine, there is blurring around the cardiac boundary in the image reconstructed by the conventional method (see Figure 4-5a). It is caused by the aliasing artefacts, which become more severe at high reduction factors (such as R = 6). Compared with conventional CS, the proposed method produced clearer structures, shown in Figure 4-5(b). Compared with the difference images Figure 4-5(c) and Figure 4-5(d), the difference image between the images obtained from the full *k*-space data and CS reconstructed image, it is easy to see that the proposed method effectively reduced the aliasing artefacts. For example, see the arrows in Figure 4-5(c) and Figure 4-5(d).

In cardiac cine MRI, the myocardial deformation is our main interest. The myocardial structure is depicted by contours as shown in Figure 4-6(b), which defines the region of interest (ROI). For the reconstruction of the myocardium in the ROI, it is easy to see that the reconstruction errors of the conventional CS (see Figure 4-6c) are much larger than that of our new method (see Figure 4-6d).

We further compared the methods with brain and foot imaging. As shown in Figure 4-7 and Figure 4-8, similar reduction of the aliasing artefacts can be observed near the tissue boundaries.

The aliasing artefacts were exacerbated in those images with sparsity in the pixel domain such as angiography (see Figure 4-9). In these cases, the improvement of the proposed method was clear when compared with conventional one. The weak incoherence of random phase-encode under-sampling patterns limited conventional method in removing artefacts, as can be seen in Figure 4-9(c) where the red arrows point to the artefacts. In contrast, as shown in Figure 4-9(d), the proposed method consistently outperforms the conventional CS method producing images with small residual errors near the blood vessels.

To illustrate the reconstruction performance of both methods at other reduction factor, we chose brain imaging at R = 4 as a typical case for comparison (see Figure 4-10).

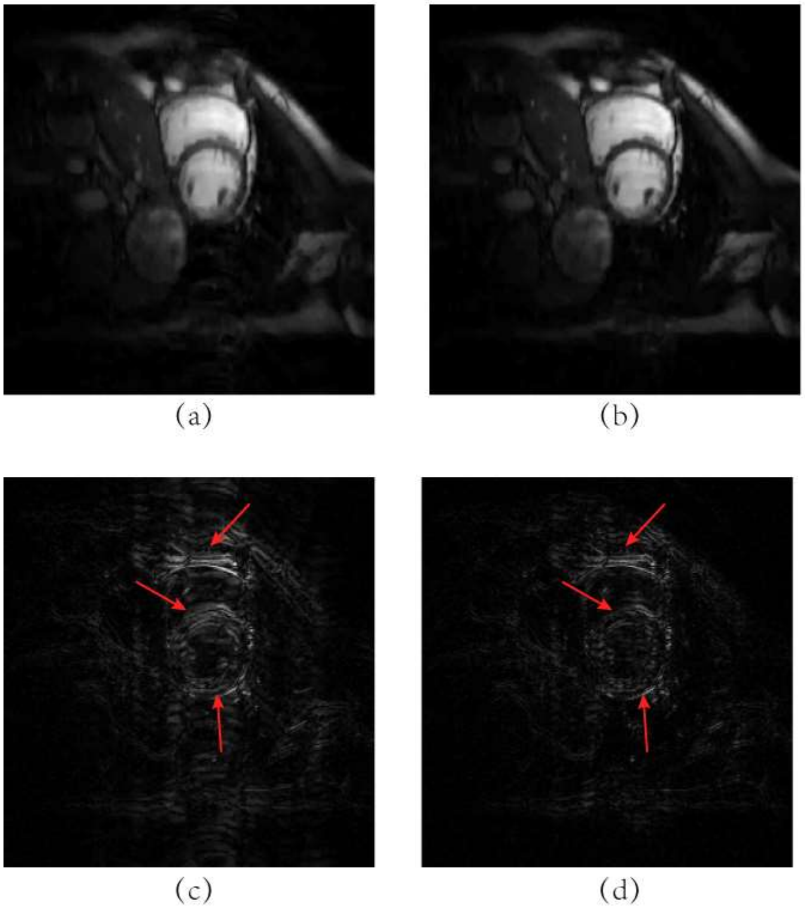

**Figure 4-5. Reconstructed images of cardiac cine MR data （top row images） and difference images (bottom row images) at R = 6. From left to right the applied algorithms are: conventional and proposed method.**

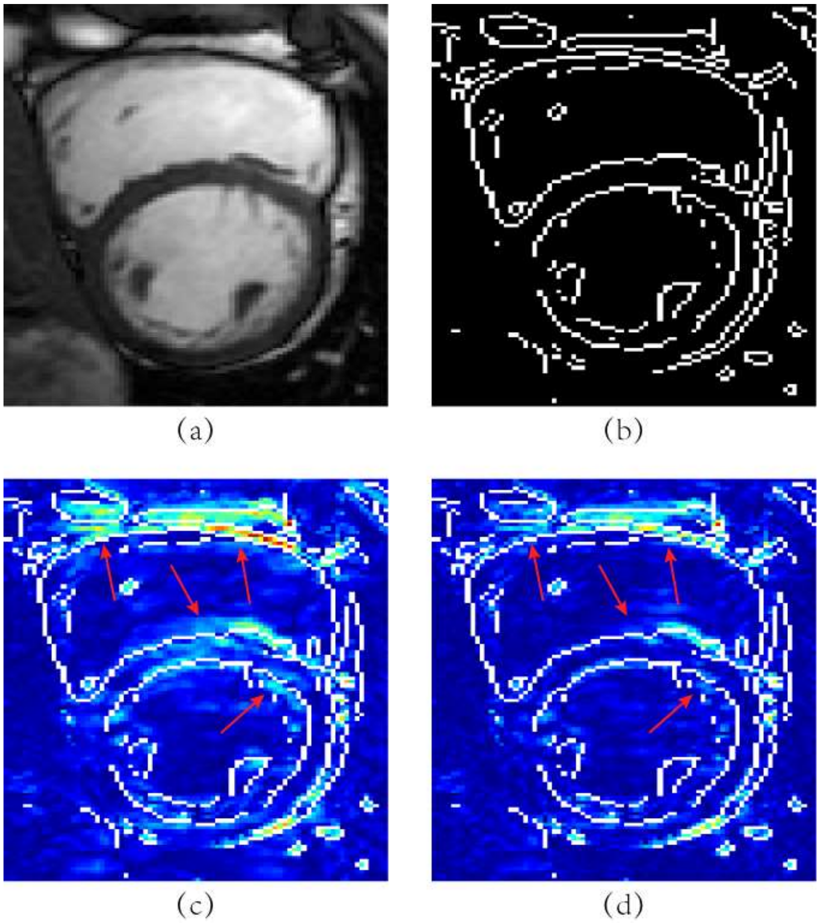

(a) (b)

(c) (d)

**Figure 4-6. Comparison of difference images Figure 4-5(c) and Figure 4-5(d) in the region of interest (ROI). (a) shows the original image in ROI and (b) shows the contour of image in ROI. The difference images in ROI mapping with the contour: (c) with conventional CS, (d) with proposed method.**

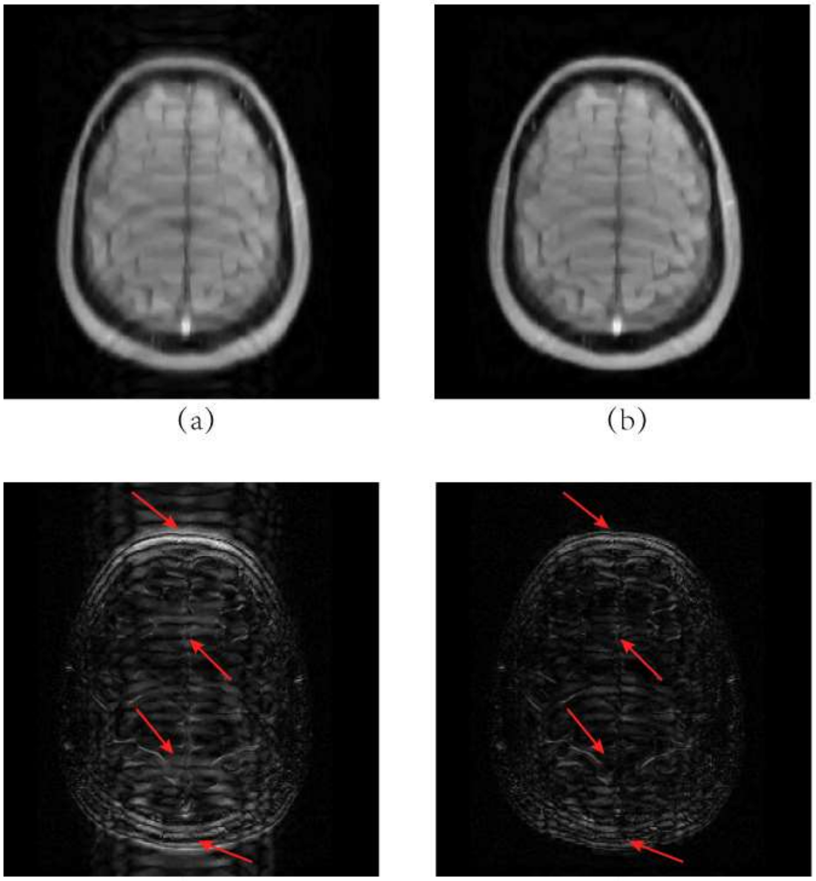

(a) (b)

(c) (d)

**Figure 4-7. Reconstructed images of brain MR data （top row images） and difference images (bottom row images) at R = 6. From left to right the applied algorithms are: conventional and the proposed method.**

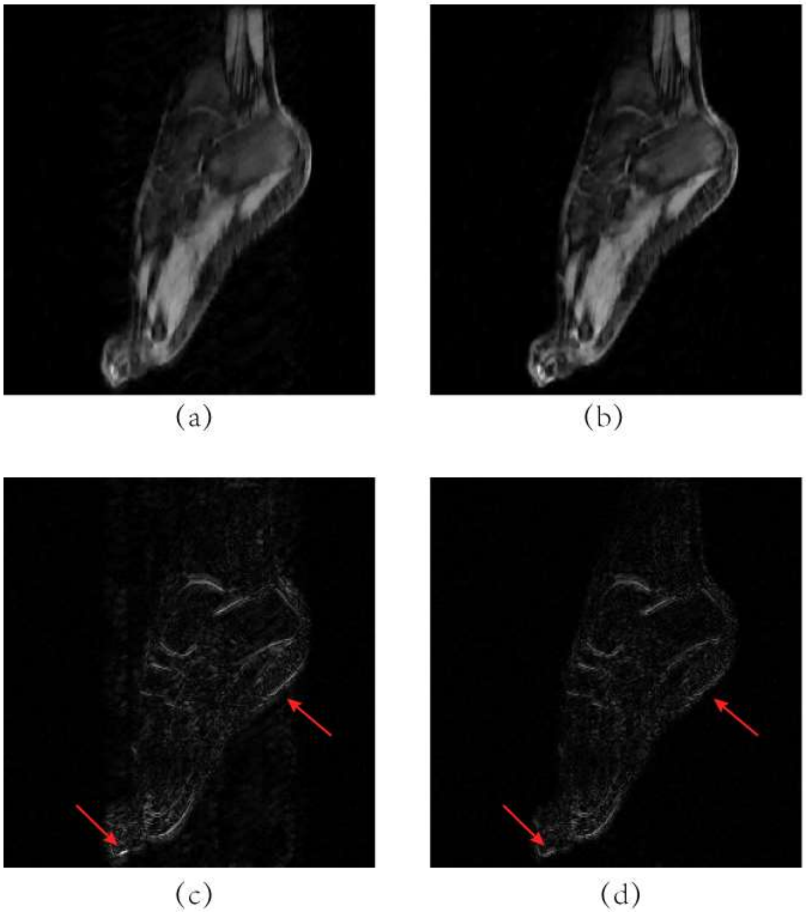

**Figure 4-8. Reconstructed images of foot MR data （top row images） and difference images (bottom row images) at R = 6. From left to right the applied algorithms are: conventional and proposed method.**

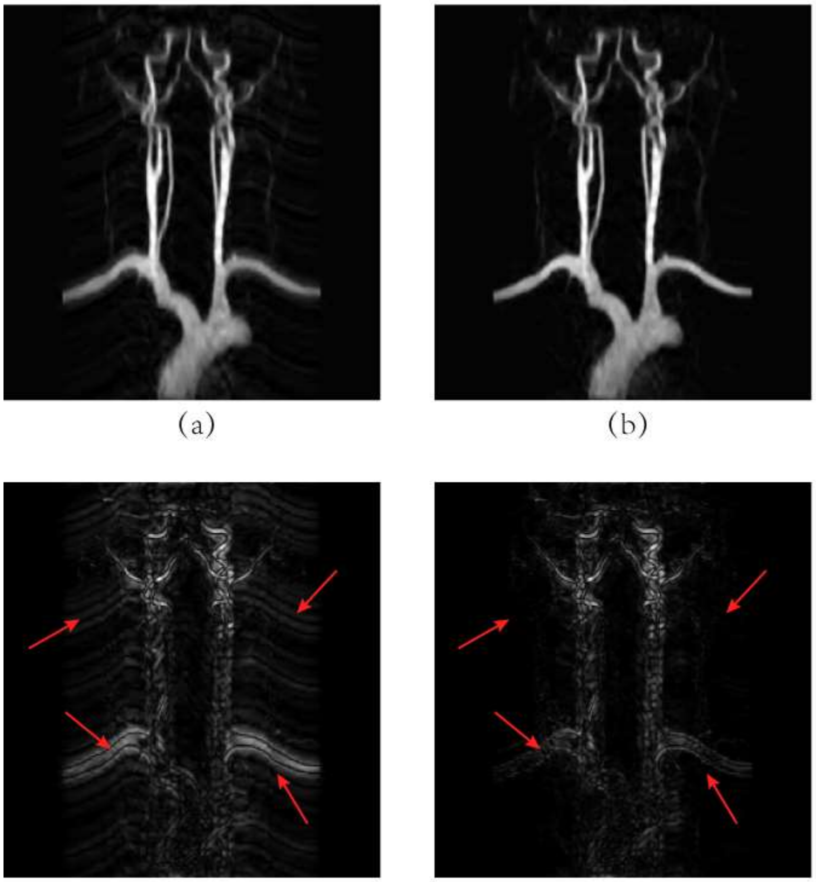
(a) (b) (c) (d)

**Figure 4-9. Reconstructed images of angiography MR data （top row images） and difference images (bottom row images) at R = 6. From left to right the applied algorithms are: conventional and proposed method.**

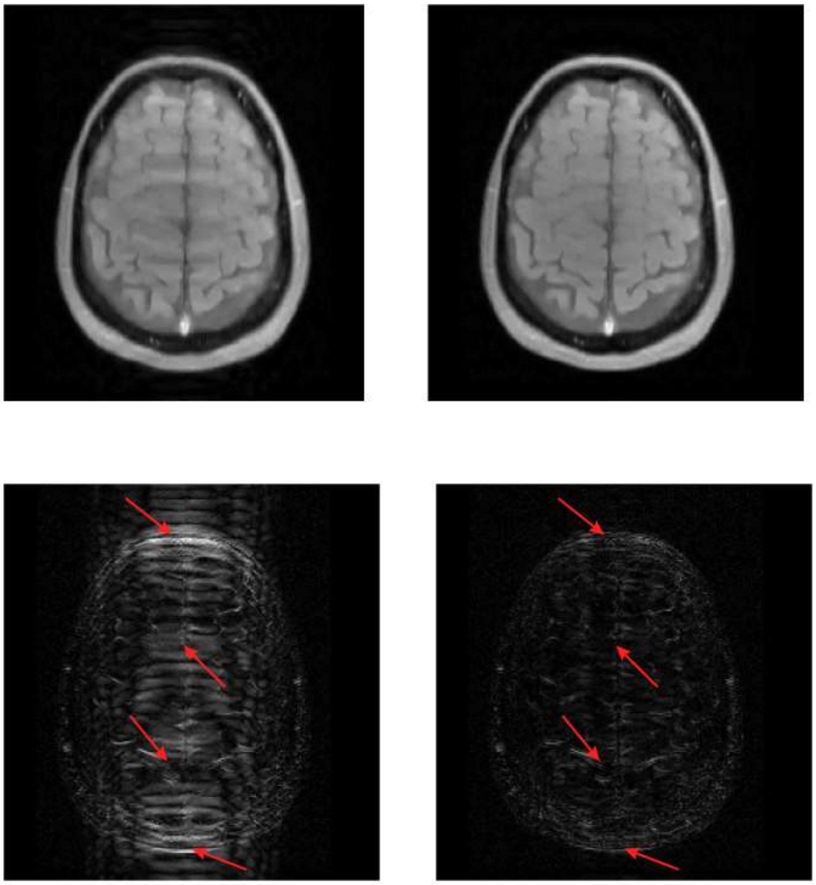

(c) (d)

Figure 4-10. Reconstructed images of brain MR data （top row images） and difference images (bottom row images) at R = 4. From left to right the applied algorithms are: conventional and the proposed method.

## 4.4 Discussion

### 4.4.1 Reconstruction artefacts reduction

In this work, we reduced the dimension of the reconstruction problem from 2D to 1D, in which excellent 1D randomness in the phase direction facilitate the incoherence property for CS reconstruction. As Figure 4-11(b) illustrates, the output of the 1D reconstruction in the proposed method eliminated the majority of the aliasing artefacts when compared with the image transformed from the under-sampled *k*-space data (see Figure 4-11a). The comparison of the difference images (see Figure 4-11e, Figure 4-11f) may indicate the artefacts suppression more clearly. Nevertheless, in comparison with the conventional CS method (see Figure 4-11c), the result of the 1D reconstruction only is unacceptable yet. Though aliasing artefacts were not entirely eliminated (see Figure 4-11g), the reconstruction error of the conventional method was smaller than that in Figure 4-11(f). In the proposed method, we utilized the outputs of the 1D reconstruction (see Figure 4-11b) as an improved initial solution, and undertake a follow-up 2D CS reconstruction procedure. In the 2D reconstruction, signal correlations along both directions (phase and frequency) are considered, therefore further exploiting the signal sparsity to produce a better solution (see Figure 4-11d). As shown in Figure 4-11(h), the aliasing artefacts of the proposed method were minimized.

### 4.4.2 Extension of the proposed method

The 1D TV transform and 2D wavelet transform were implemented as the sparsity base in the parallel 1D signal reconstructions and 2D reconstruction of the proposed method. Other sparsity bases can also be applied to the proposed method, such as wavelet transform, Walsh transform [109] and tensor decomposition based transform [80], for specific imaging studies. The developed algorithm can be easily combined with parallel MR imaging, for more rapid imaging studies.

### 4.4.3 GPU acceleration

In the above four $256 \times 256$ MR image reconstruction studies, the average computation times of the conventional CS and the proposed method are 164 seconds and 235 seconds, respectively. Although the new method is slightly slower than conventional CS methods, as the proposed method dissembles 2D image reconstruction into several independent 1D signal reconstructions, it is thus quite straightforward to implement with GPU computing, for solving the formed 1D optimization problems

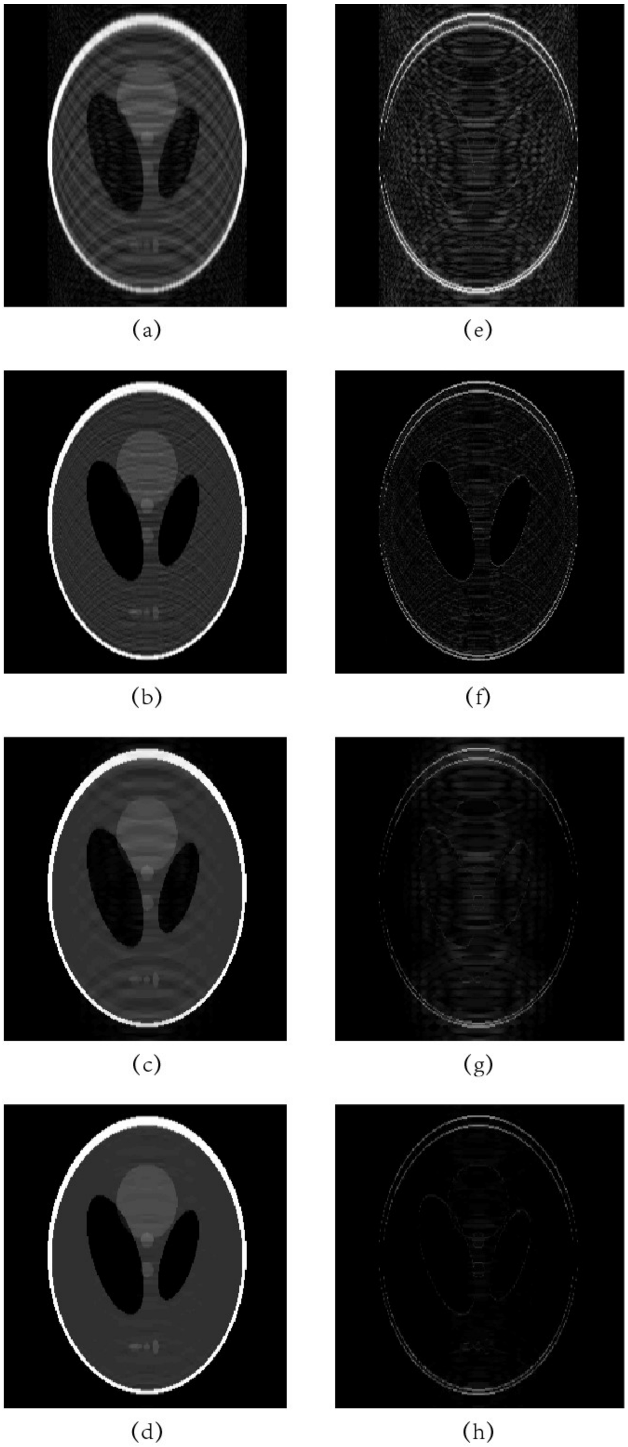

**Figure 4-11. Reconstructed images of phantom（left column images） and difference images ( right column images) at R = 4. From up to down the applied algorithms are: zero padding, only 1D reconstruction in the proposed method, conventional CS and proposed method.**

in parallel [124, 125]. With a successful GPU parallelization of the algorithm in the future, the efficiency of the proposed method can be significantly enhanced, thus has the potential to be applied to real-time reconstruction.

## 4.5 Conclusion

In this chapter, we have presented a novel reconstruction scheme for the application of CS in conventional Cartesian MRI. The proposed method is capable of eliminating large coherent aliasing artefacts introduced by random phase-encode under-sampling patterns. The theoretical analysis and imaging experiments have demonstrated that the proposed approach can effectively improve the reconstructed image quality in various MR imaging cases at different reduction factors. In future work, we plan to apply the proposed algorithm to various CS MRI applications.

# 5. Pseudo-Polar Fourier Transform based Compressed Sensing MRI

To overcome problems of applying radial trajectory in CS MRI, a radial-like pseudo-polar trajectory and the corresponding transform were approached to combine with CS in this chapter. The pseudo-polar trajectory preserves all the essential properties of radial trajectory and allows an accurate image reconstruction with pseudo-polar FFT instead of the traditional regridding and inverse-regridding process in radial trajectory.

This chapter is almost entirely based on a journal paper, "Pseudo-Polar Fourier Transform based Compressed Sensing MRI", accepted for publication by *IEEE Transactions on Biomedical Engineering*.

***Publication details***

Yang Yang, Feng Liu, Mingyan Li, Ewald Weber, Qinghuo Liu and Stuart Crozier, "Pseudo-Polar Fourier Transform based Compressed Sensing MRI," *IEEE Transactions on Biomedical Engineering*, 2016, accepted.

***Manuscript history***

| | |
|---|---|
| Received | 3 Dec 2015 |
| Interim Decision (major revision) | 20 Jan 2016 |
| Revision submission | 18 Mar 2016 |
| Interim Decision (major revision) | 24 Apr 2016 |
| Revision submission | 23 May 206 |
| Accepted | 4 Jun 2016 |

***Author contribution***

| Contributor | Statement of contribution |
|---|---|
| Yang Yang | Methodology development, code implementation, experimental design, execution of experiments, analysis and interpretation, manuscript preparation |
| Feng Liu | Analysis and interpretation, manuscript reviews |
| Mingyan Li | Experimental design, execution of experiments, analysis and interpretation, manuscript reviews |
| Jin Jin | Experimental design, execution of experiments, analysis and interpretation, manuscript reviews |
| Ewald Weber | Analysis and interpretation, manuscript reviews |
| Qinghuo Liu | Analysis and interpretation, manuscript reviews |
| Stuart Crozier | Analysis and interpretation, manuscript reviews |

## 5.1 Introduction

As a typical non-Cartesian sampling trajectory in Magnetic Resonance Imaging (MRI), radial trajectory has a number of advantages over its Cartesian counterpart [126, 127]. For instance, in radial trajectory, the low-frequency region of the *k*-space centre is inherently oversampled, which provides superior performance in motion artefact reduction in dynamic MRI [128, 129]. In addition, radially sampled *k*-space may provide improved temporal resolution throughout the field of view (FOV), which can be used to reduce the total scan time, as demonstrated in angularly under-sampled projection-reconstruction (PR) for 3D cardiac MR (CMR) [130, 131]. Another important application of radial trajectories is its use in conjunction with Compressed Sensing (CS). The latter exploits sparsity of signals in some transformation domains and thus reconstruct MR images using far less data than fully sampled ones [7, 8]. There are some unique properties of radial trajectory that make it a promising method for CS reconstruction. Firstly, each ray of the radial trajectory carries an equal amount of low and high frequency information of *k*-space [132]. In contrast, the important low spatial frequency components are concentrated in a small number of lines of the Cartesian *k*-space [132], thus creating a difficulty in balancing the acquisition of both components in under-sampling scheme. Secondly, the aliasing artefacts of a radial under-sampling are scattered to various readout directions. Therefore, the incoherence of its point-spread function (PSF) makes the artefacts less pronounced and more noise-like [108]. With less coherence artefacts, the image sparsity can be further exploited when combining radial trajectories with fast imaging schemes such as FOCUSS [133], *k*-t FOCUSS [134] and the total variation regularization method [8].

To reconstruct images from radially sampled *k*-space, interpolation plays an important role. Typically, it is implemented either in the image domain (such as the filtered back projection method) or in the frequency domain (such as the regridding method) [17, 102, 119, 130, 135-138]. The filtered back projection method transforms the data along a ray of radial trajectory into a projection then back again, to produce a two (or three) dimensional image. In order to improve the reconstruction quality, the projection profiles are convolved with a suitable mathematical function (filter) prior to back projection. The regridding method uses convolution to interpolate the radial data onto a Cartesian grid in the frequency domain, and the approximated Cartesian data can be subsequently processed by the standard Fast Fourier Transform (FFT) [102, 130]. Essentially, these two methods are equivalent and theoretically achieve similar reconstruction accuracy.

However, the filter selection in the back projection reconstruction is one of the major problems in clinical imaging [102]. Additionally, the projection process should be linear, which is difficult to achieve practically, owing to eddy current distortions and hardware imperfections. Therefore, the regridding algorithm is more popular because it is easier to be adapted to any other non-Cartesian trajectory [102]. Nevertheless, regridding methods involve significant computation, which in practice limits the application of radial trajectory in the CS MRI. This is particularly evident in those iterative CS based algorithms where the regridding and inverse-regridding operations are performed in each iteration [101, 102]. Furthermore, the interpolations in each iteration generates inaccurate data in the *k*-space, leading to areas with a piecewise constant and artefactual edges [102].

In recent years, a radial-like, pseudo-polar (PP) trajectory has been developed to avoid the above regridding / inverse-regridding operation [82, 139, 140]. This efficient pseudo-polar FFT (PPFFT) operation completely avoids the 2D interpolation, and it involves only a PPFFT operation, which has similar computational complexity as a Cartesian 2D-FFT.

In this chapter, we propose a novel method that will reconstruct MR images with a CS algorithm from under-sampled *k*-space data with a pseudo-polar trajectory. This method takes advantage of the PPFFT to eliminate errors associated with the iterative regridding algorithms and PP trajectory to preserve the details. Simulations and experiments are used to demonstrate the performance of the proposed method.

## 5.2 Theory

### 5.2.1 Pseudo-Polar grid

Based on the definition of a polar-like 2D grid, the points of pseudo-polar grid in the *k*-space domain of normalized region of $[-1,1]^2$ can be separated into two subsets, that is, basically vertical (BV) and basically horizontal (BH), which can be mathematically described as [82]:

$$\mathrm{BH} = \begin{Bmatrix} \xi_y = \frac{v}{N} \text{ for} - N \le v < N, \\ \xi_x = \xi_y \cdot \frac{2u}{N}, \text{for} - \frac{N}{2} \le u < \frac{N}{2} \end{Bmatrix} \tag{5-1}$$

$$\mathrm{BV} = \begin{Bmatrix} \xi_x = \frac{v}{N} \text{ for} - N \le v < N, \\ \xi_y = \xi_x \cdot \frac{2u}{N}, \text{for} - \frac{N}{2} \le u < \frac{N}{2} \end{Bmatrix} \tag{5-2}$$

where $\xi_x$ and $\xi_y$ are the coordinates of the grid point along x axis and y axis in the *k*-space, respectively. N is the size of the corresponding signal in the time domain. The grid is illustrated in Figure 5-1, where the BH points are marked with empty circles and the BV ones are marked with filled circles. Adapted from (5-2), the BV rays have equispaced slope: $\frac{\xi_y}{\xi_x} = \frac{2u}{N}, \text{for} - \frac{N}{2} \le u < \frac{N}{2}$. The BH rays are similar but with clockwise rotation of 90 degrees. The equispaced slope of BV and BH rays are defined as the equal-slope rays for pseudo-polar grid. Instead of having the concentric circles and equal-angle spokes in the radial grid, the pseudo-polar grid has the concentric squares and equal-slope spokes, which are depicted in Figure 5-1. Overall, $4N^2$ frequency sampling points, including BH and BV points, are generated from an image of size $N \times N$. All of these $4N^2$ pseudo-polar acquisitions fall exactly onto a $N^2 \times N^2$ Cartesian grid (see Figure 5-1 as an example for N = 4). The $4N^2$ data points are stored in a $2N \times 2N$ matrix. BH points are saved in the first N columns, where the column index and row index of the matrix correspond to the horizontal index u and vertical index v of the data points. BV points are saved in the same way for the rest N columns. The data structure of the matrix implies that, each row contains the points along one spoke and each column contains the points along one concentric square. On average, the pseudo-polar trajectory has nearly 4 times as many samples in the *k*-space as an equivalent Cartesian sampling, which ensures a good numerical stability of pseudo-polar Fourier transform.

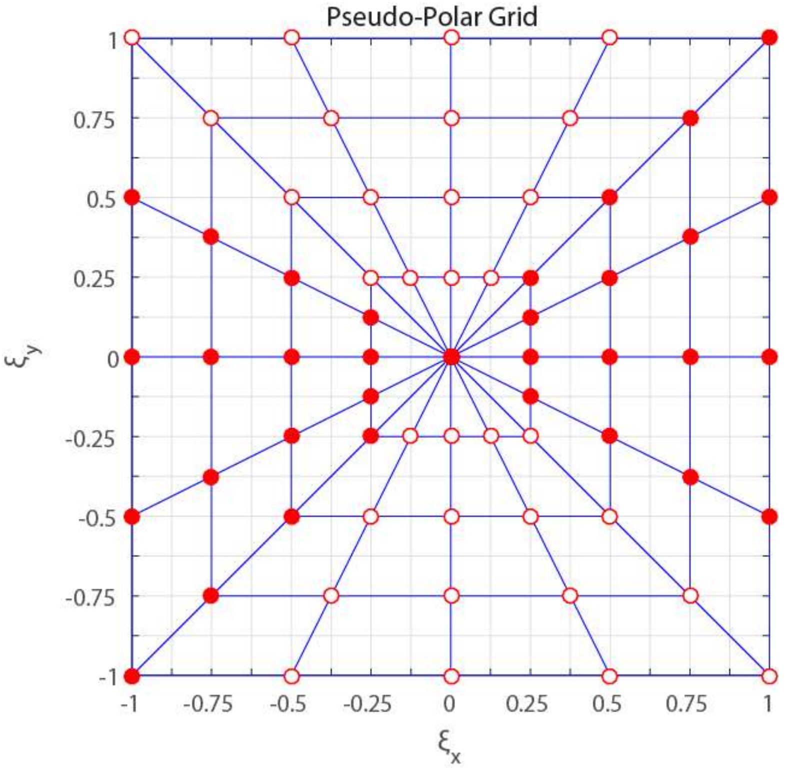

**Figure 5-1. The pseudo-polar grid consists of BH points (empty circles) and BV points (filled circles) when N = 4. The coordinates intersect into 4 concentric squares and 8 equal-slope spokes.**

### 5.2.2 Pseudo-Polar fourier transform

With a given 2D image $\boldsymbol{I}(\mathrm{m},\mathrm{n}), 0 \leq \mathrm{m},\mathrm{n} < \mathrm{N}$, its Fourier transform on the pseudo-polar grid can be obtained as follows [119]:

$$\boldsymbol{K}(\xi_x, \xi_y) = \sum_{m=0}^{N-1} \sum_{n=0}^{N-1} \boldsymbol{I}(m,n) \cdot \exp(-i(m\xi_x + n\xi_y)) \tag{5-3}$$

To the BH points $\boldsymbol{K}_{\mathrm{BH}}$, we can substitute the coordinates from (5-1) and obtain:

$$\boldsymbol{K}_{\mathrm{BH}}(\xi_x,\xi_y) = \boldsymbol{K}_{\mathrm{BH}}(\mathrm{u},\mathrm{v}) = \sum_{x=0}^{N-1}\sum_{y=0}^{N-1}\boldsymbol{I}(\mathrm{m},\mathrm{n})\cdot\exp\left(-\mathrm{i}\left(\frac{2\pi\mathrm{muv}}{\mathrm{N}^2}+\frac{\pi\mathrm{nv}}{\mathrm{N}}\right)\right) \tag{5-4}$$

$$= \sum_{m=0}^{N-1}\exp(-\frac{\mathrm{i}2\pi\mathrm{m}}{\mathrm{N}^2})\sum_{n=0}^{N-1}\boldsymbol{I}(\mathrm{m},\mathrm{n})\cdot\exp(-\frac{\mathrm{i}\pi\mathrm{nv}}{\mathrm{N}}) \tag{5-5}$$

where u and v are the indexes of the corresponding $\boldsymbol{K}_{\mathrm{BH}}$ point coordinates $\xi_x$ and $\xi_y$.

The inner summation part in Equation (5-5) becomes:

$$\boldsymbol{G}_{\mathrm{BH}}(\mathrm{m},\mathrm{v}) = \sum_{n=0}^{N-1}\boldsymbol{I}(\mathrm{m},\mathrm{n})\cdot\exp\left(-\frac{\mathrm{i}\pi\mathrm{nv}}{\mathrm{N}}\right) = \sum_{n=0}^{2N-1}\boldsymbol{I}(\mathrm{m},\mathrm{n})\cdot\exp\left(-\frac{\mathrm{i}2\pi\mathrm{nv}}{2\mathrm{N}}\right) \tag{5-6}$$

Equation (5-6) is actually a 1D-FFT on the columns of $\boldsymbol{I}(\mathrm{m},\mathrm{n})$ with zero padding and can be processed directly using regular 1D-FFT algorithm.

With the result of equation (5-6), we can precede with the outer summation in equation (5-5) as:

$$\boldsymbol{K}_{\mathrm{BH}}(\xi_x,\xi_y) = \boldsymbol{K}_{\mathrm{BH}}(\mathrm{u},\mathrm{v}) = \sum_{m=0}^{N-1}\boldsymbol{G}_{\mathrm{BH}}(\mathrm{m},\mathrm{v})\exp(-\frac{\mathrm{i}2\pi\mathrm{m}}{\mathrm{N}}\cdot\frac{\mathrm{v}}{\mathrm{N}}) \tag{5-7}$$

Without the factor $\alpha = \frac{\mathrm{v}}{\mathrm{N}}$ in the exponent function, equation (5-7) is a regular 1D-FFT, applied on the rows of $\boldsymbol{I}(\mathrm{m},\mathrm{n})$. Here, we use Fractional Fourier Transform (FRFT) to calculate the summation in equation (5-7) [82, 101, 138]. The results will be stacked in an array with 2N rows and N columns.

BV points can be processed in a similar fashion. After processing both the HV and BV points, the pseudo-Polar FFT results will be stored in a matrix $\boldsymbol{T}_{\mathrm{PP}} \in \mathbb{C}^{4\mathrm{N}^2\times\mathrm{N}^2}$.

The inverse Fourier transform can be implemented using the least-squares (LS) method [102, 140], and specifically, the inversion is achieved by solving the following minimization problem:

$$\boldsymbol{I} = \mathrm{Arg}\ \min_{\boldsymbol{I}}\|\boldsymbol{T}_{\mathrm{PP}}\boldsymbol{I}-\boldsymbol{K}\|_2^2 = \left(\boldsymbol{T}_{\mathrm{PP}}^{\mathrm{H}}\boldsymbol{T}_{\mathrm{PP}}\right)^{-1}\boldsymbol{T}_{\mathrm{PP}}^{\mathrm{H}}\boldsymbol{K} \tag{5-8}$$

The above equation is computationally expensive; an iterative approach is used instead:

$$\boldsymbol{I}_{\mathrm{i}+1} = \boldsymbol{I}_{\mathrm{i}} - \boldsymbol{D}\boldsymbol{T}_{\mathrm{PP}}^{\mathrm{H}}(\mathrm{T}_{\mathrm{PP}}\boldsymbol{I}_{\mathrm{i}}-\boldsymbol{K}) \tag{5-9}$$

where i stands for the current iteration step, $\boldsymbol{D}$ is a positive-definite matrix to control the descent of each iteration step (for details, see [82]). As shown in [82], a proper $\boldsymbol{D}$ can ensure good convergence of the corresponding algorithm. In the current study, ***D*** was determined in a similar fashion to previous works [82, 101].

### 5.2.3 Comparison between the pseudo-polar and polar methods

To analyse the properties of the pseudo-polar grid and corresponding PPFFT further, we compare them to those of the radial grids and traditional regridding methods. Suppose the object MR image I has 32 × 32 pixels, and its pseudo-polar grid and radial grid in the *k*-space are shown in Fig. 2. According to the theory in II.A and Nyquist-Shannon sampling theorem, the pseudo-polar grid (see Figure 5-2a) contains 64 rays with 64 points on each ray and the radial grid (see b) has 50 rays with 32 points on each ray [138]. It is evident that the pseudo-polar grid covers more high frequency parts of the *k*-space, therefore contains more information of image details.

A numerical Shepp-Logan phantom with 256×256 pixels (see Figure 5-3a) is used to analyse the accuracy of PPFFT and traditional regridding methods [137]. The pseudo-polar grid is defined as a set of 512 rays with 512 points on each ray. The radial grid contains 402 full-length rays with 512 points, where the two-fold oversampling is applied along the readout direction to avoid the effects from aliasing sidelobes of the convolution in traditional regridding methods [137, 141]. Non-Uniform Fast Fourier Transformation (NUFFT) [137] is implemented as the traditional regridding method. Firstly, the phantom is transformed from the image domain to the corresponding *k*-space domains. For a numerical comparison, the *k*-space data are inversely transformed from the *k*-space back to the image domain. The reconstructed image by PPFFT (see Figure 5-3b) and the one by the regridding method (see Figure 5-3c) are then compared to the original image. The dual interpolations during inverse-regridding and regridding operations introduce numerical error as shown in Figure 5-3(d). Based on a 1D FFT, the PPFFT can more accurately reconstruct the image as shown in Figure 5-3 (e). Comparing Figure 5-3(d) and Figure 5-3(e), we see that the main reconstruction errors of the regridding method concentrate near the image edge or regions with fine detail. In addition to the interpolation-introduced error, the reconstruction inaccuracy is also caused by the omission of the high frequency part in the radial *k*-space data as the arrow in Figure 5-2(d) illustrates.

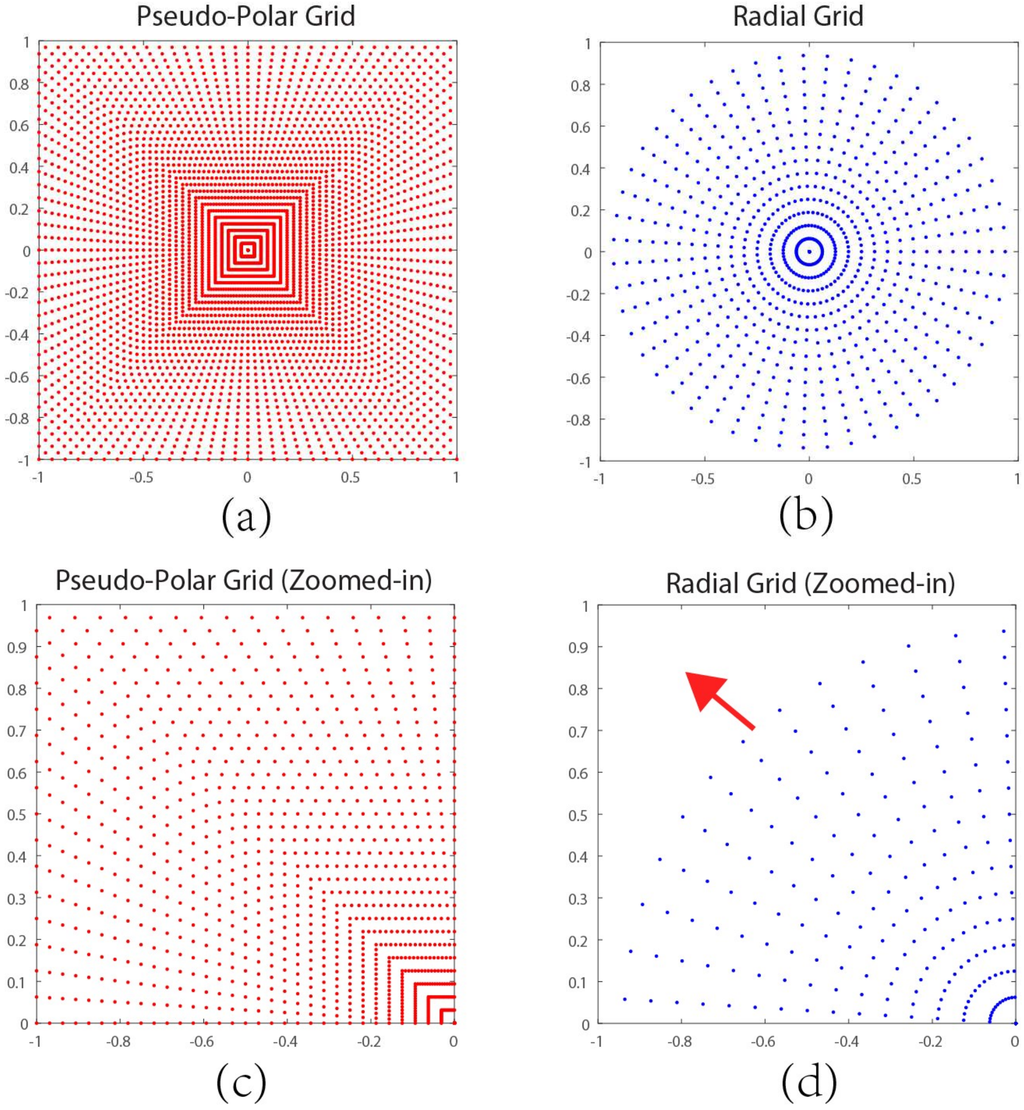

**Figure 5-2. Comparison of pseudo-polar and radial grids: The first row shows pseudo-polar grid (a) and radial grid (b) for the object MR image with 32 × 32 pixel. The second row displays the magnified part of pseudo-polar grid (c) and radial grid (d). The arrow in (d) illustrates the k-space coverage omission by radial grid.**

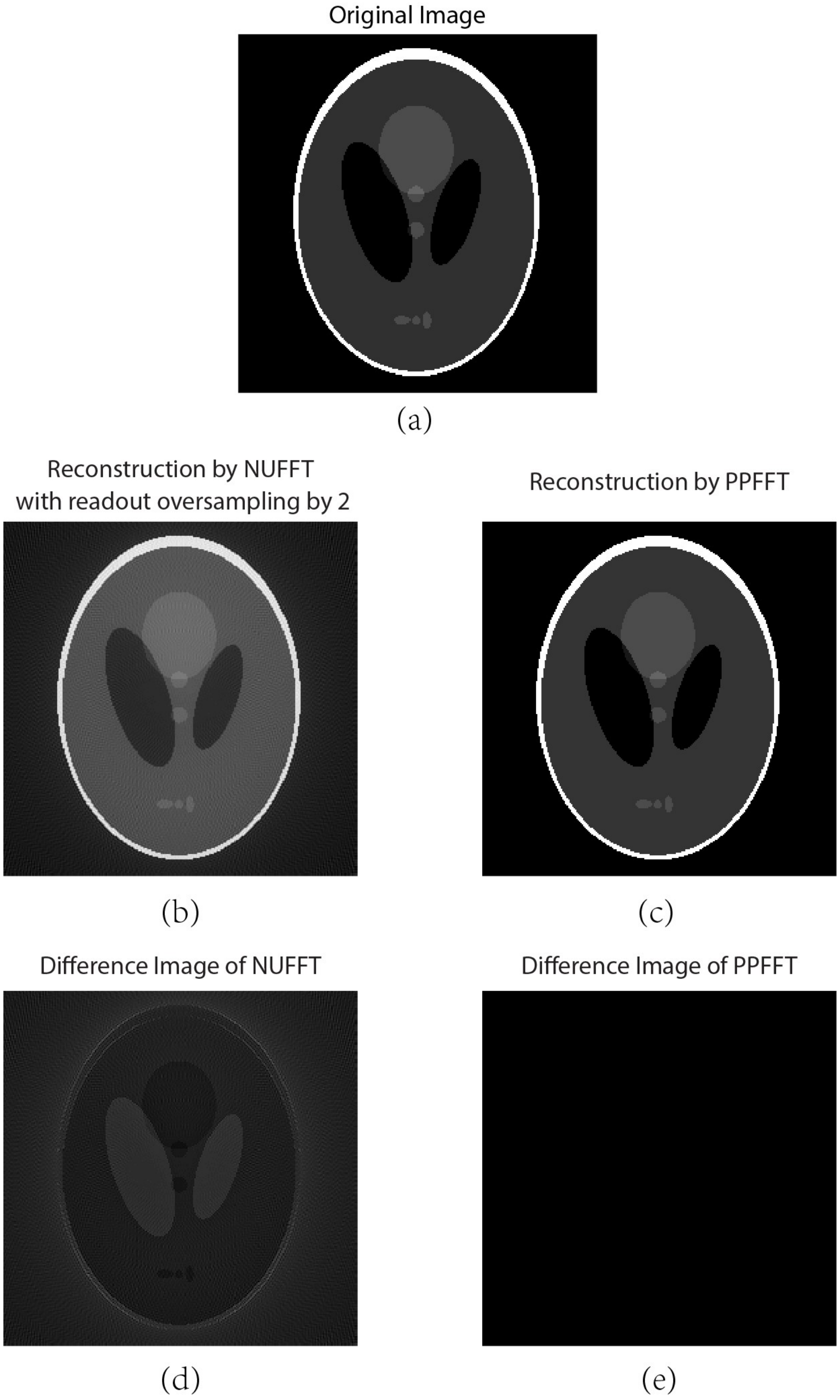

**Figure 5-3. Accuracy comparison of PPFFT and regridding method: (a) Original image; (b) Reconstructed image from radial *k*-space data through regridding; (c) Reconstructed image from Pseudo-Polar *k*-space data through inverse PPFFT; (d) The difference of original image and reconstructed one by regridding method; (e) The difference of original image and reconstructed one by PPFFT.**

### 5.2.4 Under-sampling pattern

The design of an under-sampling pattern is critical to the implementation of CS MRI, as it relates to the incoherence property that is essential for the image reconstruction. Using the equal-angle rays of radial trajectory and equal-slope rays of pseudo-polar trajectory, golden-angle under-sampling patterns [136, 137] and homogenous under-sampling patterns are performed. Here, in the cases with radial or pseudo-polar trajectories, the under-sampling rate or reduction factor (R) is defined as the ratio of one dimension of the image size (N) and the amount of sampled rays (S), i.e., R=N/S. For instance, the objective image size was 256×256. According to section C, the size of fully sampled *k*-space data of pseudo-polar trajectory was 512 rays with 512 points on each ray. Correspondingly, the size of fully sampled *k*-space data of radial trajectory was 402 rays with 256 points on each ray, according to the Nyquist-Shannon sampling theorem. When the reduction factor was set to be 6, there were $\frac{256}{6} \approx 43$ rays obtained for both trajectories. Figure 5-4(a) and Figure 5-4(b) illustrate the corresponding under-sampling patterns of these two trajectories.

The point spread function (PSF) was used here to evaluate the incoherence property of the two under-sampling patterns [137, 142, 143], as shown in Figure 5-4(c) and Figure 5-4(d). The incoherence is computed as the ratio of the main-lobe to the standard deviation of the side-lobes of PSF. The numerical incoherence results were 54.8 and 56.6 for the radial under-sampling pattern with a golden-angle scheme and pseudo-polar with a homogenous under-sampling, respectively. It demonstrates the performance of homogenous under-sampling pseudo-polar trajectory in incoherence properties.

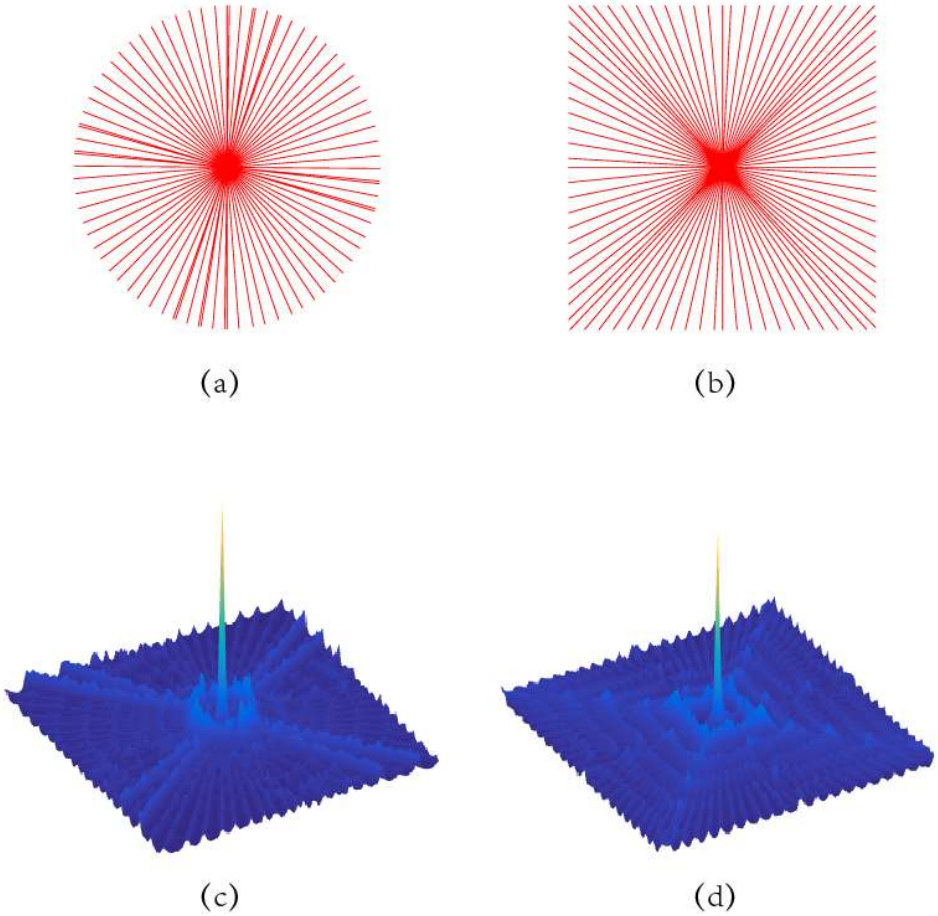

(a) (b)

(c) (d)

**Figure 5-4. Comparison of radial and pseudo-polar under-sampling pattern at R = 6. (a) Radial trajectory with golden-angle under-sampling scheme; (b) Pseudo-polar trajectory with homogenous under-sampling scheme; (c) The point spread function (PSF) of radial under-sampling pattern; (d) PSF of pseudo-polar under-sampling pattern.**

### 5.2.5 The proposed CS-MRI method

Based on the above described pseudo-polar framework, the CS MRI optimization is described as follows:

Suppose the object MR image I with N × N pixels, which can be represented sparsely in a mathematical basis Ψ. To reduce the data collection time, a subset of *k*-space data, y, is obtained using an under-sampling pattern P. Then the standard CS MRI reconstruction attempts to recover the full image data I through solving the following constrained optimization problem [8, 142, 143]:

$$\boldsymbol{Min} \quad \|\boldsymbol{\Psi}(\boldsymbol{x})\|_1 \qquad \boldsymbol{s.t.} \quad \|\boldsymbol{\emptyset}_{\boldsymbol{P}}(\boldsymbol{x}) - \boldsymbol{y}\|_2 < \boldsymbol{\varepsilon} \tag{5-10}$$

where $\boldsymbol{x}$ is the reconstructed $\mathrm{N} \times \mathrm{N}$-pixel image, $\|\cdot\|_1$ represents the $\ell_1$ norm defined as $\|\boldsymbol{x}\|_1 = \sum_{j=1}^{N} \sum_{i=1}^{N} |\mathrm{x_{ij}}|$ , $\boldsymbol{\Psi}$ means the sparse transform, $\emptyset_{\boldsymbol{P}}$ donates the FFT followed by an under-sampling pattern $\boldsymbol{P}$, $\boldsymbol{y} = \emptyset_{\boldsymbol{P}}(\boldsymbol{I})$ is the corresponding subset of the $k$-space measurements, ε controls the data fidelity of reconstruction depending on the selected $k$-space measurements $\boldsymbol{y}$.

With the pseudo-polar Fourier transform, the $\emptyset_{\boldsymbol{P}}$ operator in (5-10) is expressed as:

$$\emptyset_{\boldsymbol{P}} = (\boldsymbol{T}_{\mathrm{PP}}\boldsymbol{x}).* \boldsymbol{P}_{\mathrm{PP}} \tag{5–11}$$

where $\boldsymbol{P}_{\mathrm{PP}}$ is the under-sampling pattern, $\boldsymbol{T}_{\mathrm{PP}}$ is the PPFFT.

## 5.3 Methods and materials

### 5.3.1 Data acquisitions

The numerical validation of the proposed method is performed with using a Shepp-Logan image with 256×256 pixels. The two-fold oversampling in readout direction was applied on each radial ray, which avoided aliasing sidelobes [137, 141]. So the radial $k$-space consisted of 402 full-length rays, on which 512 points were sampled. The pseudo-polar $k$-space consisted of 512 full-length rays on which 512 points were sampled.

A LEGO phantom and a mouse were used to verify the performance of the proposed method experimentally. The experimental data acquisition was implemented by a 9.4 T Bruker Biospin MRI preclinical scanner (Ettlingen, Germany) with a birdcage volume radiofrequency coil of 40 mm in diameter. The LEGO phantom was constructed by inserting a piece of LEGO block into a cylindrical container ($\phi$ = 24 mm) filled with a water solution of NaCl (0.045 mol/L) and $NiSO_4 \cdot 6H_2O$ (0.005 mol/L). The mouse was anesthetized with isoflurane (1% - 2% in 1 L/min flow of medical grade oxygen) and was presented prone within the scanner.

The radial $k$-space data were acquired using ultra-short TE (UTE) sequence [144] with the following parameters: TR = 100ms, TE = 0.40ms, and matrix size 256×256. $B_0$ shimming was achieved by first measuring the $B_0$ map using a multi-echo sequence, and then calculating and applying the second-order shims. The fully sampled radial $k$-space data consisted of 804 half-length rays, on which 128 points were sampled in the readout direction. The total acquisition time was 80.4 s for this radial UTE sequence. In order to avoid the fold-over effect caused by regridding method, we set the FOV larger than the imaging subject instead of two-fold oversampling along the readout direction for radial trajectory [141].

The pseudo-polar sequence was modified from UTE sequence by replacing radial grid with pseudo-polar grid. In this study, we kept TR, TE and matrix size of pseudo-polar UTE the same as radial UTE; therefore, according to Section II.A, the fully sampled pseudo-polar k-space is a set of 1024 half-length rays, each of which consisted of 256 points with uniform distance in the readout direction. The acquisition time of the whole data was in 102.4 s.

The eddy currents and gradient imperfections led to deviations of the actual sampling trajectory from the theoretical one. The actual sampling locations in *k*-space were estimated using a vendor-supplied function (Paravision 6.0, Bruker Biospin) available to both radial and pseudo-polar trajectories. The deviation happened to both radial and pseudo-polar acquisitions, as illustrated in Figure 5-5, where theoretical trajectory is shown in red and the actual trajectory is shown in blue. As the deviations of theoretical sampling points and actual sampling points were not significant, a cubic interpolation was implemented to calibrate the raw *k*-space data points to the theoretical locations for both trajectories.

The golden-angle under-sampling pattern was applied to the radial trajectory in a retrospective fashion. Since the conventional radial rays do not coincide with golden angles, the acquired radial rays that were closest to the desired golden angles were selected to simulate golden angle acquisitions. The under-sampling was achieved in a straightforward fashion. Taking an image of 256×256 (corresponding to a fully-sampled *k*-space of 804 half-length radial rays) for example, the radial rays associated with the first 256, 128, 90, 64 and 52 golden angles corresponded to reduction factors of 2, 4, 6, 8 and 10 respectively.

The homogenous under-sampling pattern was implemented for the pseudo-polar trajectory by discarding the fully sampled *k*-space data. For a 256×256 image (corresponding to a fully sampled k-space of 1024 half-length pseudo-polar rays) with the same reduction factors as radial acquisition (i.e., 2, 4, 6, 8 and 10), 256, 128, 90, 64, 52 half-length pseudo-polar rays were included in the CS reconstruction. In such a way, with the under-sampling rate the number of acquisitions and hence the acquisition times are the same for both trajectories.

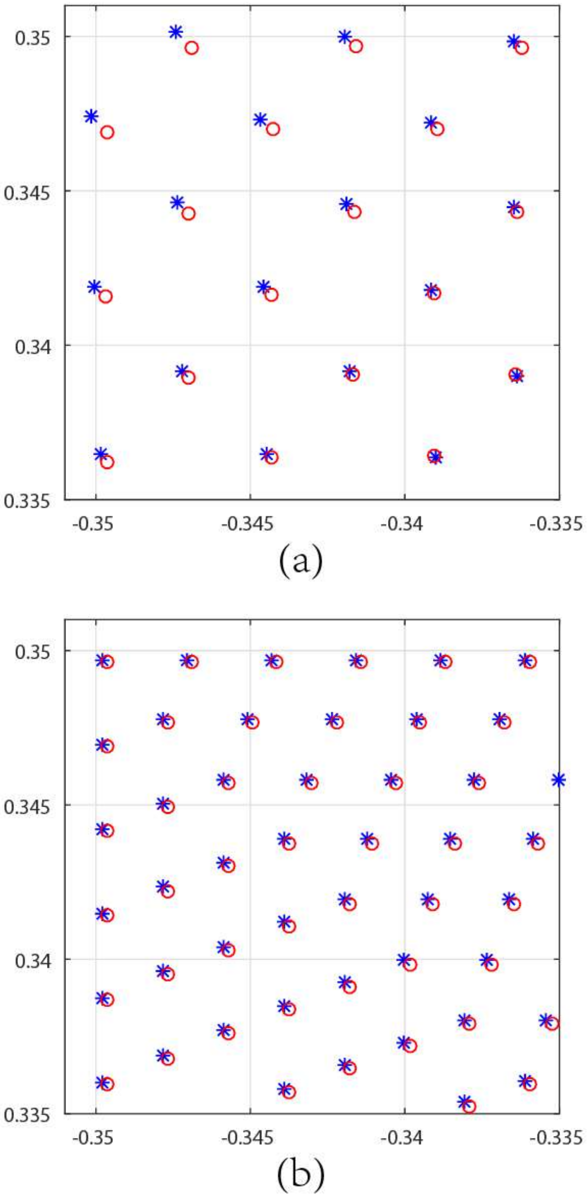

**Figure 5-5. The magnified version of radial trajectory (a) and pseudo-polar trajectory (b) with theoretical sampling points in red and actual sampling points in blue.**

### 5.3.2 CS reconstructions

All the above-mentioned reconstructions were implemented in Matlab (R2014b: The Mathworks, Natick, MA) on a personal computer with an Intel Core i7-3770 eight-core processor and 12GB of memory. During CS optimization, the constrained convex optimization problem expressed in (5-10) and (5-11) was re-organized into an unconstrained Lagrangian form [142, 143]:

$$\boldsymbol{Arg}\ \min_{\boldsymbol{x}}(\|(\boldsymbol{T}_{\mathbf{PP}}\boldsymbol{x}).*\ \boldsymbol{P}_{\mathbf{PP}}-\boldsymbol{y}\|_{\mathbf{2}}+\boldsymbol{\lambda}\|\boldsymbol{\Psi}(\boldsymbol{x})\|_{\mathbf{1}}) \tag{5-12}$$

where $\lambda$ donates the trade-off parameter between the data sparsity ($\ell_1$ norm) and consistency ($\ell_2$ norms). In this study, equation (12) was processed by the nonlinear conjugates and backtracking line-search methods proposed in [142, 143]. For comparison, the algorithm developed in [119] is referred to as the conventional CS method, which is based on a modified version of nonlinear conjugate gradient algorithm to solve the optimization problem and uses non-uniform FFT or NUFFT (instead of traditional Cartesian 2D-FFT) to transform data between radial *k*-space and image domain. Wavelet and total variation (TV) transforms are utilized as sparse transform in both methods to control the $\ell_1$ norm. The regularization parameters (Lagarangian multipliers for sparsity and TV terms) for both methods were tuned individually to achieve optimal reconstruction qualities. To quantitatively evaluate the reconstructed image quality of both CS MRI methods, PSNR (define as equation (3-5)) and SSIM (define as equation (4-5)) are introduced as performance metrics.

As *k*-space data were acquired using radial and pseudo-polar trajectories in the experiments, the fully sampled radial and pseudo-polar images were obtained and normalized as the reference for conventional and the proposed method respectively. For both conventional and the proposed methods, the differences between the reconstructed and fully sampled images were also qualitatively compared.

## 5.4 Results

### 5.4.1 Simulation

In this numerical simulation, we compared the reconstructed images of conventional and the proposed methods at the reduction factor of 6 (45 sampled rays from 402 fully sampled rays for radial trajectory and 512 fully sampled rays for pseudo-polar trajectory). The results are shown in Figure 5-6. Comparing the magnified parts in the reconstructions of the two methods (see Figure 5-6a and Figure 5-6b), we find that the proposed method recovered image details without blurring. When comparing the difference between the original and reconstructed images outlined in Figure 5-6(c) and Figure 5-

6(d), it is easy to see that the proposed method effectively eliminated the streaking artifacts and retained the sharp edges of the object (see arrows in Figure 5-6c and Figure 5-6d).

Figure 5-7 displays the PSNR and SSIM values as a function of reduction factors. Both curves show that the proposed method had a stable improvement at all the reduction factors under consideration. Compared with the conventional CS approach, the new method obtained at about 5dB PSNR increase whilst it still kept the SSIM value above 0.8, particularly when R = 2, 4 or 6.

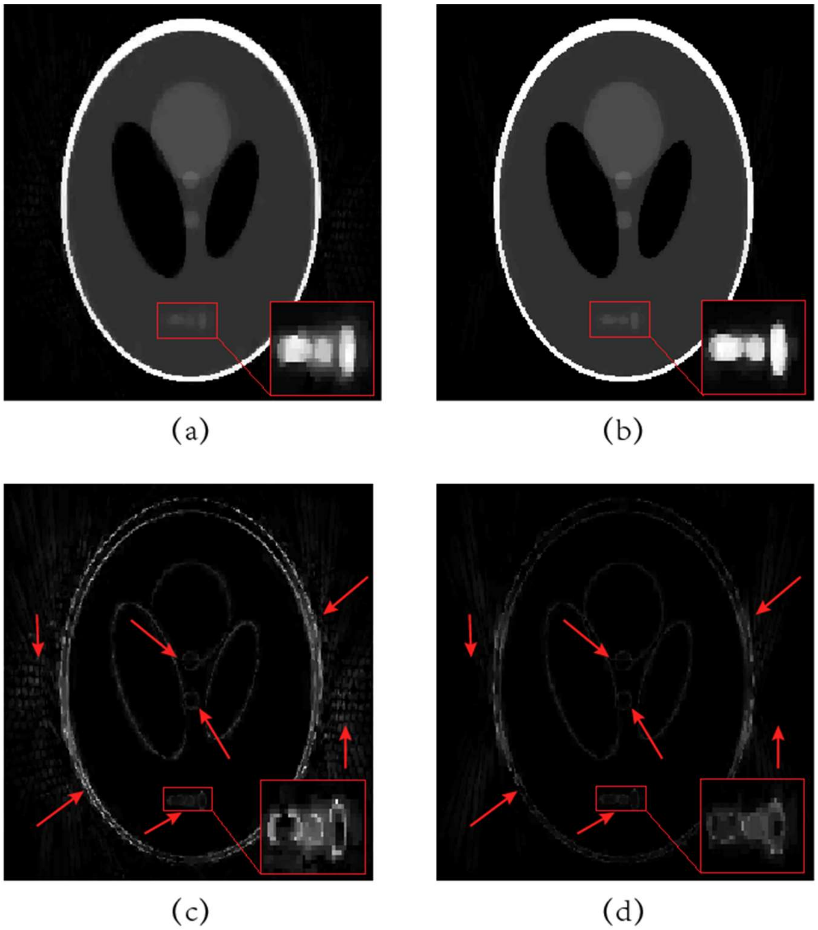

(a) (b)

(c) (d)

**Figure 5-6. Reconstructed images of Shepp-Logan phantom (top row) and difference images (bottom row) at R = 6. From left to right applied algorithms are: conventional and proposed methods. The contrast of magnified parts in (a) and (b) is normalized with the maximum values of them. The magnified parts in (c) and (d) are processed in the same way.**

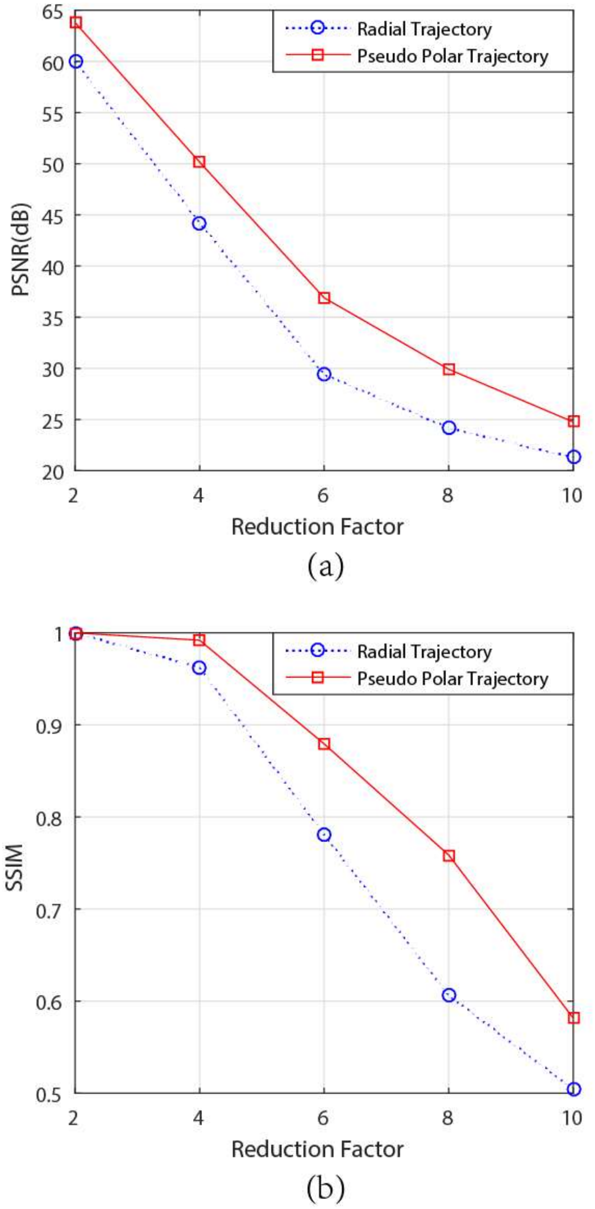

**Figure 5-7. PSNR (a) and SSIM (b) curves vs. various reduction factors. In this study, the CS reconstruction of under-sampled Shepp-Logan phantom data was considered. It can be seen that the proposed method achieved higher PSNR and SSIM values compared with conventional NUFFT based CS methods.**

### 5.4.2 LEGO phantom results

A LEGO phantom was used to acquire radial and pseudo-polar *k*-space data. The fully sampled *k*-space datasets with both trajectories were used as references (see Figure 5-8a and Figure 5-8b) in the respective accelerated case. Images in Figure 5-8 illustrated the performance of the two methods with 64 rays (R = 4) of *k*-space data. Compared with the original image from fully sampled radial *k*-space data (see Figure 5-8a), the streaking artefacts introduced by under-sampling was evident in the image reconstructed by the conventional method, especially near sharp edges (marked with red arrows in Figure 5-8c). In contrast, the proposed method eliminated these under-sampling artefacts when comparing the original image (see Figure 5-8b) and reconstructed image (see Figure 5-8d) from pseudo-polar *k*-space data. Comparing Figure 5-8(e) and Figure 5-8(f), the difference in images produced by the two methods demonstrates the improved accuracy of the proposed method. The errors near the border between the background and object were obvious in the conventional method as shown in Figure 5-8(e). The max error in the image reconstructed by the proposed method was 0.1116, which was less than half of that of the conventional method (0.2642).

Figure 5-9 displays the PSNR and SSIM values as a function of reduction factor. As the LEGO phantom with sharp edges and strong contrast, the proposed method had at least 5dB improvements in PSNR compared to a conventional method. At a very high reduction factor (R=10), the SSIM of reconstructed images with the proposed method was still kept up to 0.95, significantly higher than that of the conventional method with R=4.

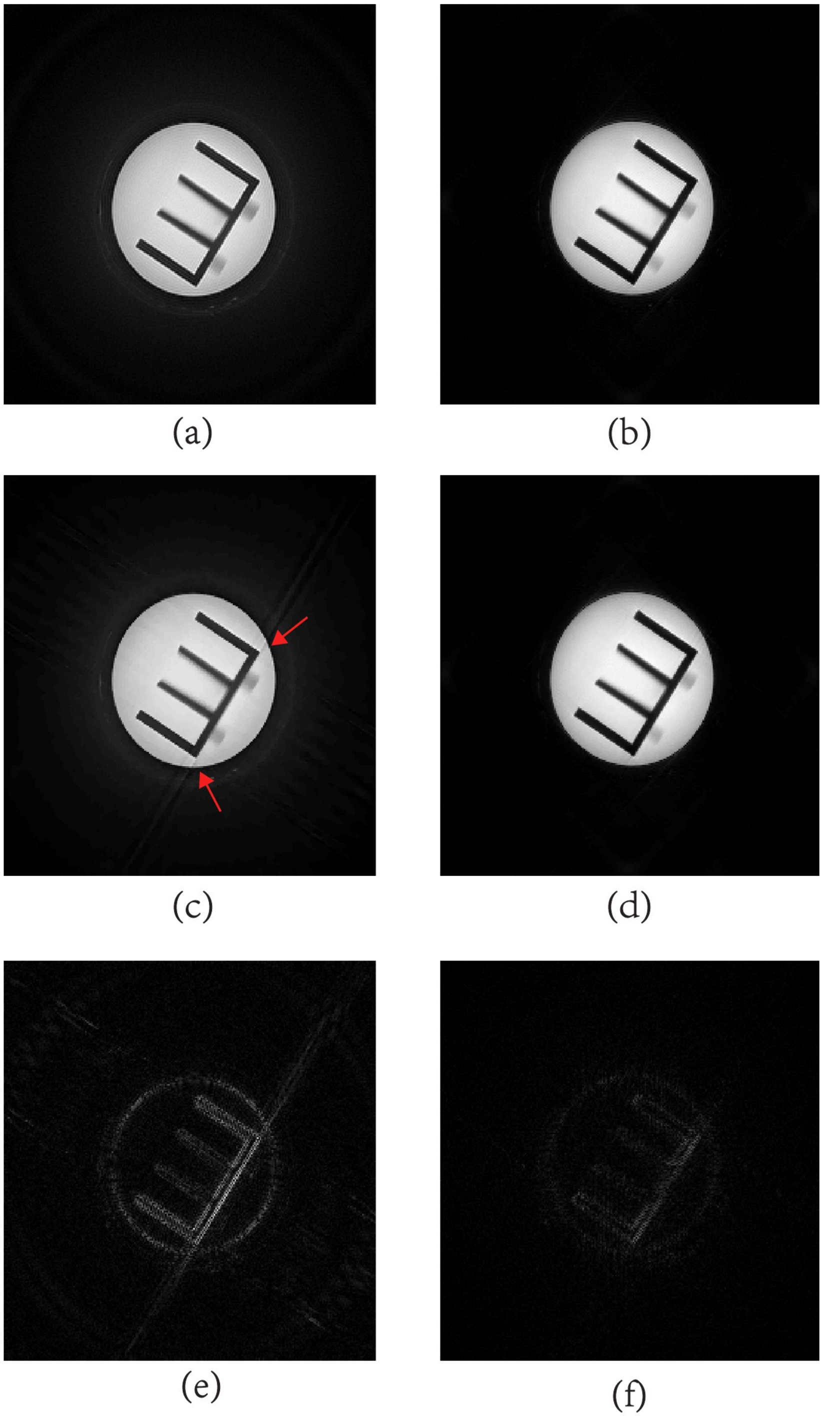

(a) (b) (c) (d) (e) (f)

**Figure 5-8. Reconstructed images of Shepp-Logan phantom (top row) and difference images (bottom row) at R = 6. From left to right applied algorithms are: conventional and proposed methods. The contrast of magnified parts in (a) and (b) is normalized with the maximum values of them. The magnified parts in (c) and (d) are processed in the same way.**

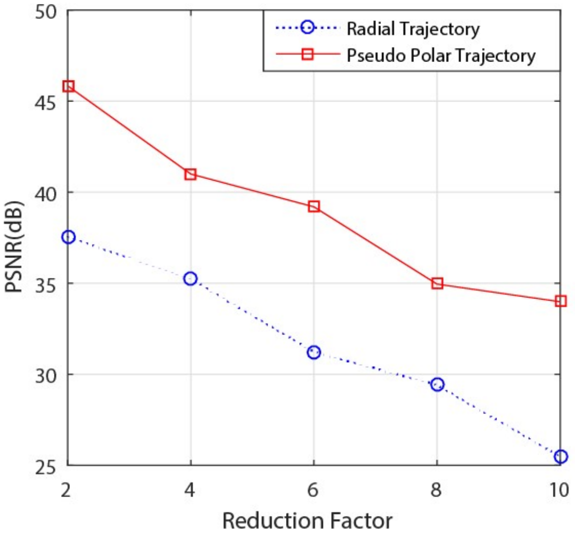

(a)

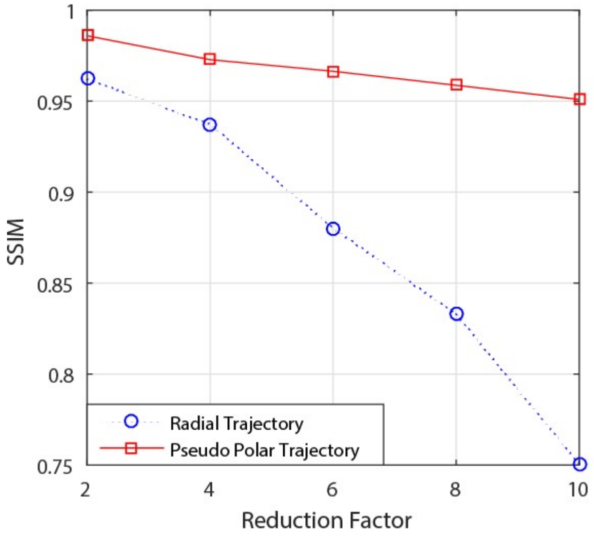

(b)

**Figure 5-9. PSNR (a) and SSIM (b) curves vs. various reduction factors. In this study, the CS reconstructions of under-sampled LEGO phantom data from radial and pseudo-polar trajectories were considered.**

### 5.4.3 In vivo experiment results

A live mouse was used to acquire radial and pseudo-polar *k*-space data for head imaging. Due to a slight mismatching in the imaging slice, the radial and pseudo-polar images had different appearances shown as  Figure 5-10(a) and Figure 5-10(b) respectively.

In Figure 5-10, the reconstructions with 64 *k*-space rays (R = 4) from the radial and pseudo-polar trajectories were selected as a case for study. Overall, both methods acquired good quality images. Compared with the reconstruction by the proposed method (see Figure 5-10d), there were some streaking artefacts in the conventional method, illustrated by the arrow in Figure 5-10(c). Meanwhile, Pseudo-Polar trajectory effectively suppressed these under-sampling artefacts. To the reconstruction accuracy of the two methods, the difference in images is shown in Figure 5-10(e) and Figure 5-10(f). Noticeably, the proposed method provided higher reconstruction accuracy, especially regarding the edges and details. The max reconstruction errors were 0.1565 and 0.1514 for conventional and the proposed methods respectively.

Figure 5-11 depicts the magnified version of images shown in Figure 5-10 for detailed analysis.  For the conventional method, Figure 5-11(a) and Figure 5-11(c) show some structure losses (illustrated by the arrows) in the reconstructed image when compared to the original image. In comparison, the proposed method showed better reconstruction performance with finely maintained structures and sharpness, indicated by the arrows in Figure 5-11(b) and Figure 5-11(d).

As depicted in Figure 5-12, the improvement of the proposed method was stable at different reduction factors, where the PSNR value was higher than the radial-sampled counterpart by over 2dB and the SSIM value was kept over 0.88.

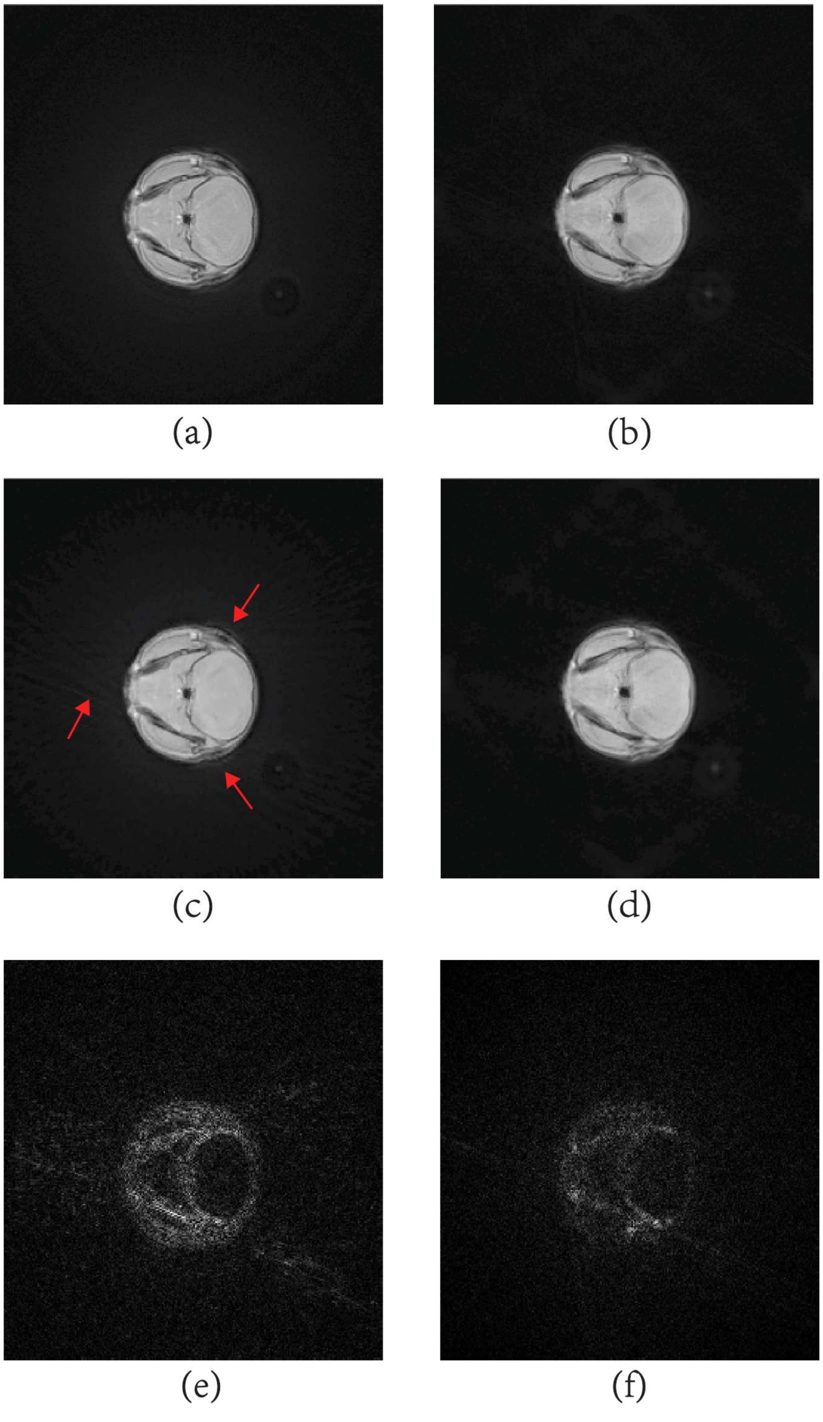

**Figure 5-10. The performance comparison of two methods in in vivo mouse head imaging with 64 rays of *k*-space data (R = 4). (a) Original image from fully sampled radial data. (b) Original image from fully sampled pseudo-polar data. (c) Reconstructed image by conventional method from under-sampled radial data. (d) Reconstructed image by proposed method from under-sampled pseudo-polar data. (e) Difference image of conventional method. (f) Difference image of proposed method.**

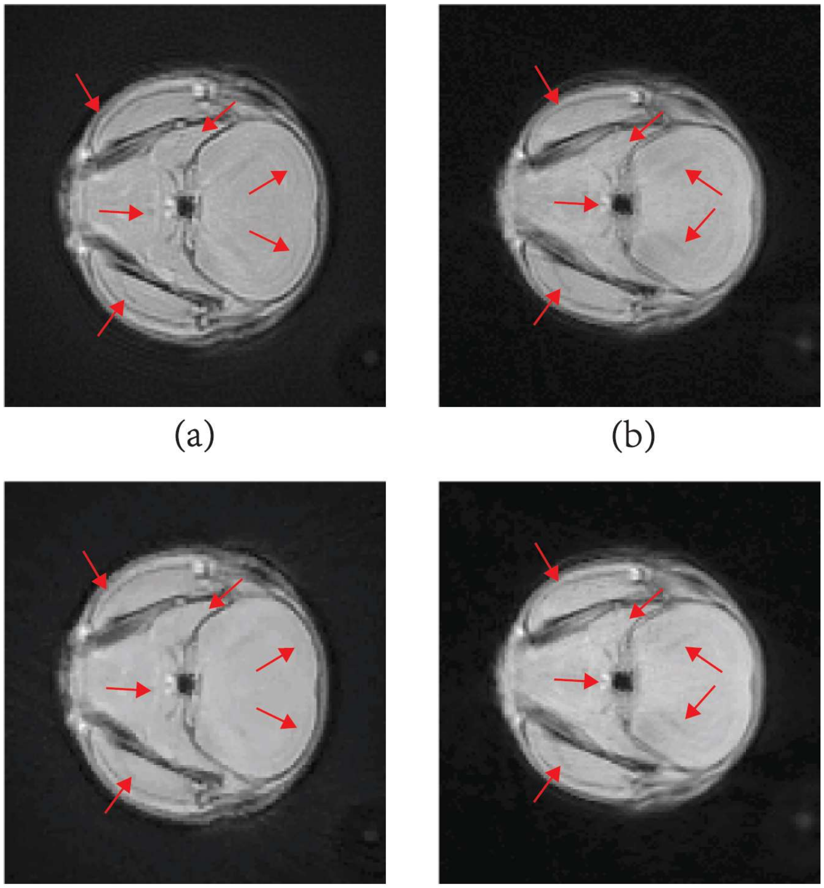

(a) (b)

(c) (d)

**Figure 5-11. Magnified versions of images in Fig. 10. (a) Original image from fully sampled radial data. (b) Original image from fully sampled pseudo-polar data. (c) Reconstructed image by conventional method from under-sampled radial data. (d) Reconstructed image by proposed method from under-sampled pseudo-polar data.**

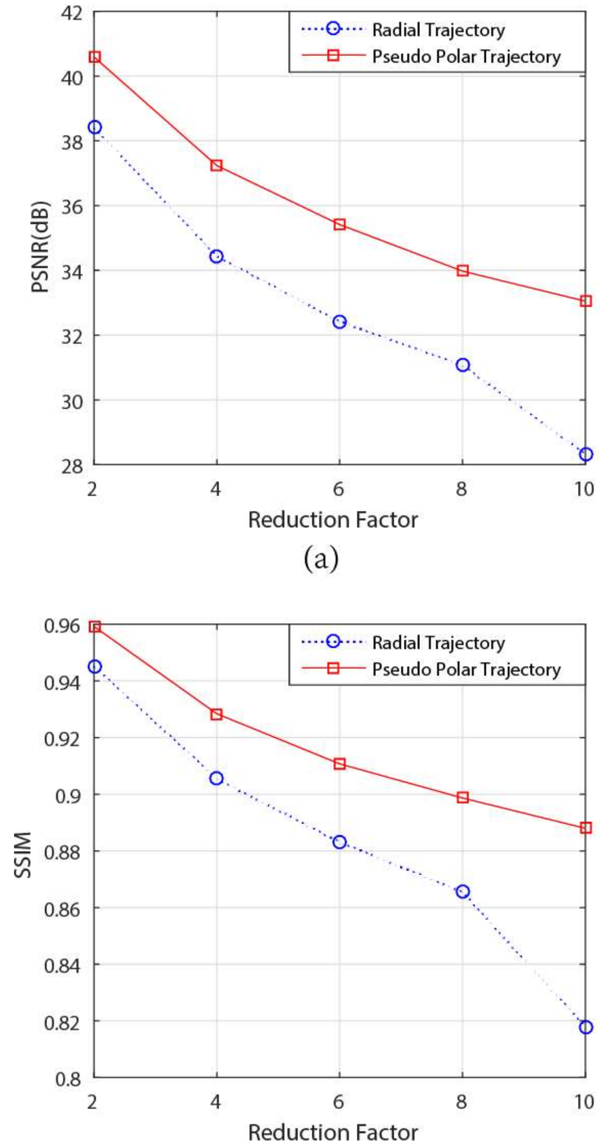

(a)

(b)

**Figure 5-12. PSNR (a) and SSIM (b) curves vs. various reduction factors. In this study, the CS reconstruction of under-sampled in vivo mouse head imaging was considered.**

## 5.5 Discussion

### 5.5.1 Reconstruction quality improvement

In this study, we have proposed a method that uses pseudo-polar trajectories for CS-MRI. This method avoids the iterative procedure of regridding and inverse regridding involved in the traditional non-Cartesian CS-MRI reconstruction method. A Shepp-Logan phantom, LEGO phantom and an in vivo mouse sample were used to demonstrate the performance of the proposed method in relation to image detail preservation and streaking artifacts suppression. The results clearly demonstrate that the combination of the new sampling trajectory and CS reconstruction outperforms that of the conventional CS implementation with the radial trajectory and regridding.

Similar to the standard radial trajectory, the pseudo-polar trajectory inherits characteristics of low sensitivity to motion. Also, with superior incoherence property, the pseudo-polar under-sampling pattern leads to streaking artifacts of lower intensities than that of the radial trajectory. In terms of *k*-space coverage of these two trajectories (see Figure 5-2a and Figure 5-2b), pseudo-polar trajectory acquires more high-frequency regions of *k*-space. The additional high-frequency *k*-space coverage leads to a better result in image detail and sharp edge preservation. Moreover, the pseudo-polar trajectories enable the applications of PPFFT in the proposed reconstruction algorithm, which avoids the regridding and inverse regridding operations (lossy interpolations) as typically done in each iteration of the radial CS reconstruction. The advantages of the pseudo-polar CS reconstruction are evidenced by the simulation and experimental data ( Figure 5-6 ~ Figure 5-12).

### 5.5.2 Computational cost

Compared with Cartesian CS method, the proposed method involves an iterative inverse PPFFT operation, which increases the computation burden. To robustly achieve good quality reconstructions, we set the max iteration time as 10 and error tolerance as $10^{-7}$ for the inverse PPFFT implementation. In the given studies with the image size of 256×256, the average computation times of the Cartesian CS method and proposed method were 15.5 seconds and 198.5 seconds, respectively. For imaging applications requiring real-time reconstructions, the computational efficiency can be improved by implementing the reconstruction software in more efficient platforms, such as C language, instead of the MATLAB scripts currently used.

### 5.5.3 Limitations of the proposed method

The successful implementation of the proposed method requires a high accuracy *k*-space sampling. Because of the eddy current issue in MRI, the actual sampling trajectory may deviate from the designed trajectory, leading to inaccuracy in signal collection. A calibration method for the *k*-space sampling is currently in progress, which aims to improve the performance and robustness of the proposed method.

## 5.6 Conclusion

In this Chapter, we have presented a novel rapid MR imaging method that combines the pseudo-polar *k*-space trajectory and CS. The proposed method takes advantage of the high efficiency of the fast pseudo-polar Fourier transform, thus avoiding repeated regridding/inverse-regridding operations that result in interpolation errors in cases of standard radial *k*-space trajectory. The results from the simulation and imaging experiments demonstrate that the new method effectively improves the reconstructed image quality at various reduction factors. In further work, the proposed method will be refined and used in dynamic imaging applications.

# 6. Conclusion

As described in Chapter 2, the imaging speed of traditional MRI is inherently limited by collecting data sequentially using gradient encoding. To reduce the scan time of MRI, high-speed imaging techniques like FSE and EPI, and parallel imaging techniques such as GRAPPA and SENSE have been proposed and implemented. However, the current techniques for acceleration still cannot fully meet the imaging requirements in some situations such as cardiac, perfusion and functional MRI to image dynamic phenomena with higher spatial and temporal resolution. Theoretically sound, CS is a breakthrough in MRI acceleration technique. The sub-sampling in data collection can directly shorten the scan time and faithful image reconstruction can be obtained from the sub-sampled *k*-space data using optimisation algorithms. Nevertheless, looking at the application of CS in MRI, some theoretical conditions are not feasible in practise, for example the truly random point *k*-space sampling trajectory required by CS is impractical in current MRI systems. The compromise in the realization of this degrades the quality of reconstructed images and obstructs the further applications of CS MRI.

This thesis presents a series of original research (Chapters 3-5) with the intention to improve the image reconstruction quality of CS MRI. In this chapter, the contribution of the thesis is summed up and the implications of the research are presented. Then, a discussion of the limitations of the current research is provided and the chapter concludes with an overview of planned future work related to improvements and extensions to the current solutions.

## 6.1 Thesis contributions and implications

### 6.1.1 Compressed Sensing MRI via two-stage reconstruction (Chapter 3)

A novel, two-stage reconstruction scheme was introduced to avoid the deterioration in image quality of MR images reconstructed by CS at high reduction factors. As it is known that energy of most images is concentrated in and around the central region of *k*-space origin, the approach applied a segmentation strategy to take advantage of the non-uniform distribution of *k*-space information. In contrast to other methods that segment data in the sparsity domain such as the wavelet domain, this novel approach is the first to segment data in the *k*-space domain. An original metric, *k*-space power ratio, was introduced here to decide the boundary of segmentation. Applying different optimization parameters to the segmented areas, the non-uniform distribution of *k*-space information can be used to facilitate the CS reconstruction close to ideal conditions. To assess the performance, cardiac cine, sagittal brain MR and angiogram imaging were selected for clinical research. Compared with a conventional CS reconstruction, the proposed method achieved a better reconstruction with a 2 ~ 4dB peak signal-to-noise ratio improvement, while the reduction factor was up to 6.

### 6.1.2 Aliasing Artefact Suppression in Compressed Sensing MRI for Random Phase-encode Under-sampling (Chapter 4)

The feasibility of a novel method was investigated to suppress the aliasing artefacts by exploiting the random phase-encode under-sampling pattern in CS MRI. In this method, a new strategy, which splits the traditional 2D image reconstruction problem into a series of 1D signal reconstruction problems, was first bought up to reduce the mutual coherence between the adjacent columns of under-sampled *k*-space data acquired using a random phase-encode pattern. In each 1D signal reconstruction problem, the 1D randomness in the phase-encode under-sampling pattern can be put to best use to cut down the aliasing artefacts in the 2D image reconstruction. The performance of the proposed method was evaluated by various cases of typical MR images including cardiac cine, brain, foot and angiogram with the reduction factor up to 10. Compared to conventional methods that use a modified version of the nonlinear conjugate gradient algorithm to solve whole image reconstruction problem, the new method achieves more accurate reconstruction results with a 2~5dB gain in PSNR and a higher SSIM. Experiments using the proposed method demonstrated faithful reconstruction of the MR image and suppression of the coherent artefacts introduced by the random phase-encode under-sampling.

### 6.1.3 Pseudo-Polar Fourier Transform based Compressed Sensing MRI (Chapter 5)

In order to avoid the weak incoherence of a Cartesian trajectory in CS MRI, a non-Cartesian trajectory, a pseudo-polar trajectory and the relative transform (PPFFT) were applied to combine with CS in the proposed method. Compared with conventional Cartesian trajectories, the radially sampled *k*-space data by pseudo-polar trajectory are more incoherent and more data are collected from the central *k*-space region. These properties are very suitable for CS based fast imaging. Meanwhile, the transformation of pseudo-polar sampled *k*-space data into the image domain was realized through pseudo-polar FFT, which is based on the standard 1D FFT and the FRFT. This effective and accurate way of transformation makes it superior to the radial *k*-space trajectory, which is also a non-Cartesian trajectory and has drawn strong interest from researchers for its potential in developing fast imaging methods in MRI. To evaluate the performance of the proposed method, both simulated and experimental data are used to compare the new method with conventional approaches. Compared with the conventional radial sampling based CS-MRI methods, the proposed method achieves greater than 2 dB gain in PSNR and keeps the SSIM over 0.88 in different situations of simulation and in vivo experiments. The performance demonstrated the proposed method achieved a more accurate reconstruction with respect to image detail/edge preservation and artefact suppression than conventional approaches. The successful implementation of the non-Cartesian trajectory based scheme provides a practical way of implementing CS MRI to get accurate and faithful image reconstruction for clinical applications.

### 6.1.4 Implications

This research has presented a number of original and creative methods for improving the reconstruction quality of CS MRI. The majority of current studies in CS MRI focus on improving the performance of the CS algorithm  by finding more suitable sparsity transform, designing more incoherent under-sampling patterns and using more efficient optimization. This thesis presented a series of methods from another perspective to achieve more accurate reconstruction by exploiting the properties of MRI *k*-space data when combined with CS. Using iterative (Chapter 3) and split (Chapter 4) reconstruction strategies, and a novel acquisition trajectory (Chapter 5) approach all demonstrate an increase in performance in faithful image reconstructions. These novel approaches have significant potentials when merged with existing research focusing on the transform sparsity or optimization algorithms of CS. These proposed methods are likely to contribute positively to clinical feasibility of CS MRI and provide better opportunities to further implement CS MRI in dynamic imaging and rapid imaging.

## 6.2 Limitations

### 6.2.1 Computational complexity

A common limitation of the proposed methods in Chapter 3 and 4 is the increased computational cost compared to the conventional methods based on a nonlinear optimization, which has already been shown to be time consuming. The segmenting process of the method in Chapter 3 separated the whole image reconstruction of the conventional method into two stages. The extra central *k*-space data reconstruction in the first stage does obtain a faithful reconstruction of image outline, which provides more information for the whole image reconstruction. However, the accompanying iterative optimization in this stage increases the computation burden.

Regarding the approach in Chapter 4, the series of 1D signal reconstructions separated from the 2D image reconstruction took full advantages of the 1D incoherence of the random phase-encode under-sampling pattern to fit the requirement of incoherence in CS. However, the corresponding cost was the additional optimizing operations, which caused an increase in computational complexity.

The PPFFT in Chapter 5 is more efficient than the traditional regridding and inverse-regridding method when realizing the transform between the non-Cartesian *k*-space data and the reconstructed image. However, the inverse PPFFT process still poses a difficulty in its calculation as it is realized by an iterative optimization method. The different settings of maximum iteration number for various situations can cause uncertainty in computing time. And error tolerance in this iteratively refined algorithm may also make it time consuming, especially if this threshold is set to an infinitesimal value. It is expected that the inverse transform can be further improved with more effective or non-iterative optimizations.

### 6.2.2 Data accuracy

By using a pseudo-polar trajectory and a pseudo-polar fast Fourier transform, the method developed in Chapter 5 reconstructed images with detail preservation. However, the quality of the reconstruction does not only depend on the recovery method. The accuracy of the *k*-space sampling is also an important element affecting the final reconstructed result. In practice, the eddy current effects induced by gradient switching can cause trajectory deviation from the designed trajectory. The deviation leads to inaccurate signal collection and degrades the reconstructed image quality. The problem is prominent when applying a non-Cartesian sampling trajectory like a pseudo-polar trajectory. Because the inverse pseudo-polar fast Fourier transform is based on an iterative algorithm, the initial error introduced by the trajectory deviation will be magnified after several iterations and degrade the quality of the transformed images. A simple data calibration algorithm was implemented to post-correct the data in Chapter 5, but this could also influence reconstruction accuracy. It is hoped that data accuracy can be improved by resorting to a more optimized data calibration algorithm and advanced hardware platforms.

## 6.3 Future work

Future work will mainly focus on improvement to existing solutions and extending the applications of the current work. Specifically, the image reconstruction schemes developed in Chapter 3 and Chapter 4 could achieve better performance with a more efficient sparsity transform and an improved optimization algorithm. With the spread of GPU accelerated computing, taking advantage of upgraded hardware would mean that the series of 1D parallel signal reconstructions in the proposed method (see Chapter 4) could be computed simultaneously to shorten the processing time. The approach based on a PP trajectory and PPFFT could be developed for dynamic imaging for its low motion sensitivity.

### 6.3.1 Improvement to current solutions

In this thesis, the classic wavelet sparsity transform and the standard CG optimization algorithm are still used in the proposed methods. Recently, the CS theory has been considerably improved and can be used to further promote the reconstructed image quality of CS MRI. For example, the novel sparsity bases in CS [79, 80, 92, 99] have the potential in to provide optimal sparse representation of objects to retain more details with the same number of samples. In the static CS MRI, shearlet and curvelet [146, 147] sparsity transforms can preserve the edges and features in image reconstruction because of the excellent directional selectivity and localization property. In addition to these 2D sparsity transforms, a series of high-order sparsity transforms like 3D wavelet transform [148], 3D shearlet transform [149] and HOSVD [80] can exploit the tensor sparsity in the 3D or 4D dataset. They are demonstrated to be useful in dynamic MRI in terms of image reconstruction accuracy and sparsifying efficiency. On the other hand, several kinds of algorithms have also been proposed for CS to faithfully reconstruct the sparse signals from a small number of linear measurements. For example, the iteratively reweighted least squares (IRLS) performed $l_p$-norm ($p < 1$) minimization to approximate the ideal $l_0$-norm minimization in CS [150]. And the Fast Iterative Soft Thresholding Algorithm (FISTA) [152, 153] is proposed to achieve fast convergence of image reconstruction by first order methods. Another proposed method [153] split the hard composite regulation problem in CS into sub problems, which reduces the computational complexity in the image reconstruction. Combining all of these advanced sparsity transforms and optimization algorithm, the proposed methods in this thesis will be used to greater advantage in making CS MRI practical for routine clinical use.

The split reconstruction strategy of the method in Chapter 4 successfully eliminates the aliasing artefacts introduced by the weak incoherence of the random phase-encode under-sampling pattern. To handle the consequent series 1D signal reconstructions, our next step is to investigate the GPU parallel acceleration to optimise the computational time. In contrast to a CPU which consists of a few cores optimised for sequential serial processing, GPU has thousands of smaller and more efficient cores designed to handle multiple tasks simultaneously in a massively parallel architecture. As the series 1D signal reconstructions in the proposed method are computationally independent, the GPU-accelerated computing offers the parallel 1D signal reconstructing processes to break the limitation of computational complexity. Furthermore, the proposed method can also be considered as a novel initialization method of CS.  The relationship between the initial solution and final reconstruction needs to be elaborated in theory as one part of our future work.

As mentioned in section 5.5.2, the proposed method in Chapter 5 involves an iterative inverse PPFFT operation, which brings extra computation burden. As equation (5-8) illustrated, the minimization problem might be solved by recursive least squares approach to improve the convergence. It can also avoid the difficulty in choosing the matrix D in equation (5-9) for more accurate reconstruction.

### 6.3.2 The extension of current work for wider applications

Chapter 3 proposed a two-stage reconstruction to take advantage of the non-uniform energy distribution of the *k*-space in the application of CS to static MRI. Extending to dynamic MRI, the segmentation strategy in the proposed method can further exploit the non-uniform *k*-space information as the cross section of the 3D under-sampling lines can be really disturbed in various densities according to the energy distribution. With sufficient base SNR and data sparsity, the performance of the proposed method in dynamic imaging will be investigated in the future.

In Chapter 4, the decomposition of 2D image reconstruction in the proposed method eliminates the aliasing artefacts from the random phase-encode sampling pattern in CS MRI. This strategy can also be extended into the combination of CS and parallel MR imaging to obtain higher accelerations [154]. Theoretically, with the faithful CS reconstruction using the proposed method, the following parallel imaging reconstruction can effectively reduce the overlap by the regular under-sampling to avoid the combined error in the final reconstructed image. In the near future, we are going to test this combined rapid imaging method for real time imaging such as tumour tracking in MRI-linac applications.

Chapter 5 described a novel method of combining a radial-like trajectory and CS, which was able to improve the accuracy and efficiency of applying non-Cartesian sampling in CS MRI. It is well known that a radial trajectory has great potential in abdominal and cardiovascular imaging for its immunity to subject motion. Inheriting similar properties to the radial trajectory, the pseudo-polar trajectory was shown to have favourable off-resonance behaviour and low average specific absorption rate (SAR), which are advantageous in ultra-high field MRI [155]. Considering the motion-robustness and SAR performance, the investigation of the proposed method in the ultra-high field MRI and dynamic imaging will be included in future studies.

# References

[1] P. Mansfield, A. A. Maudsley, and T. Bains, “Fast scan proton density imaging by NMR,” Journal of Physics E: Scientific Instruments, vol. 9, p. 271, 1976.

[2] P. van der Meulen, J.P. Groen, and J.J.M. Cuppen, “Very fast MR imaging by field echoes and small angle excitation,” Magn Reson Imaging, vol. 3, pp. 297-9, 1985.

[3] J. Listerud, S. Einstein, E. Outwater, and HY. Kressel, “First principles of fast spin echo,”Magn Reson Q, vol. 8, pp. 199-244, Dec 1992.

[4] K. P. Pruessmann, M. Weiger, B. Scheidegger, and P. Boesiger, “SENSE: Sensitivity encoding for fast MRI,” Magnetic Resonance in Medicine, vol. 42, pp. 952-962, 1999.

[5] K. P. Pruessmann, M. Weiger, B. Scheidegger, and P. Boesiger, “Advances in sensitivity encoding with arbitrary k-space trajectories,” Magn Reson Med, vol. 46, pp. 638-51, Oct 2001.

[6] M. A. Griswold, P. M. Jakob, R. M. Heidemann, M. Nittka, V. Jellus, J. Wang, B. Kiefer, and A. Hasse, "Generalized autocalibrating partially parallel acquisitions (GRAPPA)," Magnetic Resonance in Medicine, vol. 47, pp. 1202-1210, 2002.

[7] D. Donoho, “Compressed sensing,” IEEE Trans. Inform. Theory, vol. 52, no. 4,pp. 1289–1306, 2006.

[8] M. Lustig, D. Donoho and J. M. Pauly, “Sparse MRI: The application of compressed sensing for rapid MR imaging,” Magnetic Resonance in Medicine, vol. 58, pp. 1182-1195, 2007.

[9] M. Lustig, D. Donoho, J.M. Santos and J. M. Pauly, “A look at how CS can improve on current imaging techniques,” IEEE Signal Processing Magazine, vol. 24, no. 2, pp. 72 – 82, 2008.

[10] E. Candès, J. Romberg, and T. Tao, “Robust uncertainty principles: Exact signal reconstruction from highly incomplete frequency information,” IEEE Trans. Inform. Theory, vol. 52, no. 2, pp. 489–509, 2006.

[11] S. Qaisar, R.M. Bilal, W. Iqbal, M. Naureen, and L. Sungyoung, “Compressive sensing: From theory to applications, a survey,” Communications and Networks, Journal of , vol.15, no.5, pp.443,456,Oct.2013doi: 10.1109/JCN.2013.000083

[12] Bloch F. “The principle of nuclear induction,” Nobel Lecture 1952, pp. 203-215.

[13] P. C. Lauterbur, “Image Formation by Induced Local Interactions: Examples Employing Nuclear Magnetic Resonance,” Nature, vol. 242, pp. 190-191, 1973.

[14] P. Mansfield and A. A. Maudsley, “Medical imaging by NMR,” The British Journal of Radiology, vol. 50, pp. 188–194, 1977.

[15] P. Mansfield, “Multi-planar image formation using NMR spin echoes,” Journal of Physics C: Solid State Physics, vol. 10, p. L55, 1977.

[16] P. Rinck. (2014). Magnetic Resonance in Medicine. The Basic Textbook of the European Magnetic Resonance Forum, 8th.

[17] Z.P. Liang and P. C. Lauterbur. Principles of Magnetic Resonance Imaging: A signal Processing Perspective, 2000.

[18] J. Hennig, A. Nauerth, and H. Friedburg, ”RARE imaging - a fast imaging method for clinical MR,” Magn. Reson. Med., vol. 3, pp. 823–833.

[19] MT. Walker, S. Partovi, JP. Karis, FK. Fram, “Fast, versatile, and cost-effective FSE MR imaging: technical considerations and clinical applications,” Barrow Quarterly, vol. 16, pp. 1-5, 2000.

[20] DA. Feinberg, JD. Hale, JC. Watts et al, “Halving MR imaging time by conjugation: demonstration at 3.5 kG,” Radiology, vol. 161, pp. 527–531, 1986.

[21] P. B. Roemer, W. A. Edelstein, C. E. Hayes, S. P. Souza, and O. M. Mueller, “The NMR phased array,” Magnetic Resonance in Medicine, vol. 16, pp. 192–225, 1990.

[22] A.Deshmane, V. Gulani, M. A. Griswold, and N. Seiberlich, ”Parallel MR imaging,” *Journal of Magnetic Resonance*, vol. 36, pp. 55-72, 2012.

[23] JF.Glockner, H.H. Hu, DW. Stanley et al, “Parallel MR imaging: a user's guide,” Radiographics, vol. 25, pp. 1279–1297, 2005

[24] DJ. Larkman and R. G. Nunes, “Parallel magnetic resonance imaging,” Physics in Medicine and Biology, vol. 52, pp. R15–R55, 2007.

[25] F.H. Lin, T.Y. Huang, N.K. Chen, F.N. Wang, S. M. Stufflebeam, J. W. Belliveau, et al., “Functional MRI Using Regularized Parallel Imaging Acquisition,” Magnetic resonance in medicine : official journal of the Society of Magnetic Resonance in Medicine / Society of Magnetic Resonance in Medicine, vol. 54, pp. 343–353, 2005.

[26] S. Geethanath, R. Reddy, A. S. Konar, S. Imam, R. Sundaresan, et al., “Compressed Sensing MRI: A Review,” Critical Reviews in Biomedical Engineering, vol. 41, pp. 183-204, 2013.

[27] S. P. Mallat, “A wavelet tour of signal processing,” Access online via Elsevier, 1999.

[28] G. Kutyniok and D. Labate, *Shearlets: Multiscale Analysis for Multivariate Data*. Birkh¨auser, Boston, 2012.

[29] Y.C. Eldar, G. Kutyniok, *Compressed Sensing: theory and applications*. Cambridge University Press, 2012.

[30] D. Donoho and J. Tanner, “Precise undersampling theorems,” *Proc. IEEE*, vol. 98, pp. 913–924, 2010.

[31] D. L. Donoho and M. Elad, “Optimally sparse representation in general (nonorthogonal) dictionaries via ℓ1 minimization,” Proceedings of the National Academy of Sciences, vol. 100, pp. 2197-2202, 2003.

[32] A. Cohen, W. Dahmen, and R. Devore, “Compressed sensing and best *k*-term approximation,” J.Amer. Math. Soc., vol. 22, pp. 211-231, 2009.

[33] E. Candès and T. Tao, “Decoding by linear programming,” *IEEE Trans. Inform. Theory*, vol 52, pp. 489-509, 2006.

[34] M.Davenport, “Random observations on random observations: Sparse signal acquisition and processing,” PhD dissertation, Rice University, 2010.

[35] D. L. Donoho, M. Elad, and V. Temlyahov, “Stable recovery of sparse overcomplete representations in the presence of noise,” *IEEE Trans. Inform. Theory*, vol. 52, pp. 6-18, 2006.

[36] J. Tropp and A. Gilbert, “Signal recovery form partial information via orthogonal matching pursuit,” *IEEE Trans. Inform. Theory*, vol. 53, pp. 4655-4666, 2007.

[37] M. Rosenfeld, “The Mathematics of Paul Erdo˝s II,” in *Praise of the Gram matrix*, pp. 318–323. Springer, Berlin, Germany, 1996.

[38] T. Strohmer and R. Heath, “Grassmanian frames with applications to coding and communication,” *Appl. Comput. Harmon. Anal.*, vol. 14, pp. 257–275, 2003.

[39] A. Cohen, W. Dahmen, and R. DeVore, “Instance optimal decoding by thresholding in compressed sensing,” *Int. Conf. Harmonic Analysis and Partial Differential Equations*, Madrid, Spain, Jun. 2008.

[40] J. Haupt and R. Nowak, “Signal reconstruction from noisy random projections,” *IEEE Trans. Inform. Theory*, vol. 52, pp. 4036–4048, 2006.

[41] S. Muthukrishnan, *Data Streams: Algorithms and Applications*. Now Publishers, Boston, MA, 2005.

[42] S. S. Chen, D. L. Donoho, and M. A. Saunders, “Atomic decomposition by basis pursuit,” *SIAM J. Sci. Comput.*, vol. 20, pp. 33–61, 1998.

[43] A. Beck and M. Teboulle, “A fast iterative shrinkage-thresholding algorithm for linear inverse problems,” *SIAM J. Imag. Sci.*, vol. 2, pp. 183–202, 2009.

[44] M. Figueiredo, R. Nowak, and S. Wright, “Gradient projections for sparse reconstruction: Application to compressed sensing and other inverse problems,” *IEEE J. Select. Top. Signal Processing*, vol. 1, pp. 586–597, 2007

[45] J. Friedman, T. Hastie, and R. Tibshirani, “Regularization paths for generalized linear models via coordinate descent,” *J. Stats. Software*, vol. 33, pp. 1–22, 2010.

[46] E. Hale, W. Yin, and Y. Zhang, “A fixed-point continuation method for $l_1$-regularized minimization with applications to compressed sensing,” *Technical Report TR07-07*, Rice Univ., CAAM Dept., 2007.

[47] I. Loris, “On the performance of algorithms for the minimization of $l_1$-penalized functions,” *Inverse Problems*, vol. 25(3):035008, 2009.

[48] S. Osher, Y. Mao, B. Dong, and W. Yin, “Fast linearized Bregman iterations for compressive sensing and sparse denoising,” *Comm. in Math. Sciences*, vol. 8, pp. 93–111, 2010.

[49] Z. Wen, W. Yin, D. Goldfarb, and Y. Zhang, “A fast algorithm for sparse reconstruction based on shrinkage, subspace optimization and continuation,” *SIAM J. on Sci. Comp.*, vol 32, pp. 1832–1857, 2010.

[50] S. Wright, R. Nowak, and M. Figueiredo, “Sparse reconstruction by separable approximation,” *IEEE Trans. Signal Processing*, vol. 57, pp. 2479–2493, 2009.

[51] A. Yang, S. Sastray, A. Ganesh, and Y. Ma, “Fast $l_1$-minimization algorithms and an application in robust face recognition: A review,” in *Proc. IEEE Int. Conf. Image Processing (ICIP)*, Hong Kong, Sept. 2010.

[52] W. Dai and O. Milenkovic, “Subspace pursuit for compressive sensing signal reconstruction,” *IEEE Trans. Inform. Theory*, vol. 55, pp. 2230–2249, 2009

[53] S.P.Boyd and L. Vandeberghe, *Convex optimization*.Cambridge University Press, 2004.

[54] K. Sung and B. A. Hargreaves, “High-frequency subband compressed sensing MRI using quadruplet sampling,” presented at Magnetic Resonance in Medicine, 2012 [Online]. Available: http://onlinelibrary.wiley.com/doi/10.1002/mrm.24592/abstract;jsessionid=403CC7AB962031BE9C94F0D97A960083.f02t01

[55] W. Yin, S. Osher, D. Goldfarb, and J. Darbon, “Bregman iterative algorithms for $l_1$-minimization with applications to compressed sensing,” *SIAM J. Imag. Sci.*, vol. 1, pp. 143–168, 2008.

[56] B. Efron, T. Hastie, I. Johnstone, and R. Tibshirani, “Least angle regression,” *Annals, of Statistics*, vol. 32, no. 2, pp. 407-451, 2004.

[57] M.A.T. Figueiredo, R.D. Nowak, and S.J. Wright, “Gradient projection for sparse reconstruction: Application to compressed sensing and other inverse problems,” *IEEE J. Sel. Top. Signa.*, vol. 1, pp. 586–597, 2007.

[58] I. Daubechies, M. Defrise, and C. De Mol, “An iterative thresholding algorithm for linear inverse problems with a sparsity constraint,” *Comm. Pure Appl. Math.*, vol. 57, pp. 1413-1457, 2004.

[59] E. Candes and B. Recht, “Exact matrix completion via convex optimization,” *Foundations of Computational Mathematics*, vol. 9, no. 6, pp. 717-772, 2009.

[60] R. Berinde, P. Indyk, and M. Ruzic, “Practical near-optimal sparse recovery in the $l_1$ norm,” *in Proc. Allerton Conf. Communication, Control, and Computing*, Monticello, IL, Sept. 2008.

[61] T. Blumensath and M. Davies, “Gradient pursuits,” *IEEE Trans. Signal Processing*, vol. 56, pp. 2370–2382, 2008.

[62] E. Candès and T. Tao, “Near optimal signal recovery from random projections: Universal encoding strategies,” *IEEE Transactions on Information Theory*, vol. 52, no. 12, pp.5406–5425, 2006.

[63] Y. Tsaig, DL. Donoho, “Extensions of compressed sensing,” *Signal Process*, vol. 86, pp. 533-548, 2006.

[64] M. Davenport and M. Wakin, “Analysis of orthogonal matching pursuit using the restricted isometry property,” *IEEE Trans. Inform. Theory*, vol. 56, pp. 4395–4401, 2010.

[65] D. Donoho, I. Drori, Y. Tsaig, and J.-L. Stark, “Sparse solution of underdetermined linear equations by stagewise orthogonal matching pursuit,” Preprint, 2006.

[66] P. Indyk and M. Ruzic, “Near-optimal sparse recovery in the $l_1$ norm,” in *Proc. IEEE Symp. Found. Comp. Science (FOCS)*, Philadelphia, PA, Oct. 2008.

[67] J. Tropp and A. Gilbert, “Signal recovery from random measurements via orthogonal matching pursuit,” *IEEE Transactions on Information Theory*, vol. 53, no. 12, pp. 4655, 2007.

[68] D. Needell and J. Tropp, “CoSaMP: Iterative signal recovery from incomplete and inaccurate samples,” *Appl. Comput. Harmon. Anal.*, vol. 26, pp. 301–321, 2009.

[69] D. Needell and R. Vershynin, “Uniform uncertainty principle and signal recovery via regularized orthogonal matching pursuit. Found,” *Comput. Math.*, vol. 9, pp. 317–334, 2009.

[70] D. Needell and R. Vershynin, “Signal recovery from incomplete and inaccurate measurements via regularized orthogonal matching pursuit,” *IEEE J. Select. Top. Signal Processing*, vol. 4, pp. 310–316, 2010.

[71] S. Mallat and Z. Zhang, “Matching pursuits with time-frequency dictionaries,” *IEEE Trans. Signal Processing*, vol. 41, pp. 3397–3415, 1993.

[72] T. Blumensath and M. Davies, “Iterative hard thresholding for compressive sensing,” *Appl. Comput. Harmon. Anal.*, vol. 27, pp. 265–274, 2009.

[73] G. Cormode and S. Muthukrishnan, “Improved data stream summaries: The count-min sketch and its applications,” *J. Algorithms*, vol. 55, no. 1, pp. 58–75, 2005.

[74] A. Gilbert, M. Strauss, J. Tropp, and R. Vershynin, “One sketch for all: fast algorithms for compressed sensing,” in *Proceedings of the thirty-ninth annual ACM Symposium on Theory of Computing*, pp. 237-246, ACM, 2007.

[75] A. Gilbert, Y. Li, E. Porat, and M. Strauss, “Approximate sparse recovery: Optimizing time and measurements,” in *Proc. ACM Symp. Theory of Comput.*, Cambridge, MA, Jun. 2010.

[76] A. Gilbert, M. Strauss, J. Tropp, and R. Vershynin, “Algorithmic linear dimension reduction in the l1 norm for sparse vectors,” Arxiv preprint cs/0608079, 2006.

[77] A. Gilbert, S. Muthukrishnan, and M. Strauss, “Improved time bounds for near-optimal sparse Fourier representations,” in *Proceedings of SPIE*, vol. 5914, pp. 59141A, Citeseer, 2005

[78] DS. Taubman and M. W. Marcellin, “JPEG 2000: Image compression fundamentals, standards, and practice,” *Kluwer International Series in Engineering and Computer Science*, 2002.

[79] Y. Yu, M. Hong, H. Wang, F. Liu, and S. Crozier, “Compressed sensing MRI using Singular Value Decomposition based sparsity basis, ” *Engineering in Medicine and Biology Society*, EMBC, 2011 Annual International Conference of the IEEE. IEEE, 2011

[80] Y. Yu, J. Jin, F. Liu and S. Corzier, “Multidimensional compressed sensing MRI using tensor decomposition-based sparsifying transform,” *PloS ONE*, vol. 9, no. 6, e98441, 2014.

[81] R. L. Cook , “Stochastic sampling in computer graphics,” ACM Transactions on Graphics, vol. 5, no. 1, pp. 51-72, 1986.

[82] A. Averbuch, R. R. Coifman, D. L. Donoho, M. Elad, and M. Israeli, “Fast and accurate Polar Fourier transform,” *Applied and Computational Harmonic Analysis*, vol. 21, pp. 145-167, 2006.

[83] J. Huang, S. Zhang, and D. Metaxas, “Efficient MR image reconstruction for compressed MR imaging,” *Medical Image Analysis*, vol. 15, pp. 670-679, 2011.

[84] H. Jung, K. Sung, KS. Nayak, EY. Kim, and JC. Ye, “k–t FOCUSS:a general compressed sensing framework for high resolution dynamic MRI,” *Magnetic Resonance Medicine*, vol. 61, no.1, pp. 103–16, 2009.

[85] J. Ji, T. Lang, “Dynamic MRI with compressed sensing imaging using temporal correlations,” 2008 5th *IEEE International Symposium on Biomedical Imaging: From Nano to Macro*, pp. 1613–1616,2008.

[86] H. Chandarana, L. Feng, TK. Block, et al, “Free-Breathing Contrast-Enhanced Multiphase MRI of the Liver Using a Combination of Compressed Sensing, Parallel Imaging, and Golden-Angle Radial Sampling,” *Investigative radiology*, vol. 48, no. 1, pp. 10, 2013.

[87] R. Otazo, D. Kim, L. Axel, and D.K. Sodickson, “Combination of Compressed Sensing and Parallel Imaging for Highly Accelerated First-Pass Cardiac Perfusion MRI,” *Magnetic Resonance in Medicine*, vol. 64, no. 3, pp. 767-776, 2010.

[88] MH. Vandsburger, FH. Epstein, “Emerging MRI methods intranslational cardiovascular research,” *J Cardiovasc Translat Res*, vol. 4, no. 4, pp.477–492, 2011.

[89] C. Bilen, IW. Selesnick, Y. Wang, R. Otazo, D. Kim, L. Axel, and D.K. Sodickson, “On compressed sensing in parallel MRI of cardiac perfusion using temporal wavelet and TV regularization,” *Acoustics Speech and Signal Processing (ICASSP)*, Piscataway, NJ, IEEE, pp. 630–633, 2010.

[90] G. Vincenti, P. Monney, J. Chaptinel, T. Rutz, S. Coppo, M. O. Zenge, et al., "Compressed Sensing Single–Breath-Hold CMR for Fast Quantification of LV Function, Volumes, and Mass," *JACC: Cardiovascular Imaging*, vol. 7, pp. 882-892, 2014.

[91] Akçakaya, Mehmet et al, "Accelerated Non-Contrast Enhanced Pulmonary Vein MRA with Distributed Compressed Sensing," *Journal of Magnetic Resonance Imaging* , vol. 33, no. 5, pp. 1248–1255, 2011.

[92] C. Chen and J. Huang, "Compressive Sensing MRI with Wavelet Tree Sparsity," *Advances in Neural Information Processing Systems*, vol. 25, pp. 1124-1132, 2012.

[93] M. I. Menzel, Ek T. Tan, K. Khare, J. I. Sperl, K. F. King X. Tao, C. J. Hardy and L. Marinelli, "Accelerated diffusion spectrum imaging in the human brain using compressed sensing," *Magnetic Resonance in Medicine*, vol. 66, no. 5, pp. 1226-1233, 2011.

[94] H. Jung and J. C. Ye, "Performance evaluation of accelerated functional MRI acquisition using compressed sensing," *2009 IEEE International Symposium on Biomedical Imaging: From Nano to Macro*, Boston, MA, 2009, pp. 702-705.

[95] P. K. Han, S-H Park, S-G. Kim , and J. C. Ye, "Compressed Sensing for fMRI: Feasibility Study on the Acceleration of Non-EPI fMRI at 9.4T," *BioMed Research International*, 2015.

[96] X. Zong, J. Le, A. Poplawsky, S-G. Kim and J. C. Ye, "Compressed Sensing fMRI using Gradient-recalled Echo and EPI Sequences," *NeuroImage*, vol. 92, pp. 312-321. 2014.

[97] H. Wang, D. Liang and L. Ying, "Pseudo 2D random sampling for compressed sensing MRI," in *Engineering in Medicine and Biology Society, 2009. EMBC 2009. Annual International Conference of the IEEE*, 2009, pp. 2672-2675.

[98] E. Cande`s and D. Donoho, 'Curvelets – a surprisingly effectivenonadaptive representation for objects with edges', in Cohen, A.,Rabut, C., Schumaker, L. (Eds.) *Curves and surfaces* (Vanderbilt University Press, Nashville, TN, USA, 2000), pp. 105– 120.

[99] M. Hong, Y. Yu, H. Wang, F. Liu and S. Crozier, "Compressed sensing MRI with Singular Value Decomposition based sparsity basis," *Physics in Medicine and Biology*, vol. 56, no. 19, pp. 6311-6325, 2011.

[100] D. S. Taubman and M. W. Marcellin, “JPEG 2000: Image Compression Fundamentals, Standards and Practice,” *International Series in Engineering and Computer Science*, Norwell, MA: Kluwer, 2002.

[101] M. Akçakaya, S. Nam, T. A. Basha, K. Kawaji, V. Tarokh, and R. Nezafat, “An Augmented Lagrangian Based Compressed Sensing Reconstruction for Non-Cartesian Magnetic Resonance Imaging without Gridding and Regridding at Every Iteration,” *PLoS ONE*, vol. 9, p. e107107, 2014.

[102] K. T. Block, M. Uecker, and J. Frahm, “Undersampled radial MRI with multiple coils. Iterative image reconstruction using a total variation constraint,” *Magnetic Resonance in Medicine*, vol. 57, pp. 1086-1098, 2007.

[103] A. Haase, “Snapshot flash MRI. applications to t1, t2, and chemical-shift imaging,” *Magnetic Resonance in Medicine*, vol. 13, pp. 77-89, 1990.

[104] M. Stehling, R. Turner, and P. Mansfield, “Echo-planar imaging: magnetic resonance imaging in a fraction of a second,” *Science*, vol. 254, pp. 43-50, 1991.

[105] K. Sung and B. A. Hargreaves, “High-frequency subband compressed sensing MRI using quadruplet sampling,” *Magnetic Resonance in Medicine*, 2012 [Online]. Available: http://onlinelibrary.wiley.com/doi/10.1002/mrm.24592/abstract;jsessionid=403CC7AB962031BE9C94F0D97A960083.f02t01

[106] P. M. Margosian, G. DeMeester and H. Liu, “Partial Fourier Acquisition in MRI,” in *Encyclopaedia of Magnetic Resonance*. John Wiley & Sons Ltd, 2007.

[107] N. Chauffert, P. Ciuciu, J. Kahn and P. Weiss, “Variable density sampling with continuous sampling trajectories,” Cornell University, 2013.

[108] R.W. Chan, E.A. Ramsay, E.Y. Cheung and D.B. Plewes, “The influence of radial undersampling schemes on compressed sensing reconstruction in breast MRI,” *Magnetic Resonance in Medicine*, vol.67, pp 363-377 2012.

[109] Z. Feng, F. Liu, M. Jiang, S. Crozier, H. Guo and Y. Wang, “Improved l1-SPIRiT using 3D Walsh transform-based sparsity basis,” *Magnetic Resonance..Imaging*, vol. 32, no. 7, pp. 924–933, 2014.

[110] Y. Ma, D. Baron and D. Needell, “Two-Part Reconstruction in Compressed Sensing,” 2013 in *IEEE Global Conference on Signal and Information Processing*, 2013.

[111] R. G. Baraniuk, R. A. DeVore, G. Kyriazis and X. M. Yu, “Near best tree approximation,” *Advances in Computational Mathematics*, vol.16, pp.357–373, 2012.

[112] H. Oh and S. Lee, “Visually weighted reconstruction of compressive sensing MRI,” *Magnetic Resonance Imaging*, vol. 32, pp. 270-280, 2014..

[113] R. Chartrand, “Fast algorithms for nonconvex compressive sensing: MRI reconstruction from very few data,” *Biomedical Imaging: From Nano to Macro, 2009. ISBI '09. IEEE International Symposium on*, pp.262-265, June 28 2009-July 1 2009.

[114] F. A. Razzaq, S. Mohamed, A. Bhatti, and S. Nahavandi, “Non-uniform sparsity in rapid compressive sensing MRI,” *Systems, Man, and Cybernetics (SMC), 2012 IEEE International Conference on*, pp.2253-2258, 2012.

[115] S. G. Lingala, H. Yue, E. DiBella, and M. Jacob, “Accelerated dynamic MRI exploiting sparsity and low-rank structure: k-t SLR,” *IEEE Trans. Med. Imag.*, vol. 30, no. 5, pp. 1042–1054, May 2011.

[116] M. Seeger, H. Nickisch, R. Pohmann, and B. Schölkopf, “Optimization of k-space trajectories for compressed sensing by Bayesian experimental design,” *Magnetic Resonance in Medicine*, vol. 63, pp. 116-126, 2010.

[117] Y. Zhang, B. S. Peterson, G. Ji, and Z. Dong, “Energy Preserved Sampling for Compressed Sensing MRI,” *Computational and Mathematical Methods in Medicine*, vol. 2014, p. 12, 2014.

[118] L. Weizman, Y.C. Eldar and D. Ben Bashat. “The application of compressed sensing for longitudinal MRI,” arXiv preprint arXiv:1407.2602, 2014.

[119] L. Feng, R. Grimm, K. T. Block, H. Chandarana, S. Kim, J. Xu, et al., “Golden-angle radial sparse parallel MRI: Combination of compressed sensing, parallel imaging, and golden-angle radial sampling for fast and flexible dynamic volumetric MRI,” *Magnetic Resonance in Medicine*, vol. 72, pp. 707-717, 2014.

[120] L. Ciancarella, D. Avola, and G. Placidi, "Adaptive Sampling and Reconstruction for Sparse Magnetic Resonance Imaging," in *Computational Modeling of Objects Presented in Images*, vol. 15, pp. 115-130, 2014;

[121] C. M. Tsai and D. G. Nishimura. "Reduced aliasing artifacts using variable-density k-space sampling trajectories," *Magnetic Resonance in Medicine*, vol. 43, pp. 452-458, 2000.

[122] Y. Yang, F. Liu, W. Xu, and S. Crozier, "Compressed Sensing MRI via Two-stage Reconstruction," *Biomedical Engineering, IEEE Transactions on*, vol. 62, pp. 110-118, 2015.

[123] Z. Wang, A. C. Bovik, H. R. Sheikh and E. P. Simoncelli, "Image quality assessment: From error visibility to structural similarity," *IEEE Transactions on Image Processing*, vol. 13, no. 4, pp. 600-612, Apr. 2004

[124] M. Murphy, M. Alley, J. Demmel, K. Keutzer, S. Vasanawala, and M. Lustig, "Fast l1-SPIRiT Compressed Sensing Parallel Imaging MRI: Scalable Parallel Implementation and Clinically Feasible Runtime," *Medical Imaging, IEEE Transactions on*, vol. 31, pp. 1250-1262, 2012.

[125] J. Chi, F. Liu, E. Weber, Y. Li and S. Crozier, "GPU-Accelerated FDTD Modeling of Radio-Frequency Field Tissue Interactions in High-Field MRI", *IEEE Transactions on Biomedical Engineering*, vol. 58, no. 6, pp. 1789-1796, June 2011.

[126] G. H. Glover and J. M. Pauly, "Projection Reconstruction Techniques for Reduction of Motion Effects in MRI," *Magnetic Resonance in Medicine*, vol. 28, pp. 275–289, 1992.

[127] MA. Bernstein, KF. King and XJ. Zhou, Handbook of MRI pulse sequences, 2004.

[128] T.P. Trouard, Y. Sabharwal, M.I. Altbach and A.F. Gmitro, "Analysis and comparison of motion-correction techniques in diffusion-weighted imaging," *J Magn Reson Imaging*. vol. 6, pp. 925–935, 1996.

[129] M. Katoh, E. Spuentrup, A. Buecker, W.J. Manning, R.W. Gunther, et al, "MR coronary vessel wall imaging: comparison between radial and spiral k-space sampling," *J Magn Reson Imaging*, vol. 23, pp. 757–762, 2006.

[130] D.R. Thedens, P. Irarrazaval, T.S. Sachs, C.H. Meyer and D.G. Nishimura, "Fast magnetic resonance coronary angiography with a three-dimensional stack of spirals trajectory," *Magnetic Resonance in Medicine*, vol. 41, pp. 1170–1179, 1999.

[131] D.C. Peters, F.R. Korosec, T.M. Grist, W.F. Block, J.E. Holden, et al, "Undersampled projection reconstruction applied to MR angiography," *Magnetic Resonance in Medicine*, vol. 43, pp. 91–101, 2000.

[132] K. T. Block, "Advanced methods for radial data sampling in magnetic resonance imaging." SUB University of Goettingen, 2008.

[133] J. C. Ye, S. Tak, Y. Han, and H. W. Park, "Projection reconstruction MR imaging using FOCUSS," *Magnetic Resonance in Medicine*, vol. 57, pp. 764-775, 2007.

[134] H. Jung, J. Park, J. Yoo, and J. C. Ye, "Radial k-t FOCUSS for high-resolution cardiac cine MRI," *Magnetic Resonance in Medicine*, vol. 63, pp. 68-78, 2010.

[135] Q.H. Liu and N. Nguyen, "Nonuniform fast Fourier transform (NUFFT) algorithm and its applications," in *Antennas and Propagation Society International Symposium, IEEE*, vol.3, pp. 1782-1785, 1998.

[136] S. Jiayu, Q.H. Liu, S. L. Gewalt, G. Cofer, G. A. Johnson, and L. Qing Huo, "Least-Square NUFFT Methods Applied to 2-D and 3-D Radially Encoded MR Image Reconstruction," *Biomedical Engineering, IEEE Transactions on*, vol. 56, pp. 1134-1142, 2009.

[137] L. Feng, L. Axel, H. Chandarana, K. T. Block, D. K. Sodickson, and R. Otazo, "XD-GRASP: Golden-angle radial MRI with reconstruction of extra motion-state dimensions using compressed sensing," *Magnetic Resonance in Medicine*, 2015.

[138] J.D. O'Sullivan, "A Fast Sinc Function Gridding Algorithm for Fourier Inversion in Computer Tomography," *Medical Imaging, IEEE Transactions on*, vol.4, no.4, pp.200,207, Dec. 1985

[139] A. Averbuch, R. Coifman, D.L. Donoho, M. Israeli, "Fast Slant Stack: A notion of Radon transform for data in a Cartesian grid which is rapidly computible, algebraically exact, geometrically faithful and invertible", Technical Report, Statistics Department, Stanford University, 2003.

[140] F. Huang, H. Cheng, and G. Duensing, "Method of pseudopolar acquisition and reconstruction for dynamic MRI," U.S. Patent 2005/0253580 A1, Nov.17, 2005.

[141] J. Jackson, C.H. Meyer, D.G. Nishimura, and A. Macovski, "Selection of a convolution function for Fourier inversion using gridding," *IEEE Transactions on Medical Imaging*, vol. 10, no. 3, pp. 473–478, 1991.

[142] J. Fessler, and B. P. Sutton, "Nonuniform fast Fourier transforms using min-max interpolation." *Signal Processing, IEEE Transactions on*, vol. 51(2), pp. 560-574, 2003.

[143] Y. Yang, F. Liu, Z. Jin, S. Crozier, "Aliasing Artefact Suppression in Compressed Sensing MRI for Random Phase-encode Undersampling," *Biomedical Engineering, IEEE Transactions on* , vol.62, pp. 2215-2223, 2015.

[144] C. J. Bergin, J. M. Pauly, and A. Macovski, "Lung parenchyma: projection reconstruction MR imaging," *Radiology*, vol. 179, pp. 777, 1991.

[145] R. Dosselmann and X. Yang, "A comprehensive assessment of the structural similarity index," *Signal, Image and Video Processing*, vol. 5, no. 1,pp. 81–91, 2009

[146] G. Plonka and J. Ma, "Curvelet-Wavelet Regularized Split Bregman Iteration for Compressed Sensing," International Journal of Wavelets, Multiresolution and Information Processing, vol 9, no. 1, pp. 79-110, 2011.

[147] J. Ma, "Improved Iterative Curvelet Thresholding for Compressed Sensing and Measurement," in *IEEE Transactions on Instrumentation and Measurement*, vol. 60, no. 1, pp. 126-136, 2011.

[148] A. Secker and D. Taubman, "Motion-compensated highly scalable video compression using an adaptive 3D wavelet transform based on lifting," Image Processing, 2001. Proceedings. 2001 International Conference on, Thessaloniki, Greece, 2001, vol. 2, pp. 1029-1032.

[149] D. Labate and P. Negi, "3D Discrete Shearlet Transform and video denoising," IEEE Transactions on Image Processing, vol. 21, no. 6, pp. 2944-2954, 2012.

[150] R. Chartrand and W. Yin, "Iteratively reweighted algorithms for compressive sensing", IEEE International Conference on Acoustics, Speech and Signal Processing. IEEE, 2008.

[151] A. Beck and M. Teboulle, “A fast iterative shrinkage-thresholding algorithm for linear inverse problems,” *SIAM J. Imag. Sci.*, vol. 2, no. 1, pp. 183–202, 2009.

[152] W. Hao, J. Li, X. Qu, and Z. Dong, “Fast iterative contourlet thresholding for compressed sensing MRI,” *Electron. Lett.*, vol. 49, no. 19, pp. 1206–1208, Sep. 2013.

[153] J. Huang, S. Zhang, D. Metaxas, “Efficient MR image reconstruction for compressed MR imaging,” *Medical Image Analysis*, vol. 15, no. 5, pp. 670-679, 2011.

[154] R. Otazo, D. Kim, L. Axel and D.K. Sodickson, “Combination of Compressed Sensing and Parallel Imaging for Highly Accelerated First-Pass Cardiac Perfusion MRI,” *Magnetic Resonance in Medicine : Official Journal of the Society of Magnetic Resonance in Medicine / Society of Magnetic Resonance in Medicine*, vol. 64, no. 3, pp. 767–776, 2010.

[155] A. Ersoz and T. Muftuler, “Pseudo-Polar trajectories achieve high acceleration rates with high image fidelity: experiments at 3T and 7T”, *International Society for Magnetic Resonance in Medicine, 23rd annual meeting and exhibition*, Toronto, Canada, May 2015.